

<https://doi.org/10.15388/vu.thesis.621>

<https://orcid.org/0000-0001-6566-5634>

VILNIUS UNIVERSITY

CENTER FOR PHYSICAL SCIENCES AND TECHNOLOGY

Yauheni Talochka

# Transient Processes in Inorganic Multicomponent Crystalline Scintillators and Semiconductors

**DOCTORAL THESIS**

Natural Sciences,  
Physics (N 002)

VILNIUS 2024

The thesis was prepared within the period from 2020 to 2024 at the Institute of Photonics and Nanotechnology, Vilnius University. The research was partially supported by the Research Council of Lithuania.

**Academic supervisor – Prof. Habil. Dr. Gintautas Tamulaitis** (Vilnius University, Natural Sciences, Physics, N 002)

**The Dissertation Defense Panel:**

**Chairman** – Prof. Dr. Darius Abramavičius (Vilnius University, Natural Sciences, Physics N 002).

**Members:**

Prof. Dr. Sergei Baranovskii (University of Cologne and Philipps-University Marburg, Germany, Natural Sciences, Physics N 002),

Prof. Habil. Dr. Vidmantas Gulbinas (Center for Physical Sciences and Technology, Natural Sciences, Physics N 002),

Dr. Vytautas Karpus (Center for Physical Sciences and Technology, Natural Sciences, Physics N 002),

Dr. Karolis Kazlauskas (Vilnius University, Natural Sciences, Physics N 002).

The thesis will be defended at a public meeting of the Dissertation Defense Panel on 20th September 2024, in room A101 at the National Center of Physical and Technological Sciences.

Address: Saulėtekio al. 3. Vilnius, Lithuania

Tel. (85) 264 9211; e-mail: [office@ftmc.lt](mailto:office@ftmc.lt)

The text of this thesis can be accessed at the libraries of the Center for Physical Sciences and Technology and the Vilnius University as well as on the website of Vilnius University:

[www.vu.lt/lt/naujienos/ivykiu-kalendorius](http://www.vu.lt/lt/naujienos/ivykiu-kalendorius)

<https://doi.org/10.15388/vu.thesis.621>

<https://orcid.org/0000-0001-6566-5634>

VILNIAUS UNIVERSITETAS  
FIZINIŲ IR TECHNOLOGIJOS MOKSLŲ CENTRAS

Yauheni Talochka

# Kinetiniai procesai neorganiniuose daugiakomponenčiuose kristaliniuose scintiliatoriuose ir puslaidininkiuose

**DAKTARO DISERTACIJA**

Gamtos mokslai,  
Fizika (N 002)

VILNIUS 2024

Disertacija rengta 2020–2024 metais Vilniaus universiteto Fotonikos ir Nanotechnologijų institute.

Tyrimus dalinai parėmė Lietuvos mokslo taryba.

**Mokslinis vadovas – prof. habil. dr. Gintautas Tamulaitis** (Vilniaus universitetas, gamtos mokslai, fizika, N 002)

Gynimo taryba:

**Pirmininkas** – prof. dr. Darius Abramavičius (Vilniaus universitetas, gamtos mokslai, fizika, N 002).

**Nariai:**

prof. dr. Sergei Baranovskii (Kelno universitetas ir Marburgo Pilypo universitetas, Vokietija, gamtos mokslai, fizika, N 002),

prof. habil. dr. Vidmantas Gulbinas (Fizinių ir technologijos mokslų centras, gamtos mokslai, fizika, N 002),

dr. Vytautas Karpus (Fizinių ir technologijos mokslų centras, gamtos mokslai, fizika, N 002),

dr. Karolis Kazlauskas (Vilniaus universitetas, gamtos mokslai, fizika, N 002).

Disertacija ginama viešame Gynimo tarybos posėdyje 2024 m. rugsėjo mėn. 20 d. Nacionalinio fizinių ir technologijos mokslų centro posėdžių salėje A101.

Adresas: Saulėtekio al. 3, Vilnius, Lietuva  
tel. (85) 264 9211; el. paštas [office@ftmc.lt](mailto:office@ftmc.lt)

Disertaciją galima peržiūrėti Fizinių ir technologijos mokslų centro ir Vilniaus universiteto bibliotekose bei Vilniaus universiteto interneto svetainėje adresu: <https://www.vu.lt/naujienos/ivykiu-kalendorius>

## ACKNOWLEDGEMENT

I sincerely thank my supervisor Prof. Gintautas Tamulaitis for helping me with my studies and more during all these years. In addition, I thank Prof. Andrey Vasil'ev and Prof. Mikhail Korjik for sharing their pioneering experience in this field and for guiding discussions indispensable for this work. Also, I thank Dr. Saulius Nargelas and Dr. Žydrūnas Podlipskas for sharing experimental data.

## CONTENTS

ABBREVIATIONS.....	9
INTRODUCTION .....	11
MAIN GOAL AND TASKS.....	13
NOVELTY.....	15
DEFENSIVE STATEMENTS .....	17
AUTHOR'S CONTRIBUTION.....	17
LIST OF PUBLICATIONS .....	18
OTHER RELEVANT PUBLICATIONS.....	18
LIST OF CONFERENCE PRESENTATIONS .....	19
1. LITERATURE REVIEW .....	20
1.1. Fast scintillators and their applications in physical measurements.. .....	20
1.2. Role of timing parameters of a scintillation material in the formation of intrinsic time resolution .....	22
1.3. Ternary nitride semiconductors and their applications in electronic and optoelectronic devices .....	23
1.4. Transient processes in inorganic crystalline materials.....	24
1.4.1. Scintillators.....	24
1.4.2. Semiconductors .....	28
2. EFFECT OF COMPOSITIONAL DISORDER ON NON- EQUILIBRIUM FREE CARRIER TRANSPORT IN MIXED SCINTILLATORS.....	30
2.1. Thermodynamic model of ion distribution in mixed crystalline scintillators.....	30
2.2. Simulation of the cation distribution in LYSO scintillator .....	32
2.3. Pseudopotential-based model of fluctuating crystal potential ..	34
2.4. Simulation of the pseudopotential for the conduction band in LYSO scintillator .....	38
2.5. Electron(hole)-phonon scattering in the virtual crystal approximation .....	40
2.6. Elastic scattering of non-equilibrium carriers on pseudopotential fluctuations in the Born approximation .....	43
2.7. Elastic scattering of non-equilibrium carriers on pseudopotential fluctuations in the coherent potential approximation.....	45
2.8. Calculation of the alloy scattering rate for electrons in LYSO scintillator .....	47
2.9. Density of states in a crystalline compound .....	50
2.10. Calculation of the density of states in LYSO scintillator .....	50

2.11. Conclusions.....	52
3. EFFECT OF COMPOSITIONAL DISORDER ON CARRIER DIFFUSION IN COMPOUND SEMICONDUCTORS .....	53
3.1. Materials and experimental techniques.....	53
3.2. Electron(hole)-phonon scattering in crystalline compound with strong compositional disorder.....	54
3.3. Simulation of pseudopotential for the valence band in AlGaN semiconductor.....	56
3.4. Calculation of the heavy hole-phonon scattering rates in AlGaN semiconductor.....	58
3.5. Calculation of the alloy scattering rate for free heavy holes in AlGaN semiconductor .....	61
3.6. Simulation of the heavy hole diffusion in AlGaN semiconductor.....	62
3.7. Conclusions.....	64
4. EFFECT OF COMPOSITIONAL DISORDER ON EXCITATION TRANSFER IN GADOLINIUM-CONTAINING GARNET HOST	66
4.1. Experimental technique and results .....	66
4.2. A kinetic Monte-Carlo model of excitation transfer through gadolinium subsystem in quaternary garnet host via the dipole- dipole and Dexter mechanisms .....	69
4.3. Results and discussion .....	72
4.4. Conclusions.....	75
5. EFFECT OF COMPOSITIONAL DISORDER ON SPECTRAL PROPERTIES OF CERIUM IONS IN QUATERNARY GARNET SCINTILLATORS.....	77
5.1. Materials and experimental technique .....	77
5.2. Results and discussion .....	78
5.3. Conclusions.....	86
GENERAL CONCLUSIONS .....	87
SANTRAUKA .....	89
ĮVADAS.....	89
PAGRINDINIS TIKSLAS IR UŽDAVINIAI .....	91
NAUJUMAS .....	93
GINAMIEJI TEIGINIAI.....	95
AUTORIAUS INDĖLIS .....	95
6. SUDĖTIES NETVARKOS POVEIKIS NEPUSIAUSVIRUJŲ KRŪVININKŲ PERNAŠAI MIŠRIUOSE SCINTILIATORIUOSE.....	96

6.1.	Rezultatai ir jų aptarimas .....	96
6.2.	Išvados .....	99
7.	SUDĖTIES NETVARKOS POVEIKIS NEŠĖJŲ DIFUZIJAI SUDĖTINIUOSE PUSLAIDININKIUOSE.....	101
7.1.	Medžiagos ir eksperimentinės metodikos .....	101
7.2.	Rezultatai ir aptarimas .....	101
7.3.	Išvados .....	102
8.	SUDĖTIES NETVARKOS POVEIKIS SUŽADINIMO PERNAŠAI GADOLINIO TURINČIAME GRANATO TIPO KRISTALE .....	104
8.1.	Eksperimento metodika ir rezultatai .....	104
8.2.	Rezultatai ir aptarimas .....	104
8.3.	Išvados .....	105
9.	SUDĖTIES NETVARKOS POVEIKIS SPEKTRINĖMS CERIO JONŲ SAVYBĖMS KETURNARIUOSE GRANATO TIPO SCINTILIATORIUOSE .....	106
9.1.	Medžiagos ir eksperimentų metodikos .....	106
9.2.	Rezultatai ir aptarimas .....	106
9.3.	Išvados .....	108
	BENDROSIOS IŠVADOS .....	109
	LIST OF REFERENCES .....	111
	CURRICULUM VITAE .....	125



## ABBREVIATIONS

---

<b>Acronym</b>	<b>Meaning</b>
DFT	Density Functional Theory
DOS	Density of States
VC	Virtual Crystal
LA	Longitudinal Acoustic
LO	Longitudinal Optical
CPA	Coherent Potential Approximation
STE	Self-Trapped Exciton
MC	Monte Carlo
TR	Time Resolution
CTR	Coincidence Time Resolution
PL	Photoluminescence
CL	Cathodoluminescence
LHC	Large Hadron Collider
FCC	Future Circular Collider
CMS	Compact Muon Solenoid
HL	High Luminosity
HL-LHC	High Luminosity Large Hadron Collider
SiPM	Silicon Photomultiplier

PMT	Photomultiplier
PET	Positron Emission Tomography
LED	Light-Emitting Diode
IQE	Internal Quantum Efficiency
QW	Quantum Well
MOCVD	Metalorganic Chemical Vapor Deposition
LITG	Light-Induced Transient Grating
TCSPC	Time-Correlated Single Photon Counting
IR	Infrared
UV	Ultraviolet
LYSO	$\text{Lu}_{2(1-x)}\text{Y}_{2x}\text{SiO}_5$
LSO	$\text{Lu}_2\text{SiO}_5$
YSO	$\text{Y}_2\text{SiO}_5$
GAGG	$\text{Gd}_3\text{Al}_{5x}\text{Ga}_{5(1-x)}\text{O}_{12}$
LuGAGG	$\text{Lu}_{3y}\text{Gd}_{3(1-y)}\text{Al}_{5x}\text{Ga}_{5(1-x)}\text{O}_{12}$
GYAGG	$\text{Gd}_{3(1-y)}\text{Y}_{3y}\text{Al}_{5x}\text{Ga}_{5(1-x)}\text{O}_{12}$
InGaN	$\text{In}_x\text{Ga}_{1-x}\text{N}$
AlGaN	$\text{Al}_x\text{Ga}_{1-x}\text{N}$

## INTRODUCTION

Inorganic crystalline scintillation materials play an essential role in the detection of ionizing radiation. Scintillator-based radiation detectors are actively used in high energy physics experiments, in particular, in LHC experiments at CERN, in medical imaging, particularly, for PET devices, environmental monitoring and security systems. Inorganic crystals allow combining the high material density ensuring a high stopping power with the flexibility in variation in luminescence properties by varying the material composition and choosing activator ions.

Over the last years, cerium-doped oxide compounds, in particular, oxyorthosilicates and garnets, have gained the greatest popularity as scintillation materials for radiation detectors [1]. Such materials are characterized by high density, high light yield, and fast scintillation decay. Ternary and quaternary compounds with the garnet or oxyorthosilicate structure have demonstrated outstanding scintillation properties [2]. Incorporating ions with intermediate ion radii in such materials allowed substantially improving their performance by engineering the band gap and the crystal field acting on the activator ion and affecting the energy levels of the ion [3], [4]. Furthermore, the modulation of crystal field due to composition fluctuations in the alloys results in a decrease in the diffusion length of free carriers, that leads to increasing the density of geminate electron-hole pairs and, consequently, increasing the excitation transfer efficiency to luminescent centers. The further engineering of fast multicomponent crystalline scintillation materials requires a deep theoretical understanding of the impact of compositional disorder on the transient processes in such systems. Most of these processes cannot be directly measured, and should be studied by analyzing integral response, for instance, that obtained by the transient optical absorption technique [5], [6].

Moreover, the study of excitation transfer through the crystalline matrix with compositional fluctuations is important also for better understanding the electrical and optical properties of compound semiconductors. In-depth understanding of the relaxation process of thermalized carriers in compound semiconductors becomes especially important for improving the IQE, in particular, in InGaN-based LEDs and LDs emitting in the deep green region and AlGaIn LEDs emitting in the UV region [7]. The InGaIn emitters are of especial importance for better color rendering of LED-based displays or LD-based projectors. Meanwhile, AlGaIn-based UV LEDs can be used as UV light

sources to replace the toxic mercury lamps, which pollute the environment [8], [9], in water purification and other applications.

## MAIN GOAL AND TASKS

This study is aimed at developing a theoretical description of the effect of compositional disorder in multicomponent crystalline scintillators and semiconductors on excitation transport through the compound and, as a consequence, on the spectral and temporal properties of the light emission by compound scintillators and semiconductors. To follow the main goal, the following tasks have been addressed:

1. Developing a model of substitutional ion distribution in ionic compound scintillators and applying this model to Ce-doped LYSO solid solution, as a prospectively fast scintillator for high-luminosity high energy physics experiments and high-spatial-resolution medical imaging.
2. Developing a theoretical description of the elastic scattering of non-equilibrium carriers on the disorder-induced fluctuations of crystal potential and applying it to LYSO system for calculating the alloy scattering rate for free nonequilibrium electrons. Comparison of the obtained results with the electron-phonon scattering rate in the virtual crystal approximation.
3. Developing a generalized theoretical description of the interaction of nonequilibrium carriers with phonons in compound scintillators and semiconductors with strong compositional disorder.
4. Evaluating the heavy hole diffusion coefficient in AlGaN semiconductor. Verifying the obtained results by comparing with the experimental data obtained by using the light-induced transient grating technique.
5. Developing a kinetic Monte Carlo model of excitation transfer through gadolinium-containing garnet host and applying it to Ce-doped LuGAGG scintillator for simulating the scintillation decay kinetics, exploitation of the difference in the decay rate at the excitation with high energy electrons in cathodoluminescence experiments and the photoexcitation resonantly to the emitting  $5d_1$  level of the activator level  $Ce^{3+}$  for revealing the contribution of

excitation transfer via gadolinium subsystem in the scintillator matrix.

6. Revealing the role of aliovalent codoping on the excitation transfer in Ce-doped garnet-type scintillators.
7. Studying the impact of the compositional disorder in multicomponent garnet scintillators on spectral properties of emitting cerium ions.

## NOVELTY

The Boltzmann transport equation exploiting the Bloch eigenvectors and their eigenstates as well as the matrix elements of the derivative of the self-consistent potential in a crystal cell is a well-known approach to calculate the mobility of non-equilibrium carriers, both in a regular crystal and in a big supercell of a compound scintillator or semiconductor [10], [11]. However, such approach is extremely time-consuming even at the calculation capacities potentially available today. Meanwhile, the existing quasiclassical methods for simulating the carrier migration through the compound crystalline scintillators and semiconductors exploiting the alloy scattering rate in the Born approximation [12], [13] and taking into account a certain modification of the scattering rate of non-equilibrium carriers due to phonon emission and absorption [13] provide a low accuracy at the carrier energies close to the mobility threshold and can be applied only to a few crystalline systems. The coherent potential method [14] and the local landscape method [15] provide a quite accurate estimation of energy uncertainty in disordered crystalline media for carrier states of the virtual crystal [16] and can be used to modify the existing quasiclassical methods.

The main novel results obtained in this thesis are:

1. In this study, a general description of non-equilibrium carrier migration in compound crystalline scintillators and semiconductors is developed. Modifications of the quasiclassical expressions for the alloy scattering rate and the electron(hole)-phonon scattering rates exploiting the CPA and local landscape methods, respectively, are provided. The developed description can be used to simulate the carrier dynamics in scintillators and semiconductor compounds with strong potential disorder.

2. In contrast to previous models, the exploited methods are valid in the entire range of carrier energy. The developed approach is demonstrated to be functionable in the description of the hole diffusion in multicomponent semiconductors and enabled calculation of the dependence of the ambipolar diffusion in ternary AlGaIn that is in a good correspondence to that experimentally obtained using the light-induced dynamic gratings technique. New features of heavy hole scattering are revealed by fitting theoretical and experimental results and included in the calculations of the scattering rate.

3. The elastic scattering of high-energy electrons on core potential fluctuations in LYSO scintillation crystal is described and revealed to be important.

4. The excitation transfer to emitting  $\text{Ce}^{3+}$  ions via the Gd-subsystem in Ce-activated multicomponent garnet-type scintillators is quantitatively demonstrated by calculating the luminescence decay kinetics at excitations with high-energy electrons and photoexcitation resonantly to the emitting level of  $\text{Ce}^{3+}$ .

5. The involvement of gadolinium multiplet  ${}^6\text{I}$ , in addition to the lowest multiplet  ${}^6\text{P}$ , in the excitation transfer via the Gd subsystem in garnet-type lattice is revealed.

6. By comparing the luminescence decay kinetics in photo- and cathodoluminescence measurements and those obtained theoretically, a mechanism of the decay acceleration due to aliovalent cooping is revealed.

7. Splitting of the emission band of cerium ions due to a compositional disorder in Ga-Al subsystem of Ce-doped multicomponent scintillator is revealed.



## DEFENSIVE STATEMENTS

1. The effect of compositional disorder on the migration of non-equilibrium electrons in lutetium yttrium oxyorthosilicates is weaker than the effect of phonon scattering.
2. The heavy-hole diffusivity in AlGaN compound semiconductor at room temperature and low carrier density is predominantly determined by the process of hopping over potential barriers due to phonon absorption and emission.
3. Gadolinium multiplet  ${}^6I$ , in addition to the lowest multiplet  ${}^6P$ , is important in the excitation transfer via the Gd subsystem in garnet-type lattice.
4. The cerium emission band in multicomponent garnet-type scintillators GYAGG:Ce consists of two pairs of lines due to compositional disorder of the crystal resulting in different content of Al and Ga in two closest coordination spheres of the emitting  $Ce^{3+}$  ion.

## AUTHOR'S CONTRIBUTION

The model for the excitation transfer in disordered crystals has been developed by the author after the discussions of the processes important for the applications of the model for specific scintillators and compound semiconductors in discussions with my thesis supervisor and my colleagues at the Institute of Photonics and Nanotechnology at Vilnius University, the mentor of my former research on the field Prof. Mikhail Korzhik, and my supervisor and indispensable adviser in the theory of solid state physics and scintillator materials Prof. Andrey Vasil'ev. All the calculations according to the models were performed by the author. The code used for the Monte Carlo simulations according to the model was created by the author from scratch using C++ language. All the experimental data used in this work were obtained by my colleagues at the Institute of Photonics and Nanotechnology, Vilnius University.

## LIST OF PUBLICATIONS

- A1. Y. Talochka, A. Vasil'ev, M. Korzhik, and G. Tamulaitis, [Impact of Compositional Disorder on Electron Migration in Lutetium–Yttrium Oxyorthosilicate Scintillator](#), *J. Appl. Phys.*, vol. 132, no. 5, p. 053101, Aug. 2022.
- A2. Y. Talochka, R. Aleksiejūnas, Ž. Podlipskas, J. Mickevičius, G. Tamulaitis, [Evaluation of Ambipolar Diffusion Coefficient in  \$Al\_xGa\_{1-x}N\$  Semiconductor](#), *J. Alloys Compd.*, vol. 969, p. 172475, Dec. 2023.
- A3. Y. Talochka, S. Nargelas, Ž. Podlipskas, M. Kucera, Z. Lucenicova, G. Tamulaitis, [Acceleration of emission decay in Ce-doped Gd-containing garnets by aliovalent codoping due to blocking excitation transfer via gadolinium subsystem](#), *Radiat. Phys. Chem.*, vol. 218, p. 111589, May 2024.
- A4. S. Nargelas, Y. Talochka, A. Vaitkevičius, G. Dosovitskiy, O. Buzanov, A. Vasil'ev, T. Malinauskas, M. Korzhik, and G. Tamulaitis, [Influence of Matrix Composition and Its Fluctuations on Excitation Relaxation and Emission Spectrum of Ce Ions in  \$\(Gd\_xY\_{1-x}\)\_3Al\_2Ga\_3O\_{12}:Ce\$  Scintillators](#), *J. Lumin.*, vol. 242, p. 118590, Feb. 2022.

## OTHER RELEVANT PUBLICATIONS

- B1. G. Dosovitskiy, A. Golutivin, I. Guz, R. Jacobsson, M. Korzhik, V. Mechinsky, Y. Talochka, G. Tamulaitis, A. Schopper, and E. Shmanin, [Time and Energy Resolution with SPACAL Type Modules Made of High-Light-Yield Ce-Doped Inorganic Scintillation Materials: Spillover and Background Noise Effects](#), *Nucl. Instrum. Methods Phys. Res. Sect. Accel. Spectrometers Detect. Assoc. Equip.*, vol. 999, p. 165169, May 2021.
- B2. M. Korzhik, K.-T. Brinkmann, V. Dormenev, M. Follin, J. Houzviccka, D. Kazlou, J. Kopal, V. Mechinsky, S. Nargelas, P. Orsich, Z. Podlipskas, V. Sharyy, S. Sykorova, Y. Talochka, G. Tamulaitis, D. Yvon, H.-G. Zaunick, [Ultrafast PWO scintillator for future high energy physics instrumentation](#), *Nucl. Instrum. Methods Phys. Res. Sect. Accel. Spectrometers Detect. Assoc. Equip.*, vol. 1034, p. 166781, Jul. 2022.

- B3. G. Tamulaitis, S. Nargelas, M. Korjik, V. Mechinsky, Y. Talochka, A. Vaitkevičius, A. Vasil'ev, [\*Transient optical absorption as a powerful tool for engineering of lead tungstate scintillators towards faster response\*](#), *J. Mater. Chem. C*, vol. 10, no. 25, pp. 9521–9529, Jun. 2022.
- B4. G. Tamulaitis, S. Nargelas, Y. Talochka, A. Vaitkevičius, M. Korjik, V. Mechinsky, R. Paramatti, I. Dafinei, M.T. Lucchini, E. Auffray, N. Kratochwil, [\*Transient Optical Absorption Technique to Test Timing Properties of LYSO:Ce Scintillators for the CMS Barrel Timing Layer\*](#), *Radiat. Phys. Chem.*, vol. 206, p. 110792, May 2023.

### LIST OF CONFERENCE PRESENTATIONS

- C1. Y. Talochka, A. Vasil'ev, M. Korjik, G. Tamulaitis, *Impact of disorder in LYSO cationic subsystem on migration of nonequilibrium carriers*, 76th Crystal Clear Collaboration Meeting, Switzerland, Geneva, CERN, Nov. 17-18, **2021**. (Oral)
- C2. Y. Talochka and G. Tamulaitis, *Impact of compositional disorder on electron transport in multicomponent scintillation crystals*, 24-th International Conference-School "Advanced Materials and Technologies 2022", Lithuania, Palanga, Aug. 22-26, **2022**. (Poster)
- C3. Y. Talochka and G. Tamulaitis, *Influence of Compositional Disorder on Electron Transport in Lutetium-Yttrium Oxyorthosilicate Scintillator*, 2022 IEEE NSS MIC RTSD Conference, Italy, Milano, Nov. 5-12, **2022**. (Poster)
- C4. Y. Talochka, S. Nargelas, G. Tamulaitis, *Energy transport through gadolinium subsystem in Ce-doped garnet scintillators*, 80th Crystal Clear Collaboration General Meeting, Switzerland, Geneva, CERN, Nov. 23-24, **2023**. (Oral)

# 1. LITERATURE REVIEW

## 1.1. Fast scintillators and their applications in physical measurements

Scintillator-based radiation detectors have been exploited in physical measurements for more than a century. Scintillation is luminescence induced by ionizing radiation in a transparent dielectric medium. The scintillation process was observed in various organic and inorganic crystalline media [17], [18], [19], fluids [20], [21], [22], [23], and gases [24], [25]. In this work, crystalline inorganic scintillation materials were discussed. The usage of inorganic crystalline media allows combining high material density, i.e., high stopping power, with a wide variation in emission properties by choosing the material composition and activating ions.

Figure 1 illustrates the general scheme of scintillator-based radiation detectors. A scintillation crystal is coupled to a photodetector (SiPM or PMT). The absorbed energy of ionizing radiation is converted via scintillation mechanism to VU or visible light. The scintillation light can be detected using the photodetector generating an electrical signal, which is processed by readout electronics.

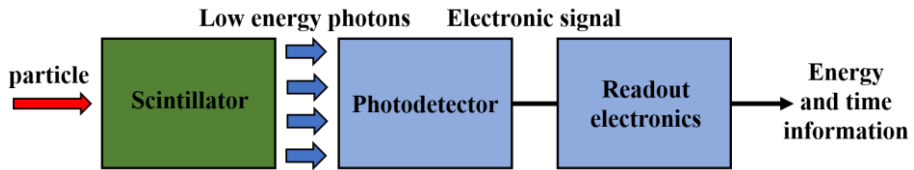


**Fig. 1.1.** Schematic of a scintillator-based radiation detector.

Currently, such industries as environmental monitoring and security systems require innovations in the scintillator field. In addition, applications of scintillator-based radiation detectors in high energy physics experiments, in particular, at HL-LHC and FCC [26], as well as for medical imaging like the time-of-flight positron emission tomography [27], require scintillators with fast luminescence response. Since the operation speed of photodetectors and readout electronics has been substantially improved over the last ten years, the development of fast radiation detectors requires improving the timing properties of scintillators. For instance, the high intrinsic time resolution along with a fast luminescence decay in scintillation materials become substantially important to suppress the pile-up effect at increasing the integrated luminosity at HL-LHC [B1]. In addition, radiation tolerance becomes the second primary property of scintillation materials to be exploited in future radiation detectors

at HL-LHC and other high energy physics facilities [28]. The same requests might be expected for scintillator-based radiation detectors at FCC operating in  $hh$  mode. The requirements for future detectors at HL-LHC and FCC have been summarized in Ref. [29]. The need for combining high energy and temporal resolutions along with high radiation tolerance of scintillator-based radiation detectors is pointed out there. Meanwhile, further enhancement of PET technology, in particular, to achieve high spatial resolution, also requires improving the timing properties of scintillation materials [30].

There are many high-performance inorganic crystalline scintillators which can be divided into two groups: self-activated and activated materials. The most extensively used in high energy physics experiments, in particular for homogeneous electromagnetic calorimeters, self-activated scintillator is lead tungstate ( $\text{PbWO}_4$ , PWO) [31], [32]. PWO was developed as a part of the LHC program three decades ago [33], [34], [35], [36], [37]. Lead tungstate scintillator exhibits a fast scintillation response (3.6 ns of decay time for PWO-II and 0.64 ns for PWO-Ultra Fast) and ensures a good radiation tolerance [37], [38], [A2]. Although PWO has low light yield (measured to be 15 phe/MeV for PWO-II and 7 phe/MeV for PWO-Ultra Fast [B2]), homogeneous PWO-based calorimeters provide the best energy resolution ( $< 1\%$  at the gamma-particle energy larger than 20 GeV) [39], [40], mainly due to the high stopping power [37]. Meanwhile, alkali halide scintillators, mainly CsI and NaI, demonstrating relatively high efficiency of radiation energy conversion (the light yield of up to 107000 ph/MeV is reported in pure CsI [41] and up to 60000 ph/MeV in CsI:Tl [42], [43]) and having low production cost are also extensively used in radiation detectors, in particular, for environmental monitoring and security systems [44]. However, such materials are characterized by substantially slower scintillation decay [45], [46]. Currently, the most promising scintillators for fast radiation detectors are Ce-activated garnets and oxyorthosilicates [1]. Such scintillators are characterized by high radiation tolerance [47], [48]. Ce-doped garnet scintillators are shown to be efficient scintillators exhibiting light yield of up to  $\sim 58000$  ph/MeV in  $\text{Gd}_3\text{Al}_5\text{Ga}_{5(1-x)}\text{O}_{12}:\text{Ce}$  (GAGG:Ce) [49] and 20000-44000 ph/MeV in many other Ce-doped garnets. The fast component of scintillation decay in garnet scintillators varies from 20 to 70 ns [50], [51], [52], [53]. Ce-doped oxyorthosilicates, such as  $\text{Lu}_2\text{SiO}_5:\text{Ce}$  (LSO:Ce) and  $\text{Lu}_{2(1-x)}\text{Y}_{2x}\text{SiO}_5:\text{Ce}$  (LYSO:Ce) crystals having similar timing properties, exhibit a short luminescence rise and decay times ( $\sim 70$  ps and  $\sim 40$  ns, respectively), high light yield ( $\sim 30000$  ph/MeV), and a small contribution of slow components in the scintillation kinetics [1], [54]. Herewith, such multicomponent garnets and

oxyorthosilicates demonstrated outstanding results in the coincidence time measurements [5], [55]. It is important to note that the CMS collaboration aims at using the LYSO:Ce scintillator for a new detector layer (the Barrel Time Layer) with a high time resolution (30-60 ps), containing  $\sim 250\,000$  crystal bars with SiPM readout [26]. In addition, nowadays, LYSO:Ce is a scintillator with the best set of properties for PET technology [30].

Such high performance of Ce-doped garnets [6], [55], [56] and oxyorthosilicates [5] as well as several other activated scintillators: LaBr<sub>3</sub>:Ce [57], NaI:Tl [58], [59] and CsI:Tl [60], and self-activated PbWO<sub>4</sub> scintillator [61], was achieved by aliovalent codoping. For instance, a strong quenching of the luminescence decay due to the formation of a new type of magnesium-induced emitting cerium centers with a faster emission time in Lu<sub>0.75</sub>Gd<sub>2.25</sub>Ga<sub>2.5</sub>Al<sub>2.5</sub>O<sub>12</sub>:Ce,Mg scintillator was reported in Ref. [62], [63]. In addition, incorporating ions with intermediate ion radii, in particular, in multicomponent garnets (Lu,Y,Gd)<sub>3</sub>(Al,Ga)<sub>5</sub>O<sub>12</sub> allowed substantially improving the performance by engineering the band gap and the crystal field acting on the activator ion and affecting the energy levels of the ion [3], [4]. Moreover, modulating the conduction band edge due to compositional disorder induced by incorporating Lu and Y ions into the gadolinium subsystem leads to a decrease in the diffusion length of free carriers, increasing the density of geminate electron-hole pairs and, consequently, increasing the efficiency of excitation transfer to luminescent centers [2]. All these effects allowed accelerating the leading edge of scintillation kinetics in the discussed systems.

## 1.2. Role of timing parameters of a scintillation material in the formation of intrinsic time resolution

Currently, the coincidence time resolution (CTR) measuring by using correlated annihilation  $\gamma$ -quanta from a <sup>22</sup>Na source is an important parameter reflecting the response time of the entire radiation detector [64]. CTR is proportional to the root of the product of the luminescence rise  $\tau_r$  and decay  $\tau_d$  times divided by the light yield  $LY$ :  $CTR \propto \sqrt{\frac{\tau_r \tau_d}{LY}}$  [65]. Thus, the high time resolution of a scintillation material might be achieved by reducing the rise and decay times and by an increase in the light yield. The scintillation decay time is an inherent property of certain emitting centers in a certain crystal host and might usually be decreased only at the expense of the light

yield [6]. The value of  $LY$  depends on the bandgap of the scintillation crystal  $E_g$ , the efficiency of energy transfer to luminescence centers  $S$ , and the efficiency of radiative recombination of luminescence centers  $Q$  as  $LY \propto \frac{SQ}{E_g}$  [66]. Thus, the light yield of certain scintillator can be improved by increasing efficiencies  $S$  and  $Q$  [3], [4]. It is worth noting that the efficiency of radiative recombination of cerium ions in a garnet host is already close to 90% [3]. Thus, the improvement of the efficiency of energy transfer to luminescence centers becomes a primary way to improve the scintillator time resolution. Moreover, the scintillation rise time is predominantly determined by the processes of excitation transfer to emitting centers and might be varied in the entire range of picosecond domain [55]. Thus, the improvement of the efficiency of energy transfer to luminescence centers also allowed accelerating the leading edge of the scintillation kinetics and, consequently, improving the time resolution. However, further enhancement of the energy transfer efficiency in compound scintillators with strong compositional disorder requires the development of a theoretical description of the effect of compositional disorder on the excitation transfer processes.

### 1.3. Ternary nitride semiconductors and their applications in electronic and optoelectronic devices

Similar phenomena of excitation transfer are of importance also in multicomponent semiconductors, in particular, ternary nitrides [67]. The difference in the band gaps of compound components is a property engineered in such materials. The band gaps of GaN, AlN, and InN crystals are equal to 3.5 eV, 6.2 eV, and 0.63 eV, respectively [68], [69]. That allows producing LEDs with light emission wavelength in a wide range from visible to UV light. The carrier localization effect induced by compositional disorder in ternary compounds of nitrides is important for the electronic and optical properties of LEDs [70], [71], [72], [73], [74]. This effect allowed reaching the defect insensitivity and, consequently, the 90% internal quantum efficiency (IQE) of (In,Ga)N-based LEDs operating in the blue to violet spectral range [75], [76]. However, the IQE is still substantially lower in  $\text{In}_x\text{Ga}_{1-x}\text{N}$  (InGaN) emitters in the deep green region that are needed for better color rendering of LED-based displays or laser-diode-based projectors and in  $\text{Al}_x\text{Ga}_{1-x}\text{N}$  (AlGaN) LEDs emitting in UV region [7]. Such AlGaN-based UV LEDs could replace mercury lamps commonly used as UV light sources containing toxic mercury that pollutes the environment [8], [9]. Moreover, AlGaN-based UV LEDs can

be used for water purification, because UV light is a strong disinfectant. Thus, a deeper study of carrier dynamics in ternary and quaternary III-nitrides with strong carrier localization is needed to improve the efficiency of light emitters based on these semiconductors.

#### 1.4. Transient processes in inorganic crystalline materials

##### 1.4.1. Scintillators

The scintillation process starts at the moment when a particle enters into the scintillator volume. If a particle has an electrical charge, it transfers energy to the electrons of the crystal through the Coulomb interaction (ionization and Bremsstrahlung energy losses). Neutral particles lose energy due to interactions with the atom nuclei in the medium. Herewith, the final products of the reaction can be gamma particles, electrons, protons, heavier charged particles such as alpha particles, etc. Gamma particles lose energy in the processes of photoelectric effect, Compton scattering, and electron-positron pair generation. All these processes eventually lead to the creation of secondary high-energy electrons or heavy charged particles which participate in the following stages of the excitation evolution [66], [77], [78]. In the current work, the evolution of excitations produced by high-energy electrons in inorganic crystalline scintillators was considered.

Currently, the results of studies demonstrating a deeper understanding of multiple processes of energy conversion through all scintillation stages in conventional materials, such as NaI:Tl [79], [80], [81], [82], CsI:Tl,Na,In [80], [81], [83], [84], [85], YAP:Ce [81], [83], PWO:La,Y [B2], etc. were reported. A complete description of the scintillation process in regular crystals as well as kinetic models of energy relaxation neglecting the compositional disorder effect in multicomponent scintillators was presented in Ref. [66].

Figure 2 shows the general scheme of the time evolution of energy distribution of electronic excitations during the processes of electron-electron scattering, thermalization of secondary electrons and holes as well as alloy scattering of them, capture of electrons and holes by traps and their self-trapping or localization in disorder-induced potential wells, exciton creation, interaction of excitations, as well as further excitation of luminescence centers, and finally photon emission or non-radiative recombination of excitations.



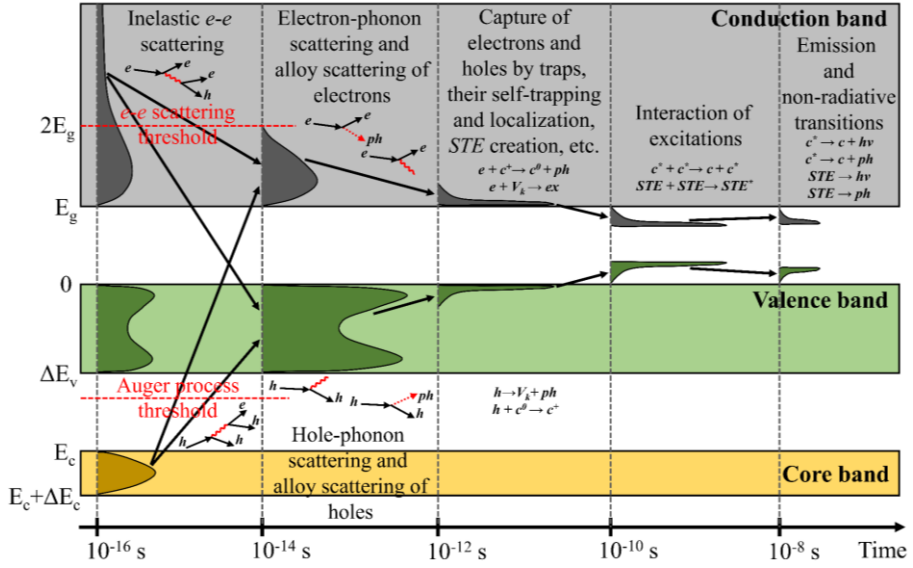


**Fig. 1.2.** Relaxation routes of electronic excitations in inorganic crystalline scintillators:  $e$  is an electron,  $h$  is a hole,  $ph$  is a phonon,  $h\nu$  is a photon,  $V_k$  is a self-trapped hole,  $STE$  is a self-trapped exciton, and  $c$  is an emission center [66].

The valence band with the top energy at  $E_v = 0$  and the bandwidth  $\Delta E_v$  and the conduction band are separated by the band gap  $E_g$ . For simplicity, only one core band with top energy  $E_c$  and the bandwidth  $\Delta E_c$  is indicated. The scheme depicts five major stages.

The first stage starts with the creation of secondary electrons and holes due to the interaction of high-energy electrons with the material. At very high energies of an incident particle, the excitations are predominantly hot electrons in the conduction band and deep holes created in inner core bands. Then, a large number of secondary electrons in the conduction band and hole in the valence band are produced through inelastic electron-electron scattering and Auger processes within a very short time scale ( $10^{-16}$ – $10^{-14}$  s). The multiplication of electronic excitations stops at the end of this stage. As the result, all electrons in the conduction band have an energy smaller than  $2E_g$  ( $e$ - $e$  scattering threshold) and all holes occupy the valence band if there is no core band lying above the threshold for Auger processes. A theoretical description of the multiplication processes has been proposed by A.N. Vasil'ev in Ref. [86]. Such approach exploits the dielectric permittivity in the entire energy range and the Brillouin zone, which can be calculated using the density functional theory (DFT) methods [87]. Meanwhile, the imaginary part

of the dielectric permittivity can be calculated using the photoexcitation cross section presented in the Evaluated Photon Data Library [88] taking into account the correction of the population and the energy of atomic shells. Then, the Kramers-Kronig relations can be used to obtain the real part of the dielectric permittivity [89]. In addition, the inelastic electron-electron scattering in scintillators can be properly simulated by using the GEANT4 package [90]. However, the GEANT4 package is designed to properly describe amorphous materials as a combination of atoms without coupling between them taken into account. The approach is often acceptable also for the simulation of the interaction of a crystalline material with high-energy particles. However, the approach leads to an incorrect distribution of energy deposition in a track of a charged particle with low kinetic energy in a crystal. Thus, this package is inappropriate for studying the further thermalization of carriers with their energy below the ionization threshold.

The second stage is electron and hole thermalization due to phonon emission and absorption. The phonon relaxation in a regular crystal as well as in a substitutional solid solution can be properly described by the DFT methods [11], [91]. It is worth noting that these calculations are complex and time-consuming. Instead, the quasiclassical approach to simulate the electron(hole)-phonon interactions in a regular crystal can be used [92], [93]. This approach has been exploited only in a semiquantitative quasiclassical description of the scattering of free non-equilibrium electrons (holes) due to phonon emission or absorption in a substitutional solid solution [13]. The pseudopotential-based technique to build fluctuating conduction (valence) band edge due to compositional disorder was exploited in that study. According to this study, the electron(hole)-phonon scattering rate in a disordered system can be calculated by integrating the rate in the virtual crystal (VC) approximation over the pseudopotential landscape. The elastic scattering of free non-equilibrium carriers on pseudopotential fluctuations was also considered there along with the electron(hole)-phonon scattering. All the techniques discussed above were adopted for cubic lattice with a single atom in a cell. Thus, further investigations of the disorder effects on the scintillation process require the extension of the proposed technique to multicomponent scintillators.

The third stage is the transfer of thermalized carriers to the centers of their radiative recombination. This transfer might be affected by carrier localization on shallow defects as well as exciton creation in the scintillation material. For instance, electrons and holes can be captured by different traps or self-trapped in the crystal lattice. The localization of excitations can be sometimes

accompanied by displacements of atoms (defect creation, photo-stimulated desorption). The processes of autolocalization of electrons, holes, and excitons as well as their further decay were in-depth discussed by R.T. Williams and K.S. Song in their book [94]. In addition, excitations can be localized in potential wells as the result of phonon emission in a substitutional solid solution. Localization of an electron and a hole in the same potential well can contribute to their Coulomb interaction leading to exciton formation. Meanwhile, electrons and holes localized at different potential minima can hardly form an exciton [13]. The probability for geminate electron-hole pairs to form excitons can be estimated using a simple black-capture-sphere model or a more sophisticated Onsager model [66], [92]. If the electron and hole are not correlated at the initial moment, the black-capture-sphere model describes the bimolecular recombination process. The black-capture-sphere model can also be used to estimate the probability of carrier capture by emission centers. However, the quantitative description of the problem of electron and hole binding to an exciton in a disordered crystalline media is still not addressed.

The last two stages are characterized by the migration of relaxed excitations and radiative and non-radiative recombination. The energy transfer from a donor to an acceptor can be described by the dipole-dipole mechanism of energy transfer [95]. In the case of the excitation diffusion through the donor subsystem occurring due to dipole-dipole transfers, the general formula describing the luminescence decay kinetics taking into account such diffusion-controlled dipole-dipole energy transfer was derived by Yokota and Tanimoto [96]. This technique was exploited in Ref. [97] to describe the luminescence decay kinetics of gadolinium ions in LuAG:Ce,Gd epitaxial films measured at  ${}^6P_j$ - ${}^8S_{7/2}$  ( $Gd^{3+}$ ) emission line under pulsed excitation to  ${}^6I(Gd^{3+})$  term at 274 nm. In the case when the donor is a crystal-building ion, the Dexter mechanism of energy transfer should also be taken into account. A description of the donor-donor ( $Tb^{3+} \rightarrow Tb^{3+}$ ) and donor-acceptor ( $Tb^{3+} \rightarrow Ce^{3+}$  and  $Ce^{3+} \rightarrow Tb^{3+}$  back-transfer) energy transfers through the dipole-dipole and the exchange mechanisms in  $(Lu,Tb)_3Al_5O_{12}:Ce$  phosphors was presented in Ref. [98]. A deep understanding of the mechanism of the energy transfer through the gadolinium subsystem in garnet scintillators is important to reduce the contribution of slow components in the scintillation decay. A kinetic Monte Carlo model with tracking excitation position taking into account both the dipole-dipole and Dexter mechanisms of energy transfer from donor  ${}^6P(Gd^{3+})$  to acceptor  $5d_2$  ( $Ce^{3+}$ ) in  $Lu_3yGd_{3(1-y)}Al_{5x}Ga_{5(1-x)}O_{12}$  (LuGAGG) crystal host was presented by M. Korzhik et al. in Ref. [53]. The proposed model provided a semiquantitative description of the effect of increasing fractions of short and

very long components in the scintillation kinetics due to breaking the integrity of the gadolinium sublattice in LuGAGG:Ce scintillator.

There is a possibility of interaction between excitations leading to a decrease in the number of excitations. For instance, such effect of STE-STE quenching was experimentally observed and theoretically studied in CdWO<sub>4</sub> [99], CaMoO<sub>4</sub> and ZnMoO<sub>4</sub> [100], and PWO [B3].

#### 1.4.2. Semiconductors

The typical energies of non-equilibrium carriers in semiconductor devices are not larger than the multiplication threshold. Meanwhile, most of the studies discussed for scintillation materials are also applicable to semiconductors. Herewith, the time and energy distribution of non-equilibrium carriers in III-nitrides are usually simulated using the rate equations. For free electron hole pairs, the ABC model is usually exploited. The model describes the decay rate for carrier density  $n$  by expression  $An + Bn^2 + Cn^3$  where  $A$  and  $C$  are the coefficients for nonradiative Shockley–Read–Hall and Auger recombination, respectively, whereas  $B$  is the coefficient of bimolecular radiative recombination [101]. This model allowed explaining a decrease in the luminescence efficiency at increasing carrier density [102] by nonradiative Auger recombination [102], [103]. This interpretation was evidenced by direct measurements of Auger electrons in InGaN LEDs [104]. Moreover, it is shown that trap-assisted Auger recombination might be important in InGaN QWs of lower quality [105], [106]. However, the ABC model doesn't allow properly describing the IQE and the recombination rate at the moderate or low level of carrier densities and in compound semiconductors with strong carrier localization.

The localization effect can be described in a limiting model by assuming that a certain electron-hole pair localized in the same potential cluster after the thermalization stage immediately forms an exciton. Such localized excitons distributed in energy below the mobility edge can move through the crystal by hopping with phonon emission and absorption. Such excitons can recombine radiatively or reach nonradiative recombination centers. Thus, the dynamics of such excitons might be simulated by using the Monte Carlo method [107]. The exciton hopping mechanism allowed explaining a decrease in the luminescence efficiency by the competition of nonradiative recombination and localization of free carriers without involving Auger processes [108]. However, this model contains many parameters that cannot be directly

measured and are extracted by fitting the simulation results with multiple dependencies of photoluminescence parameters on temperature and excitation intensity.

The carrier mobility in compound semiconductors can be estimated using the Schrödinger-Poisson equations taking into account the fluctuating crystal potential. Such method was exploited in Ref. [109] to calculate the electron mobility in InGaN quantum wells. The result is well in consistence with the experimental values that proved a significant impact of the potential fluctuations. However, the calculations using this approach are complex and time-consuming. Meanwhile, in the compounds with a weak disorder, the virtual crystal approximation assigning interpolated properties to the disordered atoms can be used [16]. The disorder is introduced into the description of compound semiconductors through dopants [110].

The confining potential affecting the nonequilibrium carriers in compounds with potential disorder can be simulated using the localization landscape method [73], [74], [111] and the low-pass filter approach [112], [113]. The localization landscape approach has been exploited to simulate the dependence of the diffusion length of minority carriers on the density of majority carriers in (In,Ga)N and (Al,Ga)N quantum-well LEDs [114].

All these approaches lead to the simulation of carrier migration by taking into account only the features of the energy distribution of nonequilibrium carriers in a random alloy and use the hole and electron mobilities of the alloy constituents as the energy-independent input parameters. To properly simulate the carrier transport through a compound semiconductor with strong compositional disorder, the electron(hole)-phonon interactions should be considered from the first principles.

## 2. EFFECT OF COMPOSITIONAL DISORDER ON NON-EQUILIBRIUM FREE CARRIER TRANSPORT IN MIXED SCINTILLATORS

The effect of compositional disorder in compound scintillators on carrier transport was investigated theoretically in Ref. [13]. A thermodynamic Monte Carlo model to simulate the ion distribution in a substitutional solid solution was exploited in that study. This technique was applied to a mixed crystal with a single occupation node in a cubic cell. Meanwhile, multicomponent scintillators, such as ternary garnets and oxyorthosilicates, contain several tens of nodes occupied with substitutional ions. Thus, a model of multicomponent solid solution should be proposed for such systems. It is worth noting that there are many approaches to simulate the ion distribution in a substitutional solid solution ranging from simple phenomenological calculations to complicated applications of the density functional theory [115], [116], [117]. In the current chapter, a modification of the thermodynamic model proposed in Ref. [13] was suggested and applied to LYSO crystal. The developed model introduces a modification of the correction energy in a cation subsystem. In addition, the study [13] considers the process of the elastic alloy scattering of non-equilibrium electrons in a mixed crystal by using the transfer cross section in the Born approximation, which is not valid in the low-energy limit. To solve this problem, a non-perturbation method to calculate the elastic alloy scattering rate using the coherent potential approximation was proposed and described in the current chapter. This method was applied to LYSO solid solution. The obtained alloy scattering rates for non-equilibrium electrons in LYSO solid solution were analyzed by comparing the results with the rate of electron scattering due to phonon emission and absorption in the virtual crystal approximation.

### 2.1. Thermodynamic model of ion distribution in mixed crystalline scintillators

A ternary compound scintillator  $A_xB_{1-x}C$  of two binary ionic crystals AC and BC having the same spatial symmetry and similar lattice constants was considered in the current chapter. The scintillation crystals are usually grown by the Czochralski method [118]. This process is conducted slowly enough to assume that the occupation of each node occurs in the state of a local thermodynamic equilibrium. Thus, the probabilities of node  $\vec{r}_m$  occupation by

A ion  $P_A(\vec{r}_m)$  and B ion  $P_B(\vec{r}_m)$  in the local equilibrium state can be calculated using the canonical Gibbs distribution. As the result, a random node is occupied by A or B ion with the probabilities  $P_A(\vec{r}_m)$  and  $P_B(\vec{r}_m)$  at each step of the simulation. Herewith, the energy of A or B ion at a certain node is corrected by taking into account the occupation of surrounding nodes and can be expressed by the pair correction energy  $U_{I_1, I_2}(\vec{r})$  between two ions  $I_1$  and  $I_2$  (both might be either A or B) at the distance  $\vec{r}$ . The energy origin is set at the energy of the virtual crystal. The correction energy dependence on the distance for ionic crystals can be approximated as

$$U_{I_1, I_2}(\vec{r}) \sim \left( \frac{r_{min}}{|\vec{r}|} \right)^6, \quad (2.1)$$

where  $r_{min}$  is the minimum distance between occupied nodes. The expression (2.1) predominantly takes into account the contribution of ions within the two nearest coordination spheres to the correction energy. Herewith, the artificial correlation between the pairs separated by high interatomic distances is prevented. The total correction energies  $U_A(\vec{r})$  and  $U_B(\vec{r})$  can be written as two sums of the correction energies of the pairs of ions of the same and different types:

$$U_A(\vec{r}) = \sum_{\vec{r}_n \in \Omega_A} U_{A,A}(\vec{r}_n - \vec{r}) + \sum_{\vec{r}_n \in \Omega_B} U_{A,B}(\vec{r}_n - \vec{r}), \quad (2.2.1)$$

$$U_B(\vec{r}) = \sum_{\vec{r}_n \in \Omega_B} U_{B,B}(\vec{r}_n - \vec{r}) + \sum_{\vec{r}_n \in \Omega_A} U_{B,A}(\vec{r}_n - \vec{r}), \quad (2.2.2)$$

where  $\Omega_A$  and  $\Omega_B$  are the sets of vectors of nodes occupied by A and B ions, respectively.

Next, the occupation probabilities  $P_A(\vec{r}_m)$  and  $P_B(\vec{r}_m)$  have the following form:

$$P_A(\vec{r}_m) = \frac{1-x}{Z} e^{-\frac{U_A(\vec{r}_m)}{k_B T}}, \quad (2.3.1)$$

$$P_B(\vec{r}_m) = \frac{x}{Z} e^{-\frac{U_B(\vec{r}_m)}{k_B T}} \quad (2.3.2)$$

with

$$Z = (1-x) \sum_{\vec{r}_m \in \Omega} e^{-\frac{U_A(\vec{r}_m)}{k_B T}} + x \sum_{\vec{r}_m \in \Omega} e^{-\frac{U_B(\vec{r}_m)}{k_B T}}, \quad (2.3.3)$$

where  $Z$  is the statistical sum,  $\Omega$  is a set of vectors of empty nodes,  $T$  is the temperature, and  $k_B$  is the Boltzmann constant.

Finally, the model of  $A_xB_{1-x}C$  solid solution has three parameters. These parameters correspond to proportionality coefficients  $U_{I_1, I_2}(r_{\min})$  in expressions (2.3), i.e.  $U_{A,A}(\vec{r})$ ,  $U_{B,B}(\vec{r})$ , and  $U_{A,B}(\vec{r}) = U_{B,A}(\vec{r})$ . The corresponding dimensionless parameters were introduced for further convenience:

$$W_{A,A} = e^{-\frac{U_{A,A}(r_{\min})}{k_B T}}, \quad (2.4.1)$$

$$W_{B,B} = e^{-\frac{U_{B,B}(r_{\min})}{k_B T}}, \quad (2.4.2)$$

$$W_{A,B} = e^{-\frac{U_{A,B}(r_{\min})}{k_B T}}. \quad (2.4.3)$$

The  $W_{I_1, I_2}$  parameters describe the probability amplitude to find a pair of ions separated by the minimal distance between occupied nodes  $r_{\min}$  neglecting the influence of surrounding.

## 2.2. Simulation of the cation distribution in LYSO scintillator

$\text{Lu}_{2(1-x)}\text{Y}_{2x}\text{SiO}_5$  mixed crystal is a substitutional solid solution of two components  $\text{Lu}_2\text{SiO}_5$  and  $\text{Y}_2\text{SiO}_5$  having a monoclinic lattice with a space group  $C_{2c}$  and similar lattice constants: 14.283 Å and 14.564 Å for LSO and YSO, respectively [119]. Yttrium and lutetium cations occupy inequivalent lattice sites RE1 and RE2 with the oxygen coordination numbers of 7 and 6, respectively [119]. The minimum distance  $r_{\min}$  between Lu/Y nodes in  $\text{Lu}_{2(1-x)}\text{Y}_{2x}\text{SiO}_5$  crystal is equal to 3.4 Å. Lutetium and yttrium ions have similar ionic radii [120]. Thus, predominantly uniform cation distribution is the most likely case. However, three qualitatively different cation distributions were considered in this chapter: i) uniform distribution ( $W_{Lu,Lu} = W_{Y,Y} = W_{Lu,Y}$ ), ii) clustered distribution ( $W_{Lu,Lu} > W_{Lu,Y}$ ,  $W_{Y,Y} > W_{Lu,Y}$ ), and iii) preferably heterogeneous neighboring case. In the latter case, the probability of forming heterogeneous Lu-Y pairs is larger than that for forming homogeneous pairs Lu-Lu and Y-Y,  $W_{Lu,Y} > W_{Lu,Lu}$ ,  $W_{Lu,Y} > W_{Y,Y}$ .

Figure 2.1 shows the examples of the three cation distributions in  $15 \times 15 \times 15$   $\text{Lu}_{1.6}\text{Y}_{0.4}\text{SiO}_5$  supercell ( $x = 0.2$ ). Lattice parameters and node positions were taken as in Ref. [121], [122]. The average lattice vectors  $x\vec{a}_{i,YSO} + (1-x)\vec{a}_{i,LSO}$  were used to build the  $\text{Lu}_{1.6}\text{Y}_{0.4}\text{SiO}_5$  supercell, where  $\vec{a}_{i,YSO}$  and  $\vec{a}_{i,LSO}$  are the lattice vectors of YSO and LSO crystals, respectively.



The model parameters  $\{W_{Lu,Lu}, W_{Y,Y}, W_{Lu,Y}\}$  are chosen as  $\{1.0, 1.0, 1.0\}$  for uniform cation distribution,  $\{0.2, 0.2, 5.0\}$  for heterogeneous neighboring, and  $\{5.0, 5.0, 0.2\}$  for clustered cation distribution.

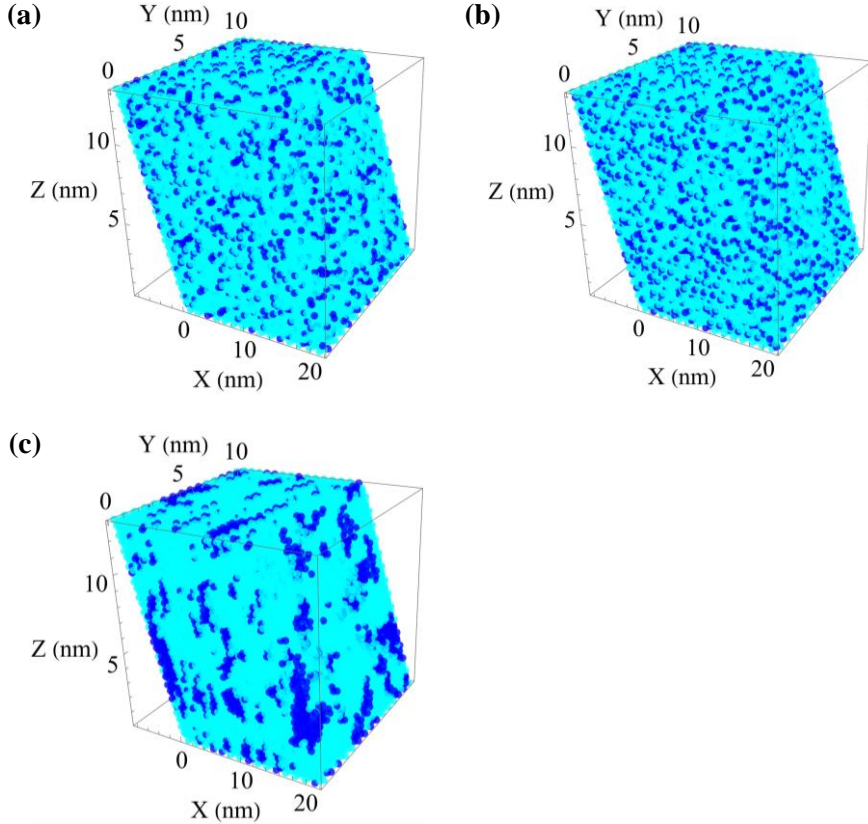


**Fig. 2.1.** Spatial distribution of lutetium (cyan) and yttrium (blue) cations in a  $\text{Lu}_{1.6}\text{Y}_{0.4}\text{SiO}_5$  supercell for uniform (a), heterogeneous neighboring (b), and clustered (c) cation distributions for parameters  $W_{ij}$  defined in the text [A1].

Figure 2.2 presents the correlation functions  $C_{Lu,Y}$  and  $C_{Y,Y}$  of the formation of cation pairs Lu-Y or Y-Y at a certain distance from each other in  $\text{Lu}_{1.6}\text{Y}_{0.4}\text{SiO}_5$  supercell for three typical cation distributions. The correlation functions  $C_{Lu,Y}$  and  $C_{Y,Y}$  for clustered distribution are substantially different at  $r_{min}$  and become equal at about  $20 \text{ \AA}$  (Fig. 2.2(c)). Meanwhile, the correlation functions  $C_{Lu,Y}$  and  $C_{Y,Y}$  for heterogeneous neighboring distribution exhibit a substantial difference of an opposite sign for the distances of up to  $2r_{min} = 6.8 \text{ \AA}$  (Fig. 2.2(b)).

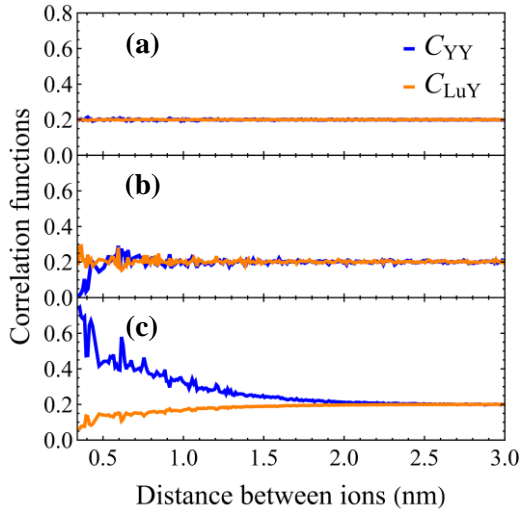


**Fig. 2.2.** Dependence of the correlation function on the distance between two ions for uniform (a), heterogeneous neighboring (b), and clustered (c) cation distribution [A1]. The parameters correspond to those used in Fig. 2.1.

### 2.3. Pseudopotential-based model of fluctuating crystal potential

To reveal the effect of compositional disorder in ternary crystalline ionic compound  $A_xB_{1-x}C$  on the crystal potential, energy characteristics, such as the density of states, the band structure, and the effective potential, of binary components should be analyzed. In the current chapter, general features of disorder-induced potential fluctuations were studied using the LYSO solid solution.

Lutetium and yttrium cations are predominantly involved in the formation of the conduction band in LSO and YSO crystals. Thus, the impact of the compositional disorder in Lu/Y cationic subsystem of  $Lu_{2(1-x)}Y_{2x}SiO_5$  solid solution on the electron states in the conduction band was studied. However, the proposed description can also be applied to the problem of the impact of the compositional disorder in an anionic subsystem of a compound scintillator on the states in the valence band.

The DFT approach exploiting the Schrodinger equation for the effective potential of core and valence electrons with the periodic boundary conditions is usually exploited to describe single electron states in a unit cell of the crystal. The modulation of the effective potential breaking its periodicity in LYSO crystal is mainly caused by the difference between the lutetium and yttrium ionic potentials. Such modulation of the effective potential should

cause scattering of single electron states in LYSO crystal. In fact, the fluctuations of the effective potential in a compound scintillator can be approximated by those in a big supercell with the periodic boundary conditions, and calculations can be performed using the DFT method. However, such calculations are difficult and time-consuming. On the other hand, the pseudopotential method can be used to obtain the effective potential fluctuations caused by the compositional disorder in the quasiclassical approximation [123]. To make some conclusions on the form of the pseudopotential in LYSO scintillator, the band structures and the effective potentials of LSO and YSO should be compared. In particular, a difference in the conduction bands of LSO and YSO should be discussed.

Figure 2.3 presents the band structures of YSO and LSO single crystals obtained using the Quantum Espresso package [124]. The Brillouin zone size in the  $\Gamma$ -Y direction is equal to  $4.6 \text{ nm}^{-1}$  for YSO and  $4.7 \text{ nm}^{-1}$  for LSO. That corresponds to  $\frac{\pi}{2r_{min}} = 4.62 \text{ nm}^{-1}$ .

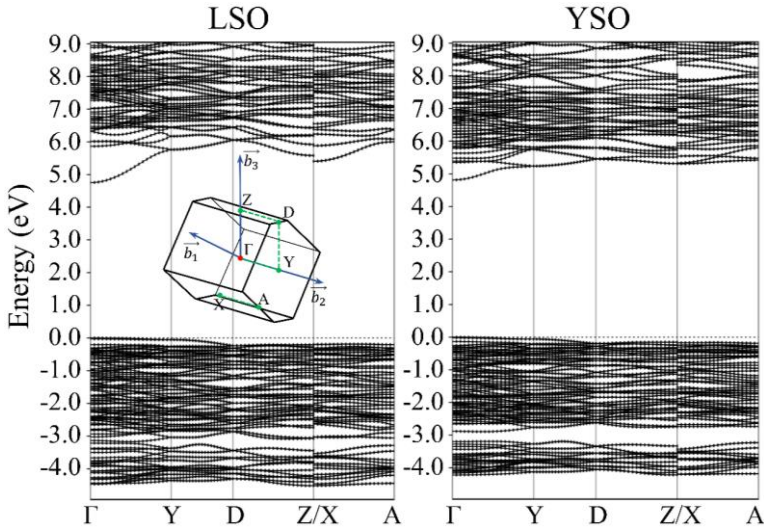


**Fig. 2.3.** Band structures of LSO (left) and YSO (right) crystals obtained using the Quantum Espresso package [A1]. The  $k$ -path in the Brillouin zone is shown in the inset. The valence band maximum is taken as energy zero.

As evident in Fig. 2.3, the main difference between the conduction bands of LSO and YSO crystals is the shift of higher energy branches of LSO crystal by  $\sim 600 \text{ meV}$  compared to those in YSO crystal. The density of states spectrum presented in Fig. 2.4 clearly shows the shift of higher energy branches. The obtained band gaps of LSO and YSO are equal to  $4.75 \text{ eV}$  and

4.83 eV, respectively. Note that the local-density approximation for the exchange-correlation functional and the basis of plane wave functions were used for the DFT calculations in this work. The value of the band gap is usually underestimated if the local-density approximation is exploited. Meanwhile, the calculations exploiting more accurate HSE hybrid functional [125] predicts 6.31 eV and 6.39 eV for the band gaps for LSO and YSO crystals, as reported in Ref. [126]. However, the experimentally observed band gaps in LSO and YSO crystals are equal to 7.266 eV and 7.376 eV, respectively [121], [122]. All these results predict a similar difference in the band gaps of LSO and YSO crystals,  $\Delta E_g$ , which is quite small. In the current study, the experimentally observed value of  $\Delta E_g = 110$  meV and the band gaps  $E_g^{LSO} = 7.266$  eV and  $E_g^{YSO} = 7.376$  eV for LSO and YSO binary crystals were used. The local-density approximation is sufficient for further analysis of the energy structure of LSO and YSO crystals.

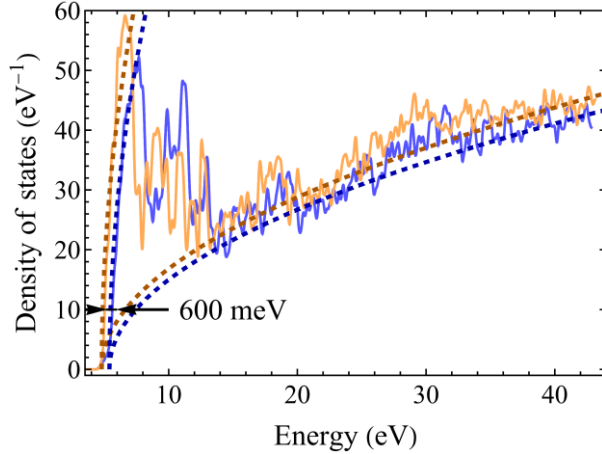


**Fig. 2.4.** Dependence of the density of states on the electron energy for LSO (blue line) and YSO (orange line) obtained using the Quantum Espresso package (solid lines) and in nearly free electron approximation (dashed lines) [A1]. The valence band maximum was taken as energy zero. The shift caused by higher energy branches is indicated, the difference in the band gap is too small to be seen on this scale.

Analyzing the obtained density of states, the electron effective mass in the vicinity of the  $\Gamma$  point was estimated to be 0.6 and 0.5 of the free electron mass,  $m_e$ , for YSO and LSO single crystals, respectively. The structure of energy levels has quasiatomic character in the intermediate range from 5.6 to 12.0 eV for LSO and from 5.1 to 12.0 eV for YSO. In the range from 5.6 to

7.8 eV for LSO and from 5.1 to 6.7 eV for YSO, the effective mass increases up to  $3.4m_e$  for both crystals. After that, in the range from 7.8 eV for LSO and 6.7 for YSO to 12.0 eV for both crystals, the effective mass decreases down to  $m_e$ . Finally, the electron effective mass remains equal to  $m_e$  at energies larger than 12 eV. Thus, the density of states can be well described in nearly free electron approximation with effective mass equal to  $m_e$  for this semi-infinite range (see dashed lines in Fig. 2.4).

The strong shift of high-energy branches down by  $\sim 600$  meV in the conduction band of YSO can be caused by the impact of a high-frequency negative term of the effective potential on single electron states in the conduction band. This high-frequency term must be spatially localized, i.e., has a size much smaller than the lattice constant. Figure 2.5 presents the effective potentials in LSO and YSO crystals on the same plane. The major difference is observed in yttrium and lutetium core areas.

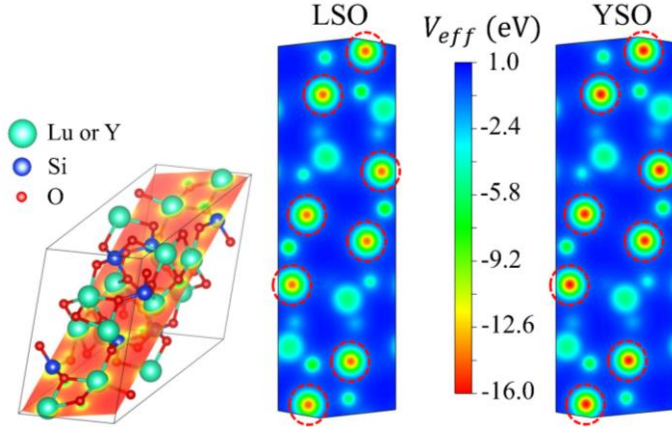


**Fig. 2.5.** Distribution of effective potentials in LSO and YSO on the same plane (shown on the left panel) obtained using the Quantum Espresso package [A1].

The core area size was obtained to be  $1.8 \text{ \AA}$ . The difference in the effective potentials in the centers of the core areas of lutetium and yttrium cations was estimated to be  $-1.5$  eV. Thus, a drop in the effective potential of the Lu/Y core areas when lutetium ions are replaced by yttrium ions apparently leads to the shift of 600 meV between higher energy branches in YSO and LSO crystals (see Fig. 2.4). Meanwhile, the band gap of LSO single crystal is 110 meV smaller than that of YSO crystal. Thus, there is a low-frequency positive term of the effective potential which predominantly affects electron states on the first branch in the conduction band leading to its shift higher on the energy

axis when lutetium ions are replaced by yttrium ions. In the quasiparticle approximation, the effect of such low- and high-frequency terms of the effective potential can be reflected in a positive and negative low-frequency pseudopotential with the amplitude proportional to 110 meV and 600 meV applying to electron states on first and higher branches in the conduction band, respectively.

Thus, the total pseudopotential acting on certain electron states in the conduction band of  $A_xB_{1-x}C$  compound in the quasiclassical approximation under the assumption that the contributions of each ion are additive can be defined as

$$u(\vec{r}) = \sum_{\vec{R}} p_{\vec{R}} u_{lf}(\vec{r} - \vec{R}), \quad (2.5)$$

where  $u_{lf}(\vec{r})$  is the low-frequency pseudopotential, and  $p_{\vec{R}}$  is the matrix of nodes occupied by A ions.

Considering the local character of interaction between ions in a multicomponent crystalline compound, the low-frequency pseudopotential  $u_{lf}(\vec{r})$  can be described using the spline  $s(x)$  proposed in Ref. [13]:

$$u_{lf}(\vec{r}) = \frac{\Delta E}{n} \frac{4V_0}{\pi(\kappa a)^3} s\left(\frac{|\vec{r}|}{\kappa a}\right), \quad (2.6.1)$$

$$s(x) = \begin{cases} 0, & |x| > 1 \\ 2(1+x)^2, & -1 \leq x < -0.5 \\ 1-2x^2, & -0.5 \leq x < 0.5 \\ 2(1-x)^2, & 0.5 \leq x \leq 1 \end{cases}. \quad (2.6.2)$$

Here,  $\Delta E$  is the band offset,  $n$  is the number of A/B nodes in the unit cell,  $\kappa$  is the scale factor,  $a \approx xa_{AC} + (1-x)a_{BC}$  is the average lattice constant,  $a_{AC}$  and  $a_{BC}$  are the lattice constants of AC and BC crystals, respectively,  $V_0 \approx xV_{0,AC} + (1-x)V_{0,BC}$  is the average volume of the unit cell of  $A_xB_{1-x}C$  compound scintillator,  $V_{0,AC}$  and  $V_{0,BC}$  are the volumes of the unit cells of AC and BC binary components, respectively.

#### 2.4. Simulation of the pseudopotential for the conduction band in LYSO scintillator

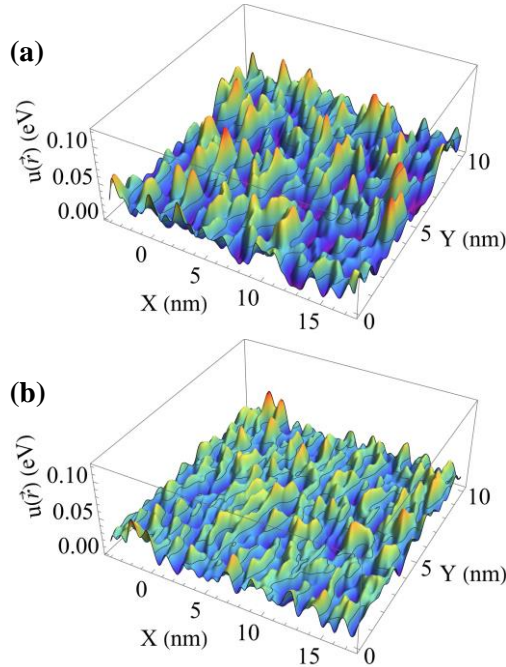
The parameters of LSO and YSO unit cells are listed in Table 2.1. The band offset  $\Delta E$  is equal to 110 and -600 meV for electron states on the first and higher energy branches in LYSO solid solution, respectively, The scale

factor  $\kappa$  was set as 0.5 taking into account two conditions: the total pseudopotential  $u(\vec{r})$  at  $x = 1$  should tend to a constant value at any point of the supercell, whereas the low-frequency pseudopotential  $u_{lf}(\vec{r})$  should be sufficiently local, i.e. the value of  $\kappa a$  should be close to  $r_{min}$ .

**Table 2.1.** Parameters of LSO and YSO unit cells [121], [122].

	LSO	YSO
$a$ (Å)	14.283	14.564
$V_0$ (Å <sup>3</sup> )	831.07	890.69
$n$	16	

Figure 2.6 shows 2D cross sections of the spatial distribution of the total pseudopotential for three types of cation distribution in LYSO supercell at the band offset of 110 meV (for electron states on the first branch). The fluctuation amplitude of a clustered crystal is quite large in comparison with those obtained for uniform and heterogeneous neighboring types. The characteristic size of fluctuations for the clustering case corresponds to  $\sim 8$  inter-cation distances, i.e.,  $\sim 30$  Å. This value is consistent with the characteristic attenuation length of the correlation function  $C_{YY}$  (see Fig. 2.2).



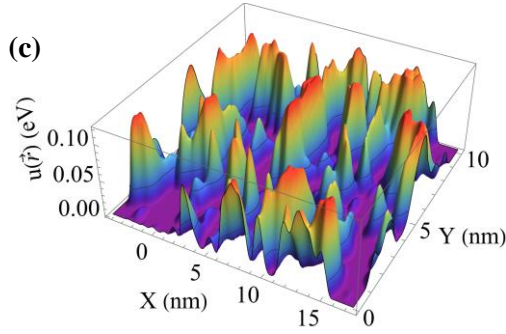


**Fig. 2.6.** Spatial distribution of the total pseudopotential  $u(\vec{r})$  for uniform (a), heterogeneous neighboring (b), and clustered (c) cation distribution in a  $\text{Lu}_{1.6}\text{Y}_{0.4}\text{SiO}_5$  supercell [A1]. The parameters correspond to those used in Fig. 2.1.

## 2.5. Electron(hole)-phonon scattering in the virtual crystal approximation

Fluctuations of the effective potential in  $\text{A}_x\text{B}_{1-x}\text{C}$  compound impact on the migration of charge carriers resulting in their scattering. However, carrier scattering due to phonon emission and absorption is the main scattering process at the carrier energy below the inelastic multiplication threshold. Therefore, the elastic scattering induced by the compositional disorder should be discussed along with the carrier scattering due to phonon emission and absorption. In ionic crystals, non-equilibrium electrons and holes mainly interact with longitudinal optical and acoustical phonons. Since free carrier transport is considered, the electron(hole)-phonon scattering can be satisfactorily described in the virtual crystal approximation.

The quasiclassical expressions of the electron(hole)-phonon scattering rates  $\tau_{LO,abs}^{-1,em}$  and  $\tau_{LA,e,abs}^{-1,em}$  due to LO and LA phonon emission and absorption in a regular crystal can be used to simulate such processes in  $\text{A}_x\text{B}_{1-x}\text{C}$  compound in the VC approximation [92]. In fact, the density functional theory can provide more accurate results describing the phonon relaxation in both regular crystal and supercell of a crystalline compound [11], [91], [127]. However, these calculations are complex and time-consuming. The quasiclassical approach with a parabolic band approximation is sufficient in a wide range of systems. Since the elastic scattering of non-equilibrium carriers on fluctuating pseudopotential was considered in the current work, the transport scattering rates  $\tau_{LO,tr,abs}^{-1,em}$  and  $\tau_{LA,tr,abs}^{-1,em}$  reflecting the scale of



electron momentum relaxation should be used. The expressions for  $\tau_{LO,tr,abs}^{-1}$  and  $\tau_{LA,tr,abs}^{-1}$  have the following forms:

$$\tau_{LO,tr,abs}^{-1}(E_k^{vc}) = \frac{e^2 \sqrt{m_{vc}^*} \Omega_{LO,vc}}{4\sqrt{2}\pi\epsilon_0 \hbar \tilde{\epsilon}_{s,vc}} \frac{1}{\sqrt{E_k^{vc}}} \left( n(\hbar\Omega_{LO,vc}) + \frac{1}{2} \pm \frac{1}{2} \right) \times \begin{cases} \theta(E_k^{vc} - \hbar\Omega_{LO,vc}), & \text{if LO em} \\ \theta(E_k^{vc}), & \text{if LO abs} \end{cases}, \quad (2.7.1)$$

$$\tau_{LA,tr,abs}^{-1}(E_k^{vc}) = \frac{\sqrt{m_{vc}^*} \sigma_{d,vc}^2}{8\sqrt{2}\pi \hbar c_{L,vc} \rho_{vc}} \frac{1}{\sqrt{E_k^{vc}}} \times \int_0^{2\left(\frac{\sqrt{2m_{vc}^* E_k^{vc} \mp c_{L,vc} m_{vc}^*}}{\hbar}\right)} \left( n(\hbar q c_{L,vc}) + \frac{1}{2} \pm \frac{1}{2} \right) q^2 \left( 1 - \frac{\hbar^2 q^2}{8m_{vc}^* E_k^{vc}} \right) dq \times \begin{cases} \theta\left(E_k^{vc} - \frac{m_{vc}^* c_{L,vc}^2}{2}\right), & \text{if LA em} \\ \theta(E_k^{vc}), & \text{if LA abs} \end{cases}, \quad (2.7.2)$$

with

$$n(\hbar\Omega) = \frac{1}{\frac{\hbar\Omega}{e^{k_B T}} - 1}. \quad (2.7.3)$$

Here,  $E_k^{vc}$  is the electron(hole) kinetic energy,  $m_{vc}^*$  is the electron(hole) effective mass,  $\epsilon_0$  is the vacuum permittivity,  $e$  is the electron charge,  $k_B$  is the Boltzmann constant,  $T$  is the temperature,  $\hbar$  is the reduced Planck constant,  $\theta(x)$  is the Heaviside step function,  $\Omega_{LO,vc}$  is the longitudinal optical phonon frequency,  $\tilde{\epsilon}_{s,vc}$  is the ionic part of the dielectric permittivity,  $\rho_{vc}$  is the crystal density,  $c_{L,vc}$  is the longitudinal sound velocity,  $\sigma_{d,vc}$  is the acoustic deformation potential. All these parameters relate to the virtual crystal.

The expression for the energy relaxation rate  $\tau_{LO,abs}^{-1}$  differs from (2.7.1)

by the logarithmic term  $\ln\left(\frac{\sqrt{E_k^{vc} + \sqrt{E_k^{vc} \mp \hbar\Omega_{LO,vc}}}}{\sqrt{E_k^{vc} - \sqrt{E_k^{vc} \mp \hbar\Omega_{LO,vc}}}}\right)$ , whereas the expression for

the energy relaxation rate  $\tau_{LA,abs}^{-1}$  doesn't contain the term  $\left(1 - \frac{q^2}{8m_{vc}^* E_k^{vc}}\right)$  in the integral (2.7.2). Meanwhile, the total transport electron(hole)-phonon scattering rate  $\tau_{e/h-ph,tr}^{-1}$  might be obtained as a sum of  $\tau_{LO,tr,abs}^{-1}$  and  $\tau_{LA,tr,abs}^{-1}$ . Although the expressions (2.7) are valid for the states on a single parabolic branch, i.e. states with the wavevector in the vicinity of the  $\Gamma$  point, they provide a quite accurate estimation of electron(hole)-phonon scattering

rate for high-energy carriers taking into account changes in the effective mass. Herewith, the upper integral limit in the expression (2.7.2) should be restricted by  $q_{max} \simeq \frac{\pi}{\sqrt[3]{V_0}}$  at the phonon wavevector module  $q$  exceeding the Brillouin zone size.

$A_xB_{1-x}C$  parameters in the VC approximation can be obtained by interpolation as follows:

$$\frac{1}{m_{vc}^*} = \frac{x}{m_{AC}^*} + \frac{1-x}{m_{BC}^*}, \quad (2.8.1)$$

$$\Omega_{LO,vc} = x\Omega_{LO,AC} + (1-x)\Omega_{LO,BC}, \quad (2.8.2)$$

$$\frac{\Omega_{LO,vc}}{\tilde{\epsilon}_{s,vc}} = x\Omega_{LO,AC} \left( \frac{1}{\epsilon_{\infty,AC}} - \frac{1}{\epsilon_{st,AC}} \right) + (1-x)\Omega_{LO,BC} \left( \frac{1}{\epsilon_{\infty,BC}} - \frac{1}{\epsilon_{st,BC}} \right), \quad (2.8.3)$$

$$c_{L,vc} = xc_{L,AC} + (1-x)c_{L,BC}, \quad (2.8.4)$$

$$\rho_{vc} = \frac{x\rho_{AC}V_{0,AC} + (1-x)\rho_{BC}V_{0,BC}}{xV_{0,AC} + (1-x)V_{0,BC}}, \quad (2.8.5)$$

$$\frac{\sigma_{d,vc}^2}{c_{L,vc}} = x \frac{\sigma_{d,AC}^2}{c_{L,AC}} + (1-x) \frac{\sigma_{d,BC}^2}{c_{L,BC}}, \quad (2.8.6)$$

where  $\epsilon_{\infty,AC/BC}$  and  $\epsilon_{st,AC/BC}$  are the high-frequency and static dielectric permittivity of AC and BC single crystals, respectively.

Note that the interpolation expressions (2.8.3) and (2.8.6) were obtained under the assumption that the energy loss function for  $A_xB_{1-x}C$  compound in the virtual crystal approximation can be evaluated as  $Im\left(-\frac{1}{\epsilon_{vc}(\omega)}\right) \approx x Im\left(-\frac{1}{\epsilon_{AC}(\omega)}\right) + (1-x) Im\left(-\frac{1}{\epsilon_{BC}(\omega)}\right)$ .

The LSO and YSO parameters exploited for calculating the electron-phonon scattering rates are listed in Table 2.2.

**Table 2.2.** Parameters of LSO and YSO single crystals.

	LSO	YSO
$m_{e,vc}^*(m_e)$	0.5	0.6
$\hbar\Omega_{LO}$ (meV)	40.0 [5]	40.0 [5]
$\epsilon_{\infty}$	10.4 [5]	10.4 [5]
$\epsilon_{st}$	3.2 [5]	3.2 [5]
$c_L$ ( $10^5$ cm/s)	3.33 [128]	3.98 [128]
$\rho$ (g/cm <sup>-3</sup> )	7.59 [121]	4.42 [122]
$\sigma_d$ (eV)	9.1	9.3

The deformation potential in LSO and YSO crystals, which is the measure of the change of the electron energy as a result of changing volume of the unit cell, i.e.,  $\Delta E_e(\vec{k}) = -\sigma_d \frac{\Delta V_{cell}}{V_{cell}}$ , was obtained using the Quantum Espresso package.

## 2.6. Elastic scattering of non-equilibrium carriers on pseudopotential fluctuations in the Born approximation

The scattering of non-equilibrium carriers on the effective potential fluctuations can be described as the scattering of single particle states of the virtual crystal  $|\varphi_{n,\vec{k}}^{vc}\rangle$ :

$$\hat{H}_{vc} = x\hat{H}_{AC} + (1-x)\hat{H}_{BC}, \quad (2.9.1)$$

$$\hat{H}_{vc} |\varphi_{n,\vec{k}}^{vc}\rangle = \varepsilon_n^{vc}(\vec{k}) |\varphi_{n,\vec{k}}^{vc}\rangle, \quad (2.9.2)$$

where  $\hat{H}_{vc}$  is the virtual crystal Hamiltonian,  $\hat{H}_{AC}$  and  $\hat{H}_{BC}$  are the Hamiltonians for AC and BC single crystals in the single particle approximation,  $\varepsilon_n^{vc}(\vec{k})$  are the eigenvalues of the virtual crystal Hamiltonian  $\hat{H}_{vc}$ .

The total Hamiltonian  $\hat{H}$  of  $A_xB_{1-x}C$  crystalline compound can be written as

$$\hat{H} = \hat{H}_{vc} + \hat{w}, \quad (2.10.1)$$

$$w(\vec{r}) = \sum_{\vec{R}} (p_{\vec{R}} - x) u_{lf}(\vec{r} - \vec{R}), \quad (2.10.2)$$

where  $\hat{w}$  is the perturbation operator reflecting the effect of disorder-induced potential fluctuations, whereas  $w(\vec{r})$  is its position representation in the quasiclassical approximation relative to the pseudopotential  $\langle u(\vec{r}) \rangle$  averaged over a fluctuation ensemble.

The description task of the alloy scattering of electrons or holes in the quasiclassical approximation can be divided into two asymptotical cases: i) scattering at low carrier energies when the unreduced wave vector is located in the first Brillouin zone and ii) scattering at high carrier energies, in particular, for electrons assuming the nearly free electron approximation.

In the quasiclassical approximation, the transport alloy scattering rate for high-energy carriers can be evaluated using the transport cross section in the Born approximation:

$$\sigma_{tr} \left( E_k^{vc}(\vec{K}) \right) = \left( \frac{m_{vc}^*}{2\pi\hbar^2} \right)^2 \int |\int w(\vec{r}) e^{i\vec{q}\vec{r}} d\vec{r}|^2 (1 - \cos(\theta)) d\Omega_{\vec{K}'}. \quad (2.11)$$

Here,  $\vec{q} = \vec{K} - \vec{K}'$  is the scattering vector,  $\vec{K}$  and  $\vec{K}'$  are unreduced wave vectors of incoming and outgoing waves, respectively,  $\theta$  is the angle between  $\vec{K}$  and  $\vec{K}'$  vectors. Since the elastic carrier scattering is considered,  $\vec{K}'$  vector belongs the set of vectors of the isoenergetic surface  $E_k^{vc}(\vec{K}') = E_k^{vc}(\vec{K})$ .

Finally, the transport cross section can be written as

$$\sigma_{tr} \left( E_k^{vc}(\vec{K}) \right) = \left( \frac{m_{vc}^*}{2\pi\hbar^2} \right)^2 V^2 \int |S(\vec{q})|^2 u_{lf}(\vec{q})^2 (1 - \cos(\theta)) d\Omega_{\vec{K}'}, \quad (2.12.1)$$

$$u_{lf}(\vec{q}) = \Delta E \frac{128 \sin^2\left(\frac{\kappa a |\vec{q}|}{4}\right) \left( 6 \sin\left(\frac{\kappa a |\vec{q}|}{2}\right) - \kappa a |\vec{q}| - 2\kappa a |\vec{q}| \cos\left(\frac{\kappa a |\vec{q}|}{2}\right) \right)}{(\kappa a |\vec{q}|)^5}, \quad (2.12.1)$$

$$S(\vec{q}) = \frac{1}{N} \sum_{\vec{R}} (p_{\vec{R}} - x) e^{i\vec{q}\vec{R}}. \quad (2.12.3)$$

Here,  $u_{lf}(\vec{q})$  is the Fourier component of low-frequency pseudopotential,  $S(\vec{q})$  is the structural factor,  $N = \frac{V}{V_0}$  is the number of primitive cells in the supercell. In the parabolic band approximation, the relationship between the carrier kinetic energy  $E_k^{vc}(\vec{K})$  and the unreduced wave vector  $\vec{K}$  can be written as

$$E_k^{vc}(\vec{K}) = \frac{\hbar^2 \vec{K}^2}{2m_{vc}^*}. \quad (2.13)$$

The zero for carrier kinetic energy is set at the band edge (conduction or valence) of the virtual crystal.

Finally, the transport alloy scattering rate can be expressed as

$$\tau_{alloy,tr}^{-1} \left( E_k^{vc}(\vec{K}) \right) = \frac{\sigma_{tr} \left( E_k^{vc}(\vec{K}) \right)}{v} \sqrt{\frac{2E_k^{vc}(\vec{K})}{m_e}}. \quad (2.14)$$

## 2.7. Elastic scattering of non-equilibrium carriers on pseudopotential fluctuations in the coherent potential approximation

The scattering of non-equilibrium carriers with low kinetic energy on the effective potential fluctuations can be described by using the CPA method [14] exploiting the average Green's function

$$\langle \hat{G} \rangle = \langle \hat{G}_0 + \hat{G}_0 \hat{W} \hat{G} \rangle. \quad (2.15)$$

Here,  $\hat{G}_0$  is the Green's function of the virtual crystal,  $\hat{G}$  is the full Green's function of the disordered system.

Since the average Green's function relates to the system with the effective potential averaged over a fluctuation ensemble, the matrix elements of the average Green's function in the basis of the virtual crystal states  $|\varphi_{n,\vec{k}}^{vc}\rangle$  are diagonal and can be written as

$$\langle \varphi_{n,\vec{k}}^{vc} | \langle \hat{G}(E) \rangle | \varphi_{n,\vec{k}}^{vc} \rangle = \frac{1}{E - \varepsilon_n^{vc}(\vec{k}) - \Sigma_{n,\vec{k}}(E)}. \quad (2.16)$$

Here,  $\Sigma_{n,\vec{k}}(E)$  are the matrix elements of the self-energy operator  $\hat{\Sigma}$  in the basis of the virtual crystal states  $|\varphi_{n,\vec{k}}^{vc}\rangle$ . Herewith, the self-energy operator  $\hat{\Sigma}$  can be expressed using the full Green's function  $\hat{G}$  as

$$\langle \hat{G} \rangle = (\hat{G}_0^{-1} - \hat{\Sigma})^{-1} \Rightarrow \hat{\Sigma} = \langle \hat{W} \hat{G} \hat{W} \rangle (1 + \hat{G}_0 \langle \hat{W} \hat{G} \hat{W} \rangle)^{-1}. \quad (2.17)$$

The expression (2.17) can be simplified by replacing the full Green's function  $\hat{G}$  with the average Green's function  $\langle \hat{G} \rangle$  and then decomposing the term  $(1 + \hat{G}_0 \langle \hat{W} \hat{G} \hat{W} \rangle)^{-1}$  into a series cutting it at the quadratic term:

$$\begin{aligned} \hat{\Sigma} &\approx \langle \hat{W} \langle \hat{G} \rangle \hat{W} \rangle (1 + \hat{G}_0 \langle \hat{W} \langle \hat{G} \rangle \hat{W} \rangle)^{-1} \approx \\ &\approx \langle \hat{W} \langle \hat{G} \rangle \hat{W} \rangle. \end{aligned} \quad (2.18)$$

As the result, the matrix elements of the self-energy operator can be calculated as

$$\Sigma_{n,\vec{k}}(E) \approx \frac{V}{(2\pi)^3} \sum_{n'} \int_B \frac{|\langle \varphi_{n',\vec{k}'}^{vc} | \widehat{W} | \varphi_{n,\vec{k}}^{vc} \rangle|^2}{E - \varepsilon_{n'}^{vc}(\vec{k}') - \Sigma_{n',\vec{k}'}(E)} d\vec{k}'. \quad (2.19)$$

Note that, unlike the alloy transport rate (2.14) in the Born approximation, the integral equation (2.19) allows avoiding the divergence at the  $\Gamma$  point.

Using the pseudopotential  $w(\vec{r})$  to approximate the fluctuating effective potential in the quasiclassical approximation and considering only the first branch in the band (conduction or valence) of the virtual crystal, the equation (2.19) can be rewritten as

$$\Sigma_K(E) = \frac{V}{(2\pi)^3} \int_0^{K_{max}} \frac{K'^2 W(K, K')}{E - \frac{\hbar^2 K'^2}{2m_{vc}^*} - \Sigma_{K'}(E)} dK', \quad (2.20.1)$$

with

$$W(K, K') = \int_0^{2\pi} \int_0^\pi |w(\vec{K} - \vec{K}')|^2 d\Omega_{\vec{K}'}, \quad (2.20.2)$$

$$w(\vec{q}) = S(\vec{q}) u_{lf}(\vec{q}), \quad (2.20.3)$$

where  $w(\vec{q})$  is the Fourier component of the pseudopotential  $w(\vec{r})$ .

In the CPA, the carrier kinetic energy  $E_k^{CPA}$  with a certain wave vector  $\vec{K}$  is complex and for a single parabolic band satisfies the following equation:

$$E_k^{CPA}(K) = \frac{E_k^{vc}(K)}{\widehat{\frac{\hbar^2 K^2}{2m_{vc}^*}}} + \Sigma_K(E_k^{CPA}(K)). \quad (2.21)$$

The imaginary part of  $E_k^{CPA}$  reflects the energy uncertainty of a state with the wave vector  $\vec{K}$  and can be used to calculate the alloy scattering rate for energy relaxation as

$$\tau_{alloy}^{-1}(E_k^{CPA}(K)) = \frac{2 |\text{Im}(\Sigma_K(E_k^{CPA}(K)))|}{\hbar}. \quad (2.22)$$

This scattering rate is close to the momentum relaxation scattering rate at low energies. Note that unlike scattering at high energies, the alloy scattering at low energies has a diffusion character.

## 2.8. Calculation of the alloy scattering rate for electrons in LYSO scintillator

Figure 2.8 presents the transport alloy scattering rate in the Born approximation and the total transport rate of scattering due to the phonon emission and absorption as a function of the electron kinetic energy. Since LSO and YSO parameters of electron-phonon scattering are similar, the total transport rate for scattering due to the phonon emission and absorption is presented in Fig. 2.8 only at yttrium content of 20%. Note that the free electron mass  $m_e$  was used as the effective electron mass in the expression (2.7) to calculate the total electron-phonon scattering rate for high-energy electrons, whereas the band offset  $\Delta E = 600$  meV in the expression (2.6) was used for electron states on higher branches.

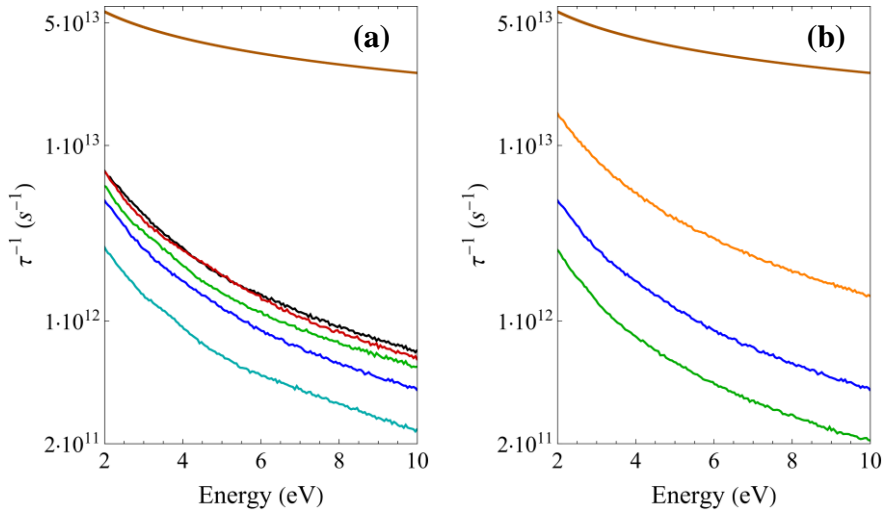


**Fig. 2.8.** Electron kinetic energy dependence of the total transport rate for scattering due to phonon emission and absorption in the VC approximation at yttrium content of 20% (brown curves in (a) and (b)) and the transport rate for alloy scattering in the Born approximation for the uniform cation distribution at yttrium content of 10% (cyan), 20% (blue), 30% (green), 40% (red) and 50% (black) (a); and at yttrium content of 20% for three types of cation distribution: uniform (blue), heterogeneous neighboring (green), and clustered (orange) (b). The parameters correspond to those used in Fig. 2.1.

The magnitude of the transport alloy scattering rate at high electron energies is smaller than the total transport rate of scattering due to phonon emission and absorption by at least one order of magnitude for the uniform

cation distribution. For the clustered distribution, the transport rate for alloy scattering has the largest amplitude tending to reach the electron-phonon scattering rate with decreasing kinetic energy. However, the formation of a clustered cation distribution in LYSO solid solution is unlikely. Therefore, the effect of the alloy scattering of high-energy electrons in LYSO crystal is negligible.

It is worth noting that the quasiclassical approximation doesn't work well for the quasiatomic energy levels from 0.3 to 7.2 eV above the edge of the conduction band (see Fig. 2.4). Here, the DFT-based method has to be applied to the LYSO supercell with periodic boundary conditions to calculate the alloy scattering rate.

Figure 2.9 shows the imaginary part of the matrix elements of the self-energy operator  $\Sigma_K(E)$  on the mass surface  $E_k^{CPA}(K)$  in the parabolic band approximation for three types of cation distributions in the  $\text{Lu}_{1.6}\text{Y}_{0.4}\text{SiO}_5$  solid solution.

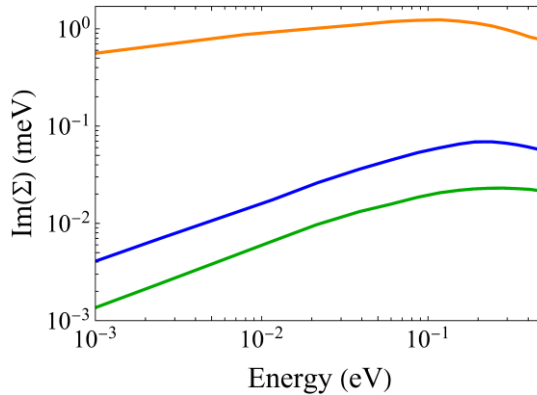


**Fig. 2.9.** The imaginary part of matrix elements of self-energy operator on the mass surface in the parabolic band approximation for three types of cation distribution: uniform (blue), heterogeneous neighboring (orange), and clustered (green) in  $\text{Lu}_{1.6}\text{Y}_{0.4}\text{SiO}_5$  solid solution [A1].

The maximal magnitude of the imaginary part of matrix elements of the self-energy operator is  $\sim 0.05$  meV for the uniform distribution and  $\sim 1$  meV for the clustered distribution in the  $\text{Lu}_{1.6}\text{Y}_{0.4}\text{SiO}_5$  solid solution. These values result in long alloy scattering times evaluated to be  $\frac{\hbar}{2 \cdot 0.05 \text{ meV}} \approx 6.58$  ps and  $\frac{\hbar}{2 \cdot 1 \text{ meV}} \approx 0.33$  ps for the uniform and clustered distributions, respectively. Such scattering times are larger than the typical time of scattering due to phonon emission and absorption ( $\sim 10$  fs). Thus, a weak scattering of low-



energy electrons on the pseudopotential fluctuations in LYSO solid solution might be expected.

Figure 2.10 presents the alloy scattering rate in the CPA and the total transport rate of scattering due to phonon emission and absorption as a function of the electron kinetic energy. Note that the total transport rate of scattering due to the phonon emission and absorption is presented in Fig. 2.10 only at yttrium content of 20%.

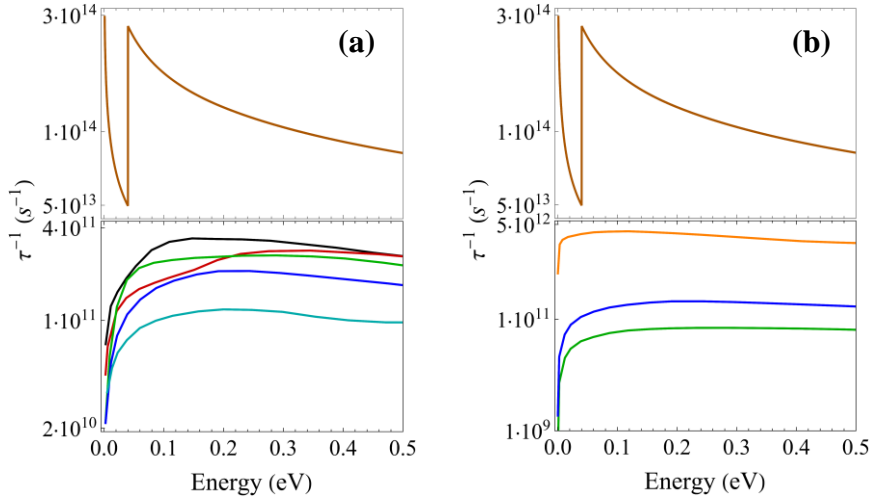


**Fig. 2.10.** Electron kinetic energy dependence of the total transport rate of scattering due to phonon emission and absorption in the VC approximation at yttrium content of 20% (brown curves in (a) and (b)) and the alloy scattering rate in the CPA for the uniform cation distribution at yttrium content of 10% (cyan), 20% (blue), 30% (green), 40% (red) and 50% (black) (a); and at yttrium content of 20% for three types of cation distribution: uniform (blue), heterogeneous neighboring (green), and clustered (orange) (b). The parameters correspond to those used in Fig. 2.1.

The obtained values of the alloy scattering rate for low electron energies are still significantly smaller than the total transport rate of electron scattering due to phonon emission and absorption even for the clustered cation distribution. Thus, our calculations revealed that the compositional disorder in LYSO solid solution has a weak effect on the migration of free non-equilibrium electrons.

## 2.9. Density of states in a crystalline compound

The disorder-induced pseudopotential fluctuations can also lead to the formation of spatially localized states of non-equilibrium carriers, i.e. states with zero mobility resulting in the formation of a tail in the density of states. Although the strict separation of states into free and localized cannot be defined, states with energy below a certain value, in particular, zero kinetic energy in a virtual crystal, can be considered as predominantly localized. The energy of the localized states is negative.

The density of states can be calculated by exploiting the matrix elements of the self-energy operator  $\Sigma_{n,\vec{k}}(E)$  obtained by using the CPA:

$$g(E) = -\frac{2}{\pi N} \text{Im} \left( \sum_{n,\vec{k}} \frac{1}{E - \varepsilon_n^{vc}(\vec{k}) - \Sigma_{n,\vec{k}}(E)} \right). \quad (2.23)$$

It is worth noting that this method provides underestimated values of the density of states at energies lower than the mobility threshold.

In addition, the upper limit of the density of states at negative energies can be evaluated using the quasiclassical approach proposed in Ref. [13]. In this case, the expression for the density of states can be written as

$$g(E) = 2 \frac{(2m_{vc}^*)^{\frac{3}{2}}}{(2\pi)^2 \hbar^3} \frac{1}{N} \int_V \sqrt{E - w(\vec{r})} \theta(E - w(\vec{r})) d\vec{r}. \quad (2.24)$$

## 2.10. Calculation of the density of states in LYSO scintillator

Certain conclusions about the dynamics of thermalized electrons in LYSO solid solution can be made by analyzing the density of states. Figure 2.11 presents the energy dependence of the density of states for non-equilibrium electrons in  $\text{Lu}_{1.6}\text{Y}_{0.4}\text{SiO}_5$  solid solution calculated using the quasiclassical approach and the CPA method for three types of cation distribution.

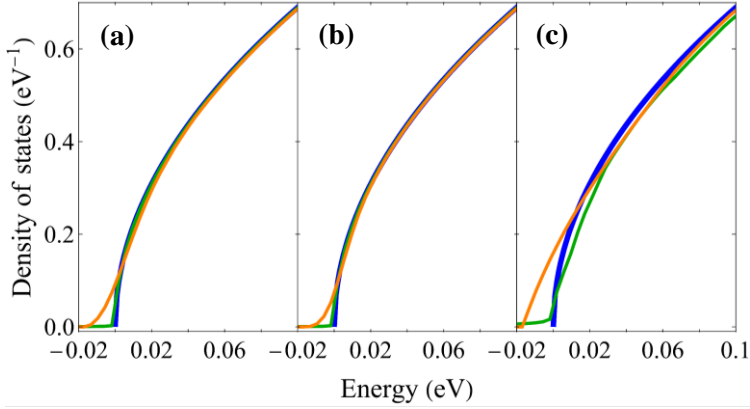


**Fig. 2.11.** Electron energy dependence of the density of states in  $\text{Lu}_{1.6}\text{Y}_{0.4}\text{SiO}_5$  solid solution calculated using quasiclassical approach (orange) and CPA method (green) for three types of cation distribution: uniform (a), heterogeneous neighboring (b), and clustered (c) [A1]. The density of states of the virtual crystal is shown by a blue line. The parameters correspond to those used in Fig. 2.1. The bottom of the conduction band of the virtual crystal was taken as energy zero.

The CPA method and the quasiclassical approach allow calculating the lower and upper limits, respectively, of the density of states at negative energies. These results can be used to estimate the concentration of localized states in LYSO solid solution. Using the average result between the densities of states in these two limits, the concentration of localized states in  $\text{Lu}_{1.6}\text{Y}_{0.4}\text{SiO}_5$  crystal was evaluated to be  $3.7 \cdot 10^{17} \text{ cm}^{-3}$ , which is quite large. For instance, the concentration of non-equilibrium electrons in an ionization track produced by 100-keV electron in  $\text{Lu}_{1.6}\text{Y}_{0.4}\text{SiO}_5$  crystal is obtained to be  $1.1 \cdot 10^{16} \text{ cm}^{-3}$ , estimated as  $\frac{100 \text{ keV}}{2.4 (0.2 E_g^{YSO} + 0.8 E_g^{LSO})} \frac{1}{\pi r_{th}^2 \langle L \rangle}$ , where  $r_{th} \sim 100 \text{ nm}$  [5] is the average displacement of secondary electrons during inelastic processes and subsequent thermalization in LYSO crystal,  $\langle L \rangle$  is the average track length of an initial electron obtained to be  $16 \mu\text{m}$  using the GEANT4 package. Thus, the localization of the entire population of secondary electrons after the thermalization stage might be expected in LYSO:Ce scintillators. However, the depth of potential wells in LYSO solid solution with the uniform cation distribution is quite small. Thus, a localized electron can quickly leave the potential well due to the absorption of a LO or short-wavelength LA phonon. Consequently, these estimates show that the effect of compositional disorder on the migration of non-equilibrium electrons

with energy close to the mobility threshold in LYSO solid solution is also weak.

## 2.11. Conclusions

A theoretical description of the alloy scattering of free non-equilibrium carriers in multicomponent ionic scintillators with compositional disorder is developed. This description was applied on LYSO solid solution for calculating the alloy scattering rate of free non-equilibrium electrons. To perform the analysis of disorder-induced fluctuations of the crystal potential in LYSO system, the density of states, the energy structure, and the effective potential in binary LSO and YSO crystals were obtained using the Quantum Espresso package. The Lu and Y cation distributions in LYSO supercell were simulated using the thermodynamic model, which exploits three parameters as the probability amplitudes of the formation of pairs Y-Y, Lu-Lu, and Lu-Y at the minimum distance. Among the many variations of these parameters, three qualitatively different types of cation distributions, uniform, heterogeneous neighboring, and clustered, were considered. The uniform distribution is supposed to be the most likely type, however, all three types were considered. Using the obtained cation distributions, the alloy scattering rate of free non-equilibrium electrons is calculated in the low ( $0 < E_k < 0.3$  eV) and high ( $E_k > 7.2$  eV) energy asymptotical limits using the CPA and Born approximation, respectively. The obtained values of the alloy scattering rate in both limits are at least one order of magnitude smaller than the total transport rate of scattering due to phonon emission and absorption. Therefore, a weak effect of compositional disorder on the migration of free non-equilibrium electrons in LYSO scintillator was evidenced. In addition, the lower and upper limits of the density of localized states in  $\text{Lu}_{1.6}\text{Y}_{0.4}\text{SiO}_5$  solid solution were estimated using the CPA method and the quasiclassical approach, respectively. Using the obtained results, the concentration of localized states in  $\text{Lu}_{1.6}\text{Y}_{0.4}\text{SiO}_5$  solid solution was evaluated. This value is comparable to the density of secondary carriers expected in an ionization track. However, the depth of potential wells in LYSO solid solution is quite small and does not exceed the energy of LO or short-wavelength LA phonons. Thus, quick activation of localized electrons due to phonon absorption can be expected. Thus, a weak effect of compositional disorder on the migration of non-equilibrium electrons with energy close to the mobility threshold in LYSO solid solution is evidenced.

### 3. EFFECT OF COMPOSITIONAL DISORDER ON CARRIER DIFFUSION IN COMPOUND SEMICONDUCTORS

In Chapter 2, the process of carrier scattering due to phonon emission and absorption in a crystalline compound was considered under the virtual crystal approximation. Such approach is valid at carrier energies substantially exceeding the amplitude of disorder-induced pseudopotential fluctuations but provides low accuracy at the carrier energy close to the mobility threshold. Meanwhile, this method does not allow describing the localization mechanism of non-equilibrium carriers due to phonon emission in disorder-induced potential wells. In the current chapter, a modification of the electron(hole)-phonon scattering rate in the VC approximation by using the local landscape method was suggested. This technique was applied to AlGa<sub>x</sub>N semiconductor for calculating the heavy-hole diffusion coefficient. The simulation results were compared with the experimental results obtained by using the light-induced transient grating technique.

#### 3.1. Materials and experimental techniques

Twelve Al<sub>x</sub>Ga<sub>1-x</sub>N epilayers with the aluminum content  $x$  varying from 10% to 70% and one GaN layer as an aluminum-free reference layer were used in the experimental study. The materials were grown by the metalorganic chemical vapor deposition (MOCVD) technique. The aluminum content was evaluated from X-ray diffraction. Nine  $\sim 1$   $\mu\text{m}$ -thick epilayers with the aluminum content  $x \geq 0.48$  were grown on (0.6-8)  $\mu\text{m}$ -thick AlN buffers deposited on c-sapphire using the migration-enhanced MOCVD method, whereas other three 130-300 nm-thick epilayers were grown on identical c-plane GaN/sapphire templates with 4  $\mu\text{m}$ -thick GaN buffers. Note that all epilayers are considered strain-free because their thickness substantially exceeds the critical thickness [129].

The light-induced transient grating (LITG) technique was exploited to evaluate the ambipolar diffusion coefficient of non-equilibrium carriers in samples under this study. This technique exploits an Ekspla Nd:YAG laser to generate two coherent 25-ps pump pulses simultaneously intersecting at the angle  $\Theta$  on the sample. These two pulses create a transient pattern of photoexcited carriers spatially modulated with spacing  $\Lambda = \lambda_{\text{pump}} / 2\sin(\Theta/2)$  [130]. The repetition rate was equal to 10 Hz. The pulse excitation wavelength  $\lambda_{\text{pump}}$  of 266/213 nm was selected for band-to-band excitation of

the samples. The spatial modulation of the density of photoexcited carriers leads to the modulation of the refractive index forming a transient diffraction grating, which decays due to diffusion and recombination of carriers. The decay kinetics of such transient diffraction grating was monitored by a probe pulse with the wavelength  $\lambda_{\text{probe}} = 1064$  nm in the transparency region of the samples. The ambipolar diffusion coefficient  $D_a$  was obtained from the evaluation of the decay time  $\tau_G$  of the diffracted pulse at various grating spacings  $\Lambda$  and the effective recombination time  $\tau_r$  as  $D_a = \frac{\Lambda^2}{(2\pi)^2} \left( \frac{1}{\tau_G} - \frac{1}{\tau_r} \right)$ . The heavy-hole diffusion coefficient was estimated as  $D_{hh} = \frac{D_a}{2}$  taking into account that the diffusion coefficient of holes is substantially smaller than that of electrons, whereas the densities of nonequilibrium electrons and holes were equal in the samples under study [131].

### 3.2. Electron(hole)-phonon scattering in crystalline compound with strong compositional disorder

As discussed above, the VC approximation is not appropriate to describe the diffusion of carriers with energy close to the mobility threshold. The phonon relaxation process in a crystalline compound with strong compositional disorder can be quite accurately described by using the DFT method [11], [91]. However, these calculations are time-consuming. On the other hand, the local landscape method [74] can be exploited to modify the quasiclassical energy relaxation rates  $\tau_{LO,abs}^{-1,em}$  and  $\tau_{LA,abs}^{-1,em}$  of electron(hole) scattering due to LO and LA phonon emission and absorption in the VC approximation. The energy relaxation rates should be used to describe the carrier localization process as opposed to the momentum relaxation rates used in section 2.5. The expressions for  $\tau_{LO,abs}^{-1,em}$  and  $\tau_{LA,abs}^{-1,em}$  can be expressed as in (2.7) by taking into account the logarithmic and subintegral terms, respectively.

The electron(hole)-phonon scattering rates  $\tau_{ph,abs}^{-1,em,disorder}$  in a disordered crystal can be calculated by integrating  $\tau_{LO,abs}^{-1,em}$  and  $\tau_{LA,abs}^{-1,em}$  with the semiclassical confining potential  $E_0(\vec{r})$ , which is evaluated using the local landscape method.

The semiclassical confining potential  $E_0(\vec{r})$  affecting electron (hole) states on a certain branch in the conduction (valence) band of the virtual crystal can be obtained by solving the following equation:

$$\left(-\frac{\hbar^2}{2m_{vc}^*}\Delta - \tilde{u}(\vec{r})\right)v(\vec{r}) = 1, \quad (3.1.1)$$

$$\tilde{u}(\vec{r}) = u(\vec{r}) - \max(u(\vec{r})), \quad (3.1.2)$$

$$E_0(\vec{r}) \approx -\frac{1}{v(\vec{r})} + \max(u(\vec{r})), \quad (3.1.3)$$

with the periodic boundary conditions

$$v(\vec{r} + \vec{T}_i) = v(\vec{r}), \quad (3.1.4)$$

where  $v(\vec{r})$  is the local landscape and  $\vec{T}_i$  are the translation vectors of the supercell.

Here, the fluctuating effective potential in a compound supercell is considered in the quasiclassical approximation using the pseudopotential  $u(\vec{r})$ , which can be obtained as discussed in section 2.3.

As a result, the electron(hole)-phonon scattering rates  $\tau_{ph,abs}^{-1}$ , disorder in a crystalline compound with strong compositional disorder can be evaluated using the obtained confining potential  $E_0(\vec{r})$  and the electron(hole)-phonon scattering rates  $\tau_{LO,abs}^{-1}$ ,  $em$  and  $\tau_{LA,abs}^{-1}$ ,  $em$  in the VC approximation as

$$\tau_{ph,abs}^{-1}, \text{ disorder}(E) = \frac{1}{V} \int_V \tau_{ph,abs}^{-1}(E + \tilde{E}_0(\vec{r})) d^3r \quad (3.2.1)$$

with

$$\tilde{E}_0(\vec{r}) = E_0(\vec{r}) - \langle E_0 \rangle. \quad (3.2.2)$$

Note that positive values of energy  $E$  in expression (3.2.1) correspond to the states of free non-equilibrium electrons (holes) in a crystalline compound and represent the average kinetic energy, i.e., the kinetic energy in the virtual crystal, whereas its negative values correspond to the states of localized electrons (holes). The strict mobility threshold at zero energy was assumed under this approach. However, this assumption is conditional because there is also an intermediate energy region of partially localized states in the vicinity of zero energy.

The momentum loss spectra for phonon emission and absorption in an interaction event in the virtual crystal approximation are proportional to  $\frac{1}{q}$  in the range from  $q_{LO,abs,max}(E_k^{vc})$  to  $q_{LO,abs,min}(E_k^{vc})$  and to  $q^2 \cdot \left(n(\hbar qc_{L,vc}) + \frac{1}{2} \pm \frac{1}{2}\right)$  in the range from 0 to  $q_{LA,abs,max}(E_k^{vc})$  for LO and LA

phonon branches, respectively. The limits of the phonon wavevector module can be calculated as

$$q_{LO,abs,max}(E) = \frac{\sqrt{2m_{vc}^*}}{\hbar} (\sqrt{E} + \sqrt{E \mp \hbar\Omega_{LO,vc}}), \quad (3.3.1)$$

$$q_{LO,abs,min}(E) = \frac{\sqrt{2m_{vc}^*}}{\hbar} (\sqrt{E} - \sqrt{E \mp \hbar\Omega_{LO,vc}}), \quad (3.3.2)$$

$$q_{LA,abs,max}(E) = \frac{2\sqrt{2m_{vc}^*E \mp c_{L,vc}m_{vc}^*}}{\hbar}. \quad (3.3.3)$$

The phonon momentum loss spectra in a disordered crystalline compound can be obtained by integrating the results for the virtual crystal over the semiclassical confining potential  $E_0(\vec{r})$  obtained by using the local landscape method:

$$\begin{aligned} G_{LO,abs}(E, q) &\sim \\ &\sim \int_V d^3r \begin{cases} \frac{1}{q}, & \text{if } q_{LO,abs,max}(E + \tilde{E}_0(\vec{r})) \geq q \geq q_{LO,abs,min}(E + \tilde{E}_0(\vec{r})) \\ 0, & \text{otherwise} \end{cases} \times \\ &\quad \times \begin{cases} \theta(E + \tilde{E}_0(\vec{r}) - \hbar\Omega_{LO,vc}), & \text{for LO em} \\ \theta(E + \tilde{E}_0(\vec{r})), & \text{for LO abs} \end{cases}, \quad (3.4.1) \end{aligned}$$

$$\begin{aligned} G_{LA,abs}(E, q) &\sim \\ &\sim \int_V d^3r \begin{cases} q^2 \left( n(\hbar qc_{L,vc}) + \frac{1}{2} \pm \frac{1}{2} \right), & \text{if } q_{LA,abs,max}(E + \tilde{E}_0(\vec{r})) \geq q \geq 0 \\ 0, & \text{otherwise} \end{cases} \times \\ &\quad \times \begin{cases} \theta \left( E + \tilde{E}_0(\vec{r}) - \frac{m_{vc}^*c_{L,vc}^2}{2} \right), & \text{for LO em} \\ \theta(E + \tilde{E}_0(\vec{r})), & \text{for LO abs} \end{cases}. \quad (3.4.2) \end{aligned}$$

### 3.3. Simulation of pseudopotential for the valence band in AlGaN semiconductor

$\text{Al}_x\text{Ga}_{1-x}\text{N}$  is a compound semiconductor of two binary nitrides AlN and GaN. The binary GaN and AlN crystals have hexagonal lattices with space group  $C6_3mc$  and similar lattice constants:  $a_{\text{AlN}} = 3.13 \text{ \AA}$  and  $a_{\text{GaN}} = 3.22 \text{ \AA}$  [132], [133]. The difference between the band gaps of AlN and GaN is quite large:  $\Delta E_g = E_{g,\text{AlN}} - E_{g,\text{GaN}} = 2.7 \text{ eV}$ , where  $E_{g,\text{AlN}} = 6.2 \text{ eV}$  and  $E_{g,\text{GaN}} = 3.5 \text{ eV}$  [68]. Such large  $\Delta E_g$  should lead to a strong modulation of the crystal potential in  $\text{Al}_x\text{Ga}_{1-x}\text{N}$  semiconductor. Disorder-induced potential fluctuations in



$\text{Al}_x\text{Ga}_{1-x}\text{N}$  compound should strongly affect single-particle states of the virtual crystal leading to the formation of localized states as well as the strong alloy scattering of free non-equilibrium carriers. In this chapter, the effect of compositional disorder on states of  $hh$ -branch in the valence band of  $\text{Al}_x\text{Ga}_{1-x}\text{N}$  compound semiconductor was considered.

The empirical pseudopotential (2.5) can be used to describe the fluctuations of the effective potential in an  $\text{Al}_x\text{Ga}_{1-x}\text{N}$  supercell in the quasiclassical approximation. The pseudopotential affecting states of the  $hh$ -branch in the valence band of the virtual crystal can be obtained using the 3D matrix of Al/Ga distribution  $p_{\vec{r}}$  in an AlGaN supercell. The number of Ga/Al nodes in the unit cell  $n = 2$ , the average lattice constant  $a \approx xa_{\text{GaN}} + (1 - x)a_{\text{AlN}}$ , the average volume of the AlGaN unit cell  $V_0 \approx xV_{0,\text{GaN}} + (1 - x)V_{0,\text{AlN}}$ . Here,  $V_{0,\text{GaN}} = 46.94 \text{ \AA}^3$  and  $V_{0,\text{AlN}} = 42.53 \text{ \AA}^3$  are the volumes of the unit cells of GaN and AlN, respectively [132], [133]. The scale factor  $\kappa$  was set as 6 in accordance with the value of the Gaussian broadening parameter  $\sigma = 2a \approx \frac{\kappa a}{3}$  as used in Ref. [74]. The band offset between GaN and AlN valence bands  $\Delta E$  is set as 1.0 eV assuming that it is 37% of  $\Delta E_g$  [67].

The 3D matrix of Al/Ga distribution  $p_{\vec{r}}$  in an AlGaN supercell was simulated using the thermodynamic model presented in section 2.1 and assuming the uniform distribution type. The simulation was performed in a supercell consisting of  $60 \times 60 \times 60$  nitride unit cells at periodic boundary conditions. Lattice parameters and node positions were obtained as in Ref. [132], [133]. The average lattice vectors  $x\vec{a}_{i,\text{AlN}} + (1 - x)\vec{a}_{i,\text{GaN}}$  were used to build AlGaN supercell, where  $\vec{a}_{i,\text{AlN}}$  and  $\vec{a}_{i,\text{GaN}}$  are the lattice vectors of AlN and GaN crystals, respectively.

Figure 3.1 presents 2D cross sections of the spatial distribution of the total pseudopotential in a  $60 \times 60 \times 60$  AlGaN supercell at different aluminum content. Though the band offset  $\Delta E$  is large, the amplitude of fluctuations is quite small. It is explained by the large value of the scale parameter  $\kappa$  ( $\kappa a = 1.932(1 - 0.054x) \text{ nm}$ ).

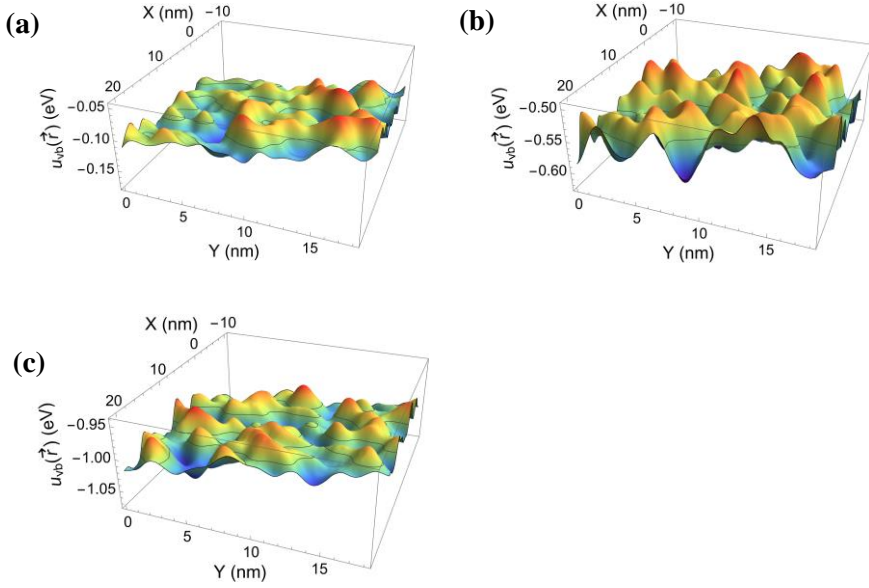


**Fig. 3.1.** Spatial distribution of the pseudopotential  $u(\vec{r})$  in an AlGaIn supercell at the aluminum content of 10% (a), 50% (b), and 90% (c) [A2].

### 3.4. Calculation of the heavy hole-phonon scattering rates in AlGaIn semiconductor

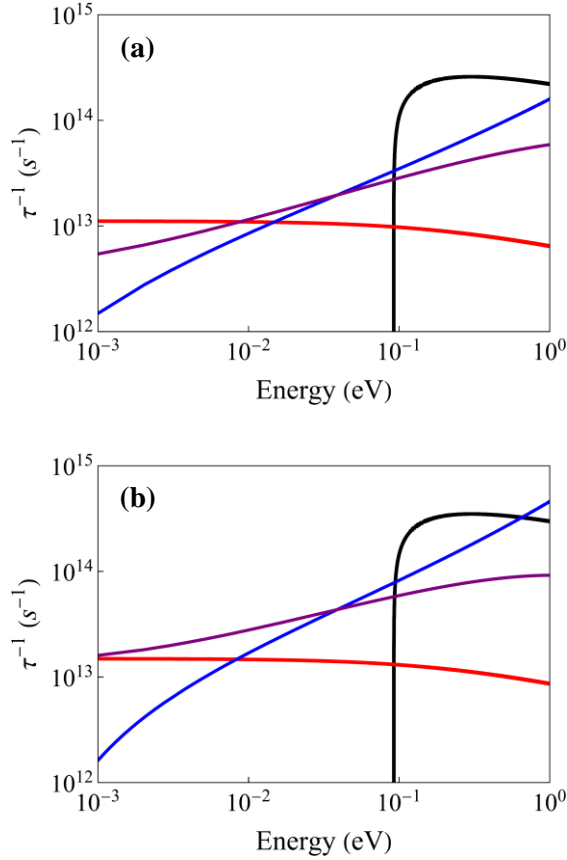
The heavy-hole mobility in polar binary nitride semiconductors at room temperature is predominantly determined by the interaction with longitudinal optical and acoustical phonons [134]. The heavy hole-phonon scattering rates  $\tau_{LO,abs}^{-1,em}$  and  $\tau_{LA,abs}^{-1,em}$  in GaN and AlN crystals can be obtained using the expressions (2.7) taking into account the logarithmic and subintegral terms, respectively. Meanwhile, the heavy hole-phonon interaction rates in AlGaIn compound with strong potential disorder can be evaluated using the modification of  $\tau_{LO,abs}^{-1,em}$  and  $\tau_{LA,abs}^{-1,em}$  described in section 3.2. The GaN and AlN parameters used to calculate the hole-phonon interaction rates are listed in Table 3.1.

**Table 3.1.** Parameters of GaN and AlN semiconductors [74], [134].

	GaN	AlN
$m_{hh}^*(m_e)$	1.87	2.68
$\hbar\Omega_{LO}$ (meV)	92.0	92.2
$\varepsilon_{st}$	9.5	8.5
$\varepsilon_\infty$	5.35	4.77
$c_L$ ( $10^5$ cm/s)	4.4	6.04
$\rho$ ( $\text{g}/\text{cm}^{-3}$ )	5.92	3.2
$\sigma_d$ (eV)	8.3	9.5

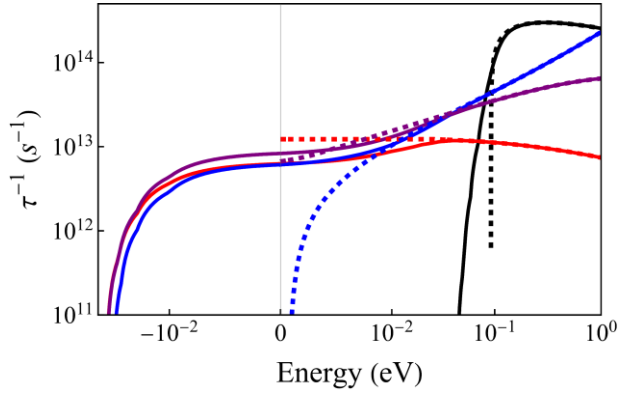
Though the heavy-hole effective mass in GaN is anisotropic close to  $\Gamma$  point, it tends to be isotropic for energies below -10 meV [135]. Since the thermalized heavy holes at room temperature have the average kinetic energy  $\frac{3}{2}k_B T \approx 38$  meV, only a small part of heavy holes is affected by the anisotropy. Thus, an isotropic hole effective mass  $m_{hh}^*$  in GaN crystal was used in our calculations. This approximation is quite accurate in samples with a low aluminum content. The anisotropy of the  $hh$  effective mass should increase at the aluminum content exceeding  $\sim 50\%$ , since the crystal field splitting energies of the opposite sign in AlN and in GaN leads to the change in the valence band ordering in AlGaIn [136]. The anisotropy of the  $hh$  effective mass in nitride semiconductors can be described by more accurate k-p method [135], [137] or using the DFT approach [68]. However, these methods are time-consuming. Thus, an isotropic effective mass approximation was used for calculating the heavy hole-phonon scattering rates, although this approximation might lead to significant errors at high aluminum content.

Figure 3.2 shows the rates of heavy hole scattering due to LO and LA phonon emission and absorption in GaN and AlN single crystals. The amplitudes of the rates of scattering due to LA phonon emission and absorption in both GaN and AlN crystals exceed that due to LO phonon absorption in the vicinity of the average kinetic energy value for thermalized heavy holes ( $\sim 38$  meV). Meanwhile, the rate of heavy hole scattering due to LO phonon emission has the energy threshold of  $\hbar\Omega_{LO}$ . It is worth noting that scattering of heavy holes on the local piezoelectric field generated by phonon oscillations also takes place in AlN and GaN semiconductors. However, such process has a minor effect on the heavy-hole mobility and was not considered under this study [134].



**Fig. 3.2.** Rates of hole-phonon scattering due to LO (black) and LA (blue) phonon emission and LO (red) and LA (purple) phonon absorption as a function of hole kinetic energy in GaN **(a)** and AlN **(b)** [A2].

Figure 3.3 presents the rates of heavy hole scattering due to LO and LA phonon emission and absorption in the Al<sub>0.5</sub>Ga<sub>0.5</sub>N compound. The disorder-induced potential fluctuations in Al<sub>x</sub>Ga<sub>1-x</sub>N compound semiconductor led to the formation of tails of the hole-phonon scattering rates below zero energy of the virtual crystal. Thus, certain localized hole can escape from the localized state by absorbing one or several LA or LO phonons. Meanwhile, a free hole can be captured in a potential well due to the emission of one or several LA or LO phonons. As the result, the thermalized hole can move through AlGa<sub>x</sub>N compound by hopping over potential barriers due to phonon emission and absorption. Tunneling of heavy holes between the potential wells at room temperature is assumed to be negligible under this study.



**Fig. 3.3.** Energy dependence of the rates of hole-phonon scattering due to LO (black) and LA (blue) phonon emission and LO (red) and LA (purple) phonon absorption in disordered  $\text{Al}_{0.5}\text{Ga}_{0.5}\text{N}$  semiconductor [A2]. The hole-phonon scattering rates in the VC approximation are also shown by the dashed lines of corresponding color. The  $x$ -axis scale is a signed log scale with 1 meV offset around zero energy.

### 3.5. Calculation of the alloy scattering rate for free heavy holes in AlGaN semiconductor

The disorder-induced fluctuations of the effective potential in AlGaN semiconductor should lead to elastic scattering of free non-equilibrium carriers, in particular, heavy holes. Such hole scattering might be described by using the quasiclassical approach exploiting the CPA as discussed in section 2.7. It is worth noting that the empirical pseudopotential (2.5) reflects the total effect of compositional disorder in  $(\text{Ga},\text{Al})\text{N}$  semiconductor on the states of heavy holes, i.e. it also contains the contribution of the fluctuations of the spontaneous polarization field and the piezoelectric polarization induced by local strains.

Figure 3.4 shows the alloy scattering rate for heavy holes in AlGaN compound semiconductor at different aluminum content obtained using the CPA-based technique. The magnitude of the alloy scattering rate for thermalized holes in the  $\text{Al}_{0.5}\text{Ga}_{0.5}\text{N}$  semiconductor is close to the heavy hole-phonon scattering rates also presented in Fig. 3.4. Therefore, a strong impact of the alloy scattering on the heavy-hole diffusivity might be expected.

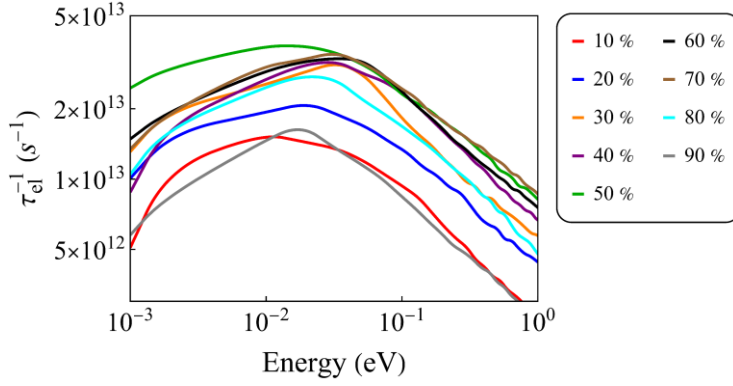


**Fig. 3.4.** Alloy scattering rate as a function of hole kinetic energy in AlGaIn semiconductor at aluminum content varying from 10% to 90% (indicated) [A2].

### 3.6. Simulation of the heavy hole diffusion in AlGaIn semiconductor

The kinetic Monte Carlo method with tracking hole positions can be used to simulate the heavy hole diffusivity in AlGaIn semiconductor. The time step  $\Delta t$  to an event of hole scattering was randomly generated as  $\Delta t = \frac{\log(\frac{1}{\xi})}{\tau_{tot}^{-1}}$ , where  $\xi$  is the random number with the uniform distribution in the range from 0 to 1, whereas the total rate of hole scattering  $\tau_{tot}^{-1}$  is calculated as a sum of the obtained scattering rates. The type of scattering process for each interaction event is randomly generated in accordance with the contribution of each process to the total scattering rate. The quasi-momentum of the emitting or absorbing phonon  $\hbar q$  in the interaction event was generated using the expressions (3.4). The hole energy loss  $\Delta E = E_i - E_f$  in the interaction event with the phonon field was calculated using the phonon dispersion laws  $\hbar\Omega_{LA,vc}(\vec{q}) = \hbar|\vec{q}|c_{L,vc}$  and  $\hbar\Omega_{LO,vc}(\vec{q}) = \hbar\Omega_{LO,vc}(\vec{q} = 0) = \hbar\Omega_{LO,vc}$ . Note that the energy loss value is negative for the phonon absorption events because the initial hole energy  $E_i$  is smaller than the final hole energy  $E_f$  after such event. The scattering direction of a heavy hole after an event of both the alloy scattering and the scattering due to phonon emission or absorption was randomly generated with the isotropic distribution.

The spatial step of a free hole ( $E \geq 0$ ) for the time step  $\Delta t$  was taken as

$$\Delta r = \sqrt{\frac{2E}{m_{hh,vc}^*}} \Delta t. \quad (3.5)$$

Meanwhile, a heavy hole with negative energy  $E$  is considered to be localized at a certain step of the simulation and its velocity is set as zero.

The heavy-hole diffusion coefficient was calculated using the mean squared displacement  $\langle \vec{r}^2 \rangle$  of heavy holes obtained in the simulation for the time period  $t = 100$  ps as

$$D_{hh} = \frac{\langle \vec{r}^2 \rangle}{6t}. \quad (3.6)$$

The simulation was performed in a  $1 \times 1 \times 1 \mu\text{m}^3$  AlGaIn sample at periodic boundary conditions. Since the kinetic energies of photoexcited holes above the average band edge in AlGaIn samples under this study are varied up to 200 meV, heavy holes are randomly generated with the Gaussian energy distribution with the energy dispersion of 10 meV and the peak position of 200 meV above the mobility edge at the beginning of the simulation for all AlGaIn compositions. Meanwhile, low excitation intensity ( $n_{ex} \lesssim 10^{17} \text{ cm}^{-3}$ ) was assumed in the simulation. It allowed neglecting the effect of saturation of the density of localized states associated with the  $hh$ -branch of the valence band as well as the effect of hole-hole and hole-electron scattering processes on the heavy-hole diffusivity. The hole scattering on charged impurities was not taken into account because of the low impurity density in the samples under this study.

Figure 3.5 shows the dependence of the heavy-hole diffusion coefficient on the aluminum content in AlGaIn semiconductor calculated both using the approach taking into account the potential fluctuations and assuming the virtual approximation. In addition, the heavy-hole diffusivity measured using the LITG technique at the excitation density of  $10^{19} \text{ cm}^{-3}$  is presented in Fig. 3.5.

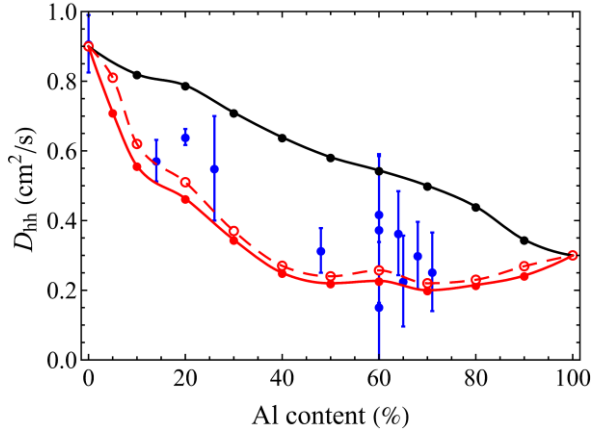


**Fig. 3.5.** Dependence of heavy-hole diffusion coefficient on aluminum content calculated in disordered  $\text{Al}_x\text{Ga}_{1-x}\text{N}$  with (red solid) and without (red dashed) alloy scattering taken into account and in virtual crystal approximation (black) [A2]. The experimental results are presented by blue points. The lines are cubic splines as guides for the eye.

The measured heavy-hole diffusivity coincides well with the result predicted for disordered AlGa $\text{N}$  crystal within the entire range of composition (for  $x$  ranging from 0 to 1). The heavy-hole diffusivities calculated with and without the alloy scattering taken into account are slightly different (see red lines in Fig. 3.5). The alloy scattering slightly affects the heavy-hole diffusivity mainly because of the short average time of holes in free states. As a result, the heavy-hole migration through AlGa $\text{N}$  compound semiconductor is predominantly determined by the process of hopping over potential barriers due to phonon absorption and emission. Meanwhile, the heavy-hole diffusivity in AlGa $\text{N}$  solid solution calculated under the VC approximation demonstrates a substantial discrepancy with the experimental result. The diffusivity obtained under the VC approximation decreases with increasing aluminum content monotonically and slower than the measured diffusivity.

### 3.7. Conclusions

A local-landscape-method-based modification of the quasiclassical expressions of the electron(hole)-phonon scattering rates in the VC approximation for accounting the effect of potential disorder in a crystalline compound was developed. This technique was applied to (Ga,Al) $\text{N}$  semiconductor for calculating the heavy-hole diffusion coefficient. Disorder-



induced fluctuations of the effective potential affecting the states of the *hh*-branch in the valence band of (Ga,Al)N compound were built using the empirical pseudopotential (see section 2.3). This fluctuating pseudopotential was exploited to calculate the alloy scattering rate for heavy-holes and the semiclassical confining potential using the CPA-based technique (see section 2.7) and the local landscape method, respectively. The rates of heavy hole scattering due to phonon emission and absorption in disordered (Ga,Al)N crystal were obtained by integrating the quasiclassical hole-phonon scattering rates in the virtual crystal approximation over the semiclassical confining potential. This method allowed describing the localization process of non-equilibrium holes in potential wells as well as their further thermal escape from the localized states by absorbing one or several LA or LO phonons. Using the obtained scattering rates, 3D diffusion of heavy holes in AlGaN compound semiconductor was simulated using the Monte Carlo method. The heavy-hole diffusivity calculated for disordered AlGaN crystal coincides well with the experimental data obtained by using the light-induced transient grating technique within the entire range of composition. The developed description can be applied to simulate carrier dynamics in other compound semiconductors with strong potential disorder, in particular, in the semiconductors exploited in electronic and photonic devices. The in-plane carrier diffusion lengths are limited by the disorder-induced potential fluctuations in quantum wells. Thus, this effect is important for enhancing the efficiency of  $\mu$ -LEDs, since the minority carriers have a greater chance of diffusing to the sidewall as the chip size decreases. The capability to calculate the carrier mobility is also important for improving the electronic properties of In-rich InGaN and Al-rich AlGaN quantum wells.

## 4. EFFECT OF COMPOSITIONAL DISORDER ON EXCITATION TRANSFER IN GADOLINIUM-CONTAINING GARNET HOST

In this chapter, the effect of compositional disorder on excitation transport through the system of quasiautomatic gadolinium levels in the band gap of a quaternary garnet host was addressed. The excitation transfer via the gadolinium subsystem in binary scintillators was observed experimentally and studied theoretically in [97], [138], [139], [140], [141], [142]. However, when breaking the integrity of the gadolinium sublattice, in particular, in a quaternary garnet host, the transfer process cannot be described by using the methods proposed in those papers. A kinetic Monte Carlo model of excitation transfer through gadolinium sublattice in a quaternary garnet host was presented in Ref. [53]. This model considers the involvement of  $^6\text{P}$  gadolinium multiplets in the excitation transfer to emitting cerium ions and provides only a semiquantitative description of scintillation kinetics under gamma or electron beam excitation. In this chapter, a modification of this model by taking into account the involvement of both  $^6\text{P}$  and  $^6\text{I}$  gadolinium multiplets in the excitation transfer was developed. The extended model was applied to LuGAGG:Ce scintillator for obtaining the CL kinetics under excitation by a 10-keV electron beam. The excitation transfer description was verified by comparing the simulated scintillation decay kinetics with those measured using the time-resolved cathodoluminescence spectroscopy. The introduction of magnesium into the matrix host of Ce-doped garnet-type scintillator leads to the acceleration of scintillation response but deteriorates the scintillator light yield [6]. In this work, the influence of magnesium codoping on the energy transfer via Gd subsystem is revealed.

### 4.1. Experimental technique and results

The experimental results obtained by cathodoluminescence on a sample of Ce-doped garnet-structure  $\text{Lu}_{0.75}\text{Gd}_{2.22}\text{Ce}_{0.03}\text{Ga}_{2.5}\text{Al}_{2.5}\text{O}_{12}$  epitaxial film (sample S1) and two films of the same composition additionally codoped with magnesium at 300 and 700 ppm (samples S2 and S3, respectively) were used in this work. All the layers, 16  $\mu\text{m}$  thick, were deposited on (100)-oriented Czochralski-grown  $\text{Gd}_3\text{Ga}_{2.7}\text{Al}_{2.3}\text{O}_{12}$  substrates by isothermal dipping liquid phase epitaxy using  $\text{BaO-B}_2\text{O}_3\text{-BaF}_2$  flux (see [62] for more details). Glow discharge mass spectroscopy was used to determine the magnesium content in these samples.

The absorption spectra were measured by using a UV-VIS-NIR spectrophotometer Lambda 950 (PerkinElmer). The spectra were obtained at room temperature in the range from 206 to 516 nm (2.4 eV – 6.0 eV) with 1 nm spectral resolution.

Cathodoluminescence (CL) kinetics were measured at room temperature using a time-resolved cathodoluminescence spectrometer (*Chronos, Attolight*) operated at an acceleration voltage of 10 kV. The electron beams pulses were generated at triggering the electron gun by picosecond laser pulses (*aeroPULSE PS, NKT Photonics*). The repetition rate was set as 2.18 MHz. Spatially averaged scintillation response within a select sample area was collected by continuously scanning the area using a Cassegrain-type objective, dispersed by a *Horiba iHR* spectrometer, and recorded using a *Hamamatsu* streak camera. To achieve the best time resolution in different time regions of the decay kinetics the final scintillation response was obtained from multiple-temporal-window measurements.

The photoluminescence (PL) decay kinetics were measured by using *Becker&Hickl* time-correlated single-photon counting (TCSPC) module SPC-130 coupled with cooled photomultiplier PMC-150 (time resolution of 200 ps). The 250-fs pulses with the wavelength of 1030 nm delivered by Yb:KGW (*Pharos, Light Conversion*) laser were used to excite the samples. To tune the excitation photon energy at 2.84 eV necessary for photoexcitation of Ce<sup>3+</sup> ions to 5d<sub>1</sub> level harmonic generators and an optical parametric amplifier (*Orpheus, Light Conversion*) were exploited.

All the measurements are performed at room temperature.

Figure 4.1 shows the absorption spectra of the samples under study. Two absorption bands peaked at 2.8 and 3.6 eV are caused by optical transitions from the ground state to 5d<sub>1</sub> and 5d<sub>2</sub> components of 5d level of Ce<sup>3+</sup> ions split by crystal field. Narrow bands at 4.0 and 4.5 are caused by f-f optical transitions in matrix-building gadolinium ions [143]. The broad band peaked at about 4.5 eV in magnesium-containing samples is caused by a charge transfer transition from the valence band to magnesium-induced trap levels [6].

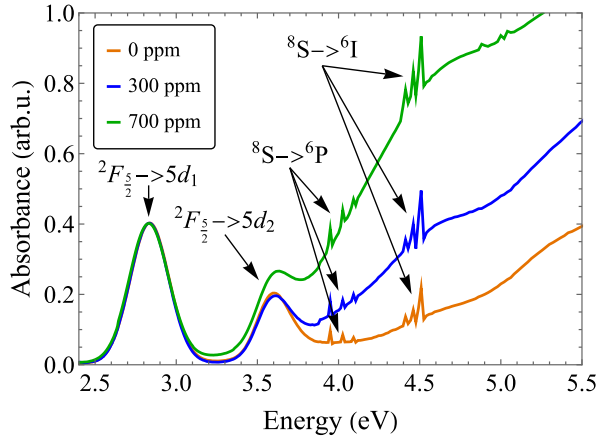


**Fig. 4.1.** Optical absorption spectra of LuGAGG:Ce,Mg layers with different Mg content (indicated) [A3]. The spectra are normalized at the peak of  $Ce^{3+}$   $^{2}F_{5/2} \rightarrow 5d_1$  transition band.

Figure 4.2(a) presents the CL kinetics of samples S1, S2, and S3. The luminescence decay kinetics under 10-keV electron beam excitation and 2.84-eV photoexcitation in samples S1 and S3 are compared in Fig. 4.2(b). The samples exhibit a strong quenching of both CL and PL kinetics with increasing magnesium content. The effect of a strong quenching of luminescence kinetics in LuGAGG:Ce scintillators with strong magnesium co-doping under 2.84-eV photoexcitation was observed in Ref. [63]. As reported, the PL kinetics of LuGAGG:Ce,Mg scintillators consists of, along with a typical 50-ns component of single  $Ce^{3+}$  ion decay, a fast component of magnesium-induced luminescence centers ( $Ce^{3+}+Mg^{2+}$ ) with 7.5-ns time constant. The contribution of such new centers to the PL intensity is proportional to the magnesium content. Thus, an increase in the magnesium content results in accelerating PL decay.

In undoped sample S1, the CL decay proceeds substantially faster than the PL decay, whereas the CL kinetics coincides well with PL kinetics in heavily codoped sample S3. The slower decay of the CL intensity in sample S1 can be caused by an increase in the contribution of excitation transfer to emitting cerium centers via the gadolinium subsystem. This effect was experimentally observed in binary gadolinium-containing systems [97], [138], [139], [140], [141], [142].

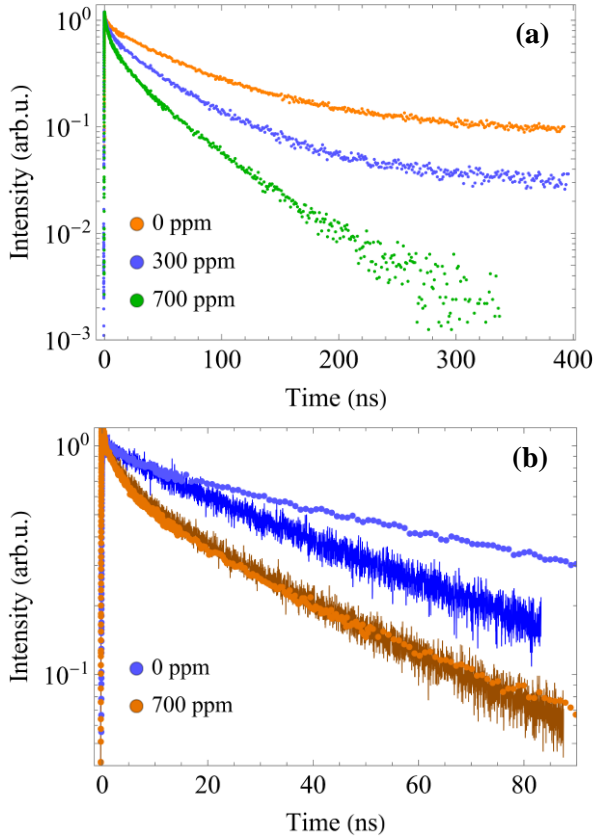


**Fig. 4.2.** (a) Normalized cathodoluminescence kinetics in LuGAGG:Ce,Mg with different Mg content (indicated) and (b) the CL (dots) and PL (curves) kinetics in LuGAGG:Ce samples without magnesium codoping and with 700 ppm of Mg content (indicated) [A3].

#### 4.2. A kinetic Monte-Carlo model of excitation transfer through gadolinium subsystem in quaternary garnet host via the dipole-dipole and Dexter mechanisms

The kinetic MC model presented in Ref. [53] takes into account both the dipole-dipole and Dexter mechanisms of energy transfer from donor  ${}^6\text{P}(\text{Gd}^{3+})$  to acceptor  $5d_2$  ( $\text{Ce}^{3+}$ ) in LuGAGG crystal host. This model predicts a complicated scintillation kinetics consisting of a fast decay component due to the direct excitation of emitting  $\text{Ce}^{3+}$  ions and slower decay component due to the excitation transfer from  $\text{Gd}^{3+}$  to  $\text{Ce}^{3+}$  ions. The involvement of higher gadolinium multiplets ( ${}^6\text{I}$ ,  ${}^6\text{D}$ ) in the excitation transfer has not been discussed there. However, the rate of the energy transfer, in particular, from  ${}^6\text{I}$

gadolinium multiplet to 5d<sub>3</sub> cerium level can be nonzero due to the strong overlap of the 5d<sub>3</sub>-related emission band of cerium and the <sup>6</sup>I-related absorption band of gadolinium [144]. Although a certain Gd<sup>3+</sup> ion initially excited to <sup>6</sup>D multiplet in the result of STE capture quickly decays to <sup>6</sup>P multiplet transiting through <sup>6</sup>I term, the oscillator strength of <sup>8</sup>S→<sup>6</sup>I transition is substantially larger than that of <sup>8</sup>S→<sup>6</sup>P transition, as can be traced in the absorption spectra in Fig. 4.1, to provide a quite large <sup>6</sup>I-related excitation transport rate between two Gd<sup>3+</sup> ions or a pair of Gd<sup>3+</sup> and Ce<sup>3+</sup> ions. Thus, the excitation diffusion through <sup>6</sup>I(Gd<sup>3+</sup>) subsystem as well as the energy transfer from a certain Gd<sup>3+</sup> ion on <sup>6</sup>I multiplet to an unexcited Ce<sup>3+</sup> ion exiting to 5d<sub>3</sub> state might be expected. This effect was experimentally observed in cerium-doped gadolinium oxyorthosilicate (GSO:Ce) scintillator [142]. A modification of the model [53] accounting for the <sup>6</sup>I-related excitation transfer channel to simulate the CL kinetics in the magnesium-free LuGAGG:Ce sample was considered in the current chapter.

The CL intensity in S1 sample is simulated by accumulating the contributions of directly excited Ce<sup>3+</sup> ions and Ce<sup>3+</sup> ions excited due to the excitation transfer from the gadolinium subsystem. Cerium ions initially excited to higher (5d<sub>2</sub>, 5d<sub>3</sub>) levels are considered to be instantaneously relaxed to 5d<sub>1</sub> emitting level, since the non-radiative decay time from 5d<sub>2</sub> to 5d<sub>1</sub> level is quite short (obtained to be ~500 fs in GAGG:Ce [6] and ~700 fs in GYAGG:Ce [A4]). The capture of excitations by 5d<sub>4</sub> and 5d<sub>5</sub> cerium levels was not taken into account because these levels are located deeply in the conduction band.

The concentration of Gd<sup>3+</sup> ions is larger than the concentration of Ce<sup>3+</sup> ions by a factor of 74, whereas the oscillator strength of Ce<sup>3+</sup> ions is about two orders of magnitude larger than that of Gd<sup>3+</sup> ions [53]. Thus, the ratio between the numbers of non-equilibrium carriers initially captured by gadolinium and cerium ions was set as 1:1 in the simulations. The concentration of electron-hole pairs in the ionization area produced by 10-keV *e*-beam in Lu<sub>0.75</sub>Gd<sub>2.22</sub>Ce<sub>0.03</sub>Ga<sub>2.5</sub>Al<sub>2.5</sub>O<sub>12</sub> scintillator assuming strong overlapping of ionization tracks of initial electrons can be evaluated as  $\frac{N_e \cdot 10 \text{ keV}}{2.4 E_g^{LuGAGG}} \frac{1}{\pi r_{th}^2 \langle L \rangle}$  and was obtained to be  $1.1 \cdot 10^{17} \text{ cm}^{-3}$ . Here, the band gap of LuGAGG crystal  $E_g^{LuGAGG}$  was estimated to be 5.88 eV by summing up those of binary components in accordance with their content in the sample. The average displacement of secondary carriers  $r_{th}$  was set as 100 nm, the average track length of initial electrons  $\langle L \rangle$  was obtained by using the GEANT4 package to be 0.78  $\mu\text{m}$ , and the average number of high-energy electrons in the beam

$N_e$  was obtained to be 3.87. Such low excitation density allows neglecting the effect of excitation quenching for a pair of two excited  $\text{Gd}^{3+}$  or  $\text{Ce}^{3+}$  ions interacting through the dipole-dipole and Dexter mechanisms.

The excitation transfer through the gadolinium subsystem to emitting  $\text{Ce}^{3+}$  ions in a LuGAGG supercell as well as the radiative and non-radiative decays of cerium and gadolinium ions can be simulated using the Monte Carlo method. The excitation transfer rate from  $\text{Gd}^{3+}$  to  $\text{Ce}^{3+}$  ions as well as between two  $\text{Gd}^{3+}$  ions separated by the distance  $r$  can be calculated as

$$w_{T_1 \rightarrow T_2}(r) = \frac{1}{\tau_{T_1}} \frac{R_{d-d, T_1 \rightarrow T_2}^6}{r^6} + c_{T_1 \rightarrow T_2} e^{-2\frac{r}{\alpha_{T_1 \rightarrow T_2}}}, \quad (4.1)$$

where  $\tau_{T_1}$  is the emission decay time of  $T_1$  donor state ( ${}^6\text{P}$  or  ${}^6\text{I}$  gadolinium multiplet),  $R_{d-d, T_1 \rightarrow T_2}$  is the dipole-dipole transfer radius between  $T_1$  donor state and  $T_2$  acceptor state ( ${}^6\text{P}$  or  ${}^6\text{I}$  gadolinium multiplet;  $5d_2$  or  $5d_3$  cerium state),  $\alpha_{T_1 \rightarrow T_2}$  is the Dexter transfer radius, and  $c_{T_1 \rightarrow T_2}$  is the frequency factor. The reverse energy transfer from cerium to gadolinium ions is unlikely because of the close-to-zero overlap integral between the hypothetical emission band from  $5d_2$  ( $5d_3$ ) cerium level and the absorption band into  ${}^6\text{P}$  ( ${}^6\text{I}$ ) gadolinium multiplet.

The lutetium, gadolinium, and cerium distributions in a LuGAGG:Ce supercell can be simulated using the Monte Carlo method assuming the uniform cation distribution in accordance with their content in the samples, i.e., 2.22, 0.75, and 0.03 out of 3.0, respectively. The simulation was performed in a  $4 \times 4 \times 4$  garnet supercell at periodic boundary conditions. Lattice parameters and node positions were taken as in Ref. [145], [146], [147], [148]. The average lattice vectors  $\frac{2.22}{2.97} \vec{a}_{i, \text{GAGG}} + \frac{0.75}{2.97} \vec{a}_{i, \text{LuAGG}}$  were used to build LuGAGG:Ce supercell, where  $\vec{a}_{i, \text{GAGG}}$  and  $\vec{a}_{i, \text{LuAGG}}$  are the lattice vectors of GAGG and LuAGG crystals, respectively.

The decay time of  ${}^6\text{I}$  gadolinium multiplet to the ground state was set as that for  ${}^6\text{P}$  multiplet, i.e. 4.25 ms. The kinetic parameters exploited by the rate of excitation transition from  ${}^6\text{P}$  gadolinium multiplet  $w_{6\text{P}(\text{Gd}) \rightarrow T_2}(r)$  were taken as in Ref. [53], [97] and are listed in Table 4.1. The time of  ${}^6\text{I} \rightarrow {}^6\text{P}$  transition and the kinetic parameters exploited by the rate of excitation transition from  ${}^6\text{I}$  gadolinium multiplet  $w_{6\text{I}(\text{Gd}) \rightarrow T_2}(r)$  were obtained from the best fit of the CL kinetics of the magnesium-free sample and are listed in Table 4.1. All excitations were initially located at gadolinium and cerium ions in the ratio 1:1 in the simulation. Herewith, all excited  $\text{Gd}^{3+}$  and  $\text{Ce}^{3+}$  ions are on  ${}^6\text{I}$

multiplet and on  $5d_1$  state, respectively. The simulation was performed for  $10^5$  realizations.

**Table 4.1.** Kinetic parameters used in the simulation.

$\tau_{Gd,6P \rightarrow 8S}$ $4.25 \cdot 10^{-3} s$	$R_{d-d, 6P(Gd) \rightarrow 6P(Gd)}$ $1.48 \text{ nm}$	$R_{d-d, 6P(Gd) \rightarrow 5d_2(Ce)}$ $1.40 \text{ nm}$
$\tau_{Gd,6I \rightarrow 8S}$ $4.25 \cdot 10^{-3} s$	$R_{d-d, 6I(Gd) \rightarrow 6I(Gd)}$ $2.0 \text{ nm}$	$R_{d-d, 6I(Gd) \rightarrow 5d_3(Ce)}$ $2.0 \text{ nm}$
$\tau_{Gd,6I \rightarrow 6P}$ $1.0 \cdot 10^{-5} s$	$C_{6P(Gd) \rightarrow 6P(Gd)}$ $1.9 \cdot 10^{15} s^{-1}$	$C_{6P(Gd) \rightarrow 5d_2(Ce)}$ $2.1 \cdot 10^{13} s^{-1}$
$\tau_{Ce,5d_1 \rightarrow {}^2F_7/2}$ $50 \cdot 10^{-9} s$	$C_{6I(Gd) \rightarrow 6I(Gd)}$ $1.0 \cdot 10^{16} s^{-1}$	$C_{6I(Gd) \rightarrow 5d_3(Ce)}$ $1.0 \cdot 10^{14} s^{-1}$
	$\alpha_{Gd \rightarrow Gd}$ $0.04 \text{ nm}$	$\alpha_{Gd \rightarrow Ce}$ $0.063 \text{ nm}$

### 4.3. Results and discussion

Figure 4.3 presents the CL kinetics of the magnesium-free sample obtained experimentally and its fits obtained using the model taking into account only the transfer channel via the multiplet  ${}^6P(Gd^{3+})$  and via two multiplets  ${}^6P(Gd^{3+})$  and  ${}^6I(Gd^{3+})$ . In addition, the CL kinetics of LuGAGG:Ce layer with the strongest magnesium codoping and its fit using biexponential model reported in Ref. [63] are presented in Fig 4.3.



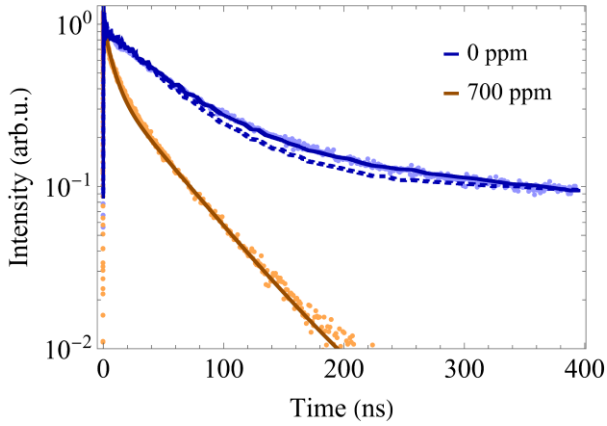


**Fig. 4.3.** Normalized CL kinetics in LuGAGG:Ce,Mg (dots) with different magnesium content (indicated) and their fits (curves) obtained using the model taking into account both types of energy transfer through Gd-subsystem (blue solid line) and only the  ${}^6\text{P}(\text{Gd}^{3+})$ -related transfer channel (blue dashed line) for magnesium-free sample and using the biexponential function with the decay time constants of 50 and 7.5 ns (orange solid line) for the sample with the highest magnesium content [A3].

The CL kinetics calculated using the model taking into account both  ${}^6\text{P}$ - and  ${}^6\text{I}$ -related energy transfer channels in the magnesium-free sample (blue solid line in Fig. 4.3) is in good agreement with the experimental results, whereas the model taking into account only the  ${}^6\text{P}(\text{Gd}^{3+})$ -related energy transfer channel predicts an underestimated contribution of such process in the kinetics of S1 sample (blue dashed line in Fig. 4.3). In comparison with the  ${}^6\text{P}$ -related transfer, the  ${}^6\text{I}$ -related excitation transfer is more pronounced in the ns-time range as seen in Fig. 4.4.

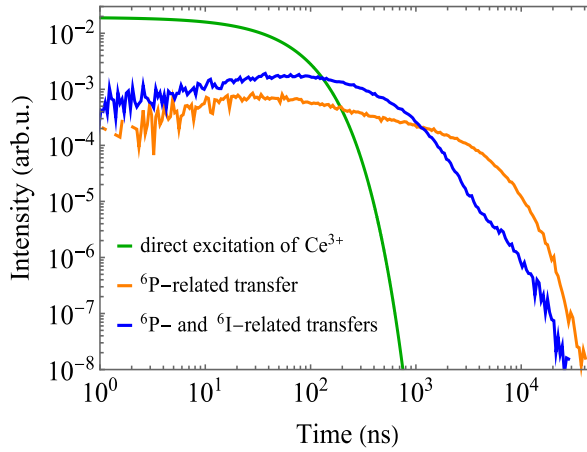


**Fig. 4.4.** Partial contributions in scintillation kinetics by component due to direct excitation of  $\text{Ce}^{3+}$  ions (green) and  $\text{Ce}^{3+}$  ions excited due to the energy transfer from the gadolinium subsystem via the multiplets  ${}^6\text{P}$  (orange) and both  ${}^6\text{P}$  and  ${}^6\text{I}$  (blue) for magnesium-free sample.

The CL kinetics in the heavily Mg-codoped sample can be well described using the biexponential model of intracenter recombination of cerium ions [63] neglecting the Gd-related energy transport effect (orange solid line in Fig. 4.3). The fast luminescence decay in heavily Mg-doped sample might be explained by the intense non-radiative recombination of excited gadolinium ions interacting with trap levels produced by magnesium. The contribution coefficient  $w_1$  of single  $\text{Ce}^{3+}$  centers in the CL kinetics was obtained to be 0.42. It slightly differs from the value reported in Ref. [63] (obtained to be 0.54). This small difference in  $w_1$  might be caused by a difference in the mechanisms of excitation of cerium ions (intracenter excitation vs self-trapped exciton capture).

Figure 4.5 shows the CL kinetics of GAGG:Ce and LuGAGG:Ce scintillators obtained using the model under study. The incorporation of Lu in GAGG:Ce scintillator contributes to a suppression of the fraction of long components in the CL kinetics mainly because of a decrease in the excitation diffusivity and, consequently, decreasing the transport efficiency primarily through long percolation chains.

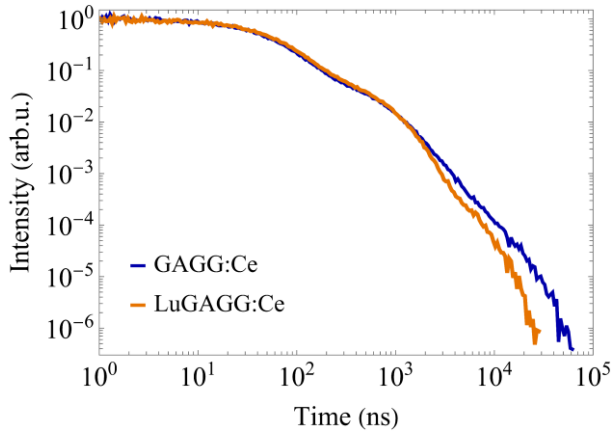


**Fig. 4.5.** Normalized room temperature CL kinetics in GAGG:Ce and LuGAGG:Ce crystals (indicated) obtained using the model taking into account both types of energy transfer through Gd-subsystem.

#### 4.4. Conclusions

A kinetic MC model of excitation transfer through the gadolinium subsystem in a quaternary garnet host was developed. The best coincidence between the CL kinetics of the magnesium-free sample measured by using a hybrid cathodoluminescence-scanning electron microscope and that predicted using the model taking into account the involvement of both  ${}^6\text{P}$  and  ${}^6\text{I}$  gadolinium multiplets in the excitation transport was achieved. Meanwhile, the CL kinetics predicted by the model taking into account only the  ${}^6\text{P}(\text{Gd}^{3+})$ -related energy transfer channel has a significant deviation in the range of the first few hundreds of picoseconds. Thus, an important role of the  ${}^6\text{I}$ -related excitation transfer channel to emitting  $\text{Ce}^{3+}$  ions in gadolinium-containing garnet scintillators was revealed. In addition, a strong quenching of luminescence kinetics with increasing codoping level in LuGAGG:Ce,Mg samples was observed. The CL kinetics of the heavily Mg-codoped sample was described well using the biexponential model with the decay constants attributed to the emission of single  $\text{Ce}^{3+}$  centers and  $\text{Ce}^{3+}+\text{Mg}^{2+}$  centers as reported in Ref. [63]. Consequently, the contribution of emitting  $\text{Ce}^{3+}$  ions excited due to energy transfer from the gadolinium subsystem to the CL intensity is negligible in LuGAGG:Ce,Mg scintillator with strong magnesium codoping. This effect can be interpreted by an increasing absorption due to the broad Mg-related absorption band in the spectral region of  ${}^6\text{P}\rightarrow{}^8\text{S}$  and  ${}^6\text{I}\rightarrow{}^8\text{S}$  transitions at  $\text{Gd}^{3+}$ . This spectral overlap blocks the excitation transfer

via the Gd subsystem, and the emission decay becomes substantially accelerated.

## 5. EFFECT OF COMPOSITIONAL DISORDER ON SPECTRAL PROPERTIES OF CERIUM IONS IN QUATERNARY GARNET SCINTILLATORS

Along with the mobility of non-equilibrium carriers, the compositional disorder affects the spectral properties of emission centers in an inorganic crystalline compound. In the current chapter, the effect of compositional disorder in  $(\text{Gd}_x\text{Y}_{1-x})_3\text{Al}_2\text{Ga}_3\text{O}_{12}:\text{Ce}$  (GYAGG:Ce) scintillators with different yttrium content on the spectral properties of cerium ions was studied. Cerium ions occupy the dodecahedral sites in the garnet host in the trivalent state  $\text{Ce}^{3+}$ .  $\text{Ce}^{3+}$  is a lanthanide ion characterized by the electronic configuration  $[\text{Xe}]4f^1$ . The  $4f^1$  valence electron is predominantly on  ${}^2F_{5/2}$  term at room temperature.  ${}^2F_{5/2}$  and  ${}^2F_{7/2}$  terms are generated by the spin-orbit splitting of  $4f^15d^0$  configuration and separated by  $\sim 0.25$  eV [3]. The emission band of  $\text{Ce}^{3+}$  ions in the garnet host is caused by optical transitions from the lowest component of  $5d$  level split by crystal field of the crystal host to  ${}^2F_{5/2}$  and  ${}^2F_{7/2}$  terms. A review on the effect of shifting the  $5d_1$  and  $5d_2$  cerium energy levels when incorporating Lu or Y ions in dodecahedral sites and Ga ions in tetrahedral and octahedral sites of Ce-doped gadolinium aluminum garnet (GAG:Ce) scintillator was presented in Ref. [3]. In the current chapter, a model of the composite emission band of  $\text{Ce}^{3+}$  ions in GYAGG:Ce scintillator was developed to fit the calculation results to the PL spectra measured experimentally by using a *Becker&Hickl* TCSPC module.

### 5.1. Materials and experimental technique

$\text{Gd}_3\text{Al}_2\text{Ga}_3\text{O}_{12}:\text{Ce},\text{Mg},\text{Ti}$  single crystal sample (S1) and two samples of  $(\text{Gd}_x\text{Y}_{1-x})_3\text{Al}_2\text{Ga}_3\text{O}_{12}:\text{Ce},\text{Mg},\text{Ti}$  with different yttrium content  $x$  of 0.33 and 0.52 (S2 and S3, respectively) were used in the current study. All the crystals were grown by the Czochralski technique in an iridium crucible under a neutral atmosphere containing 1-5 vol.% of oxygen (see [149] for more details). 1 mm-thick polished plates have been prepared for the measurements. The yttrium content was determined by analyzing the composition of the stoichiometric initial charge for the crystal growth. The cerium, magnesium, and titanium content in all samples under study is  $\sim 1000$  ppm,  $\sim 9$  ppm, and  $\sim 9$  ppm, respectively. The samples were additionally codoped by titanium to enhance the stabilization of Ce ions in a trivalent state.

The absorption spectra were measured by using a UV-VIS-NIR spectrophotometer Lambda 950 (PerkinElmer). The spectra were obtained at room temperature in the range from 275 to 700 nm (1.8 eV – 4.5 eV) with 1 nm spectral resolution.

The photoluminescence spectra were measured by using *Becker&Hickl* TCSPC module SPC-130 coupled with cooled photomultiplier PMC-150. The 250-fs pulses with the wavelength of 1030 nm delivered by Yb:KGW (*Pharos, Light Conversion*) laser were used to excite the samples. To tune the excitation photon energy for resonant excitation of Ce<sup>3+</sup> ions, harmonic generators and an optical parametric amplifier (*Orpheus, Light Conversion*) were exploited.

## 5.2. Results and discussion

Figure 5.1 presents the absorption coefficient of the samples under study as a function of photon energy. Two absorption bands peaked at about 2.85 and 3.65 eV are caused by optical transitions from the ground state  $^2F_{5/2}$  to the  $5d_1$  and  $5d_2$  levels of Ce<sup>3+</sup> ions. The absorption band caused by the  $^2F_{5/2} \rightarrow 5d_2$  transition strongly overlaps with the magnesium-induced broad band. This Mg-induced band is caused by a charge transfer transition from the valence band to magnesium-induced trap levels [6].

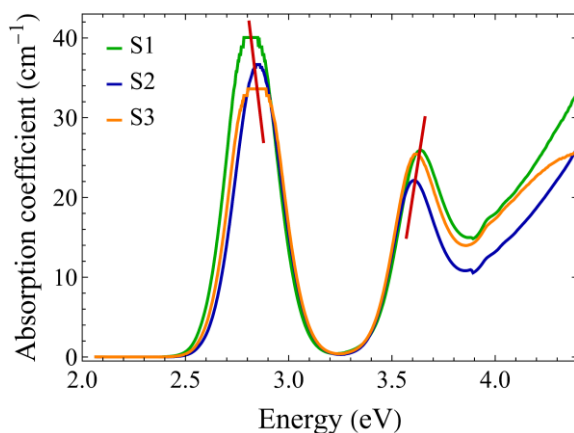


**Fig. 5.1.** Optical absorption spectra of samples S1, S2, and S3 (indicated). Red lines highlight the band peak shifts.

Incorporation of yttrium to GAGG:Ce leads to a blue shift of the band caused by the  $^2F_{5/2} \rightarrow 5d_1$  transition and a red shift of the band caused by the  $^2F_{5/2} \rightarrow 5d_2$  transition. Such trend in (Gd,Y)<sub>3</sub>(Al,Ga)<sub>5</sub>O<sub>12</sub> compounds was

pointed out in the review [3]. Since the influence of the crystal field is quite small for f-levels [3], these shifts are predominantly caused by the shifts in the energy positions of the cerium levels  $5d_1$  and  $5d_2$ . Figure 5.2 presents the same trend for the energy positions of the  $5d_1$  and  $5d_2$  cerium levels in ternary  $(\text{Gd},\text{Y})_3\text{Al}_2\text{Ga}_3\text{O}_{12}$  compounds with different yttrium content reported in the review [3]. The blue and red shifts of the  $5d_1$  and  $5d_2$  cerium levels, respectively, can be explained by a decrease in the splitting of the crystal field affecting  $\text{Ce}^{3+}$  ions when yttrium ions with smaller ionic radii substitute large gadolinium ions in the crystal host.

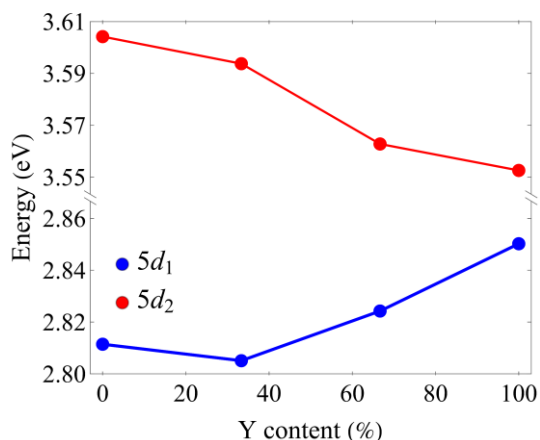


**Fig. 5.2.** Energy positions of cerium levels  $5d_1$  and  $5d_2$  (indicated) in  $(\text{Gd},\text{Y})_3\text{Al}_2\text{Ga}_3\text{O}_{12}$  compound as a function of yttrium content. The plot is created using the data obtained from the review [3].

Figure 5.3 presents the PL spectra of the samples under study at photoexcitation of cerium ions from the ground state  $^2F_{5/2}$  to the levels  $5d_1$  and  $5d_2$  (3.62 eV and 2.83 eV, respectively). The shapes of emission bands at both photoexcitation energies are similar in all samples studied. In addition, all emission bands are strongly asymmetric and have a long tail in the low-energy region caused by multiphonon transitions.

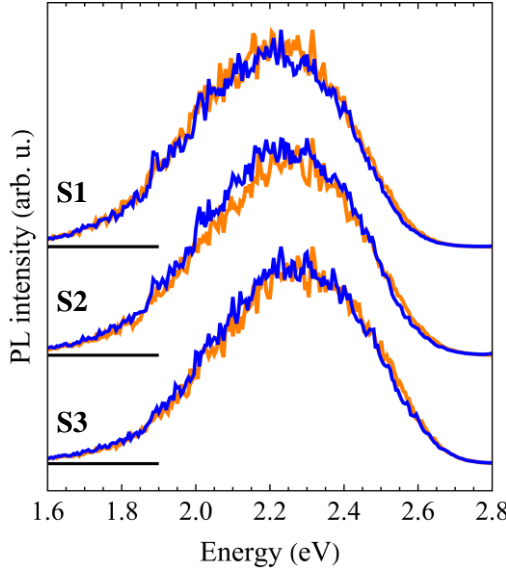


**Fig. 5.3.** Normalized PL spectra of samples S1, S2, and S3 at photoexcitation energies of 3.62 eV (orange) and 2.83 eV (blue) [A4]. The spectra are shifted vertically for clarity.

Since the emission band overlaps with the absorption band caused by the  ${}^2F_{5/2} \rightarrow 5d_1$  transition, the effect of reabsorption should be taken into account when analyzing the emission band shapes. The corrected emission spectra  $S_{corr}(E)$  can be obtained as

$$S_{corr}(E) = S_{ex}(E)r^{-1}(E), \quad (5.1)$$

Here,  $S_{ex}(E)$  is the emission spectrum measured experimentally, and  $r(E)$  is the reabsorption coefficient. Since the characteristic absorption depth of excitation (0.25 mm at 2.83 eV and 0.38 mm at 3.63 eV for S1 sample) is substantially smaller than the thickness of the layers, the reabsorption coefficient  $r(E)$  can be approximated by the following expression for semi-infinite environment [150]:

$$r(E) = \frac{1}{2} \left( 1 - \frac{\alpha(E)}{\alpha(E_{ex})} \ln \left( 1 + \frac{\alpha(E_{ex})}{\alpha(E)} \right) \right), \quad (5.2)$$

where  $\alpha(E)$  is the absorption coefficient, and  $E_{ex}$  is the excitation photon energy (2.83 eV or 3.62 eV).



Figure 5.4 presents the emission and the  ${}^2F_{5/2} \rightarrow 5d_1$  absorption bands as well as the corrected PL spectrum for S1 sample. The reabsorption effect is significant only above  $\sim 2.5$  eV.

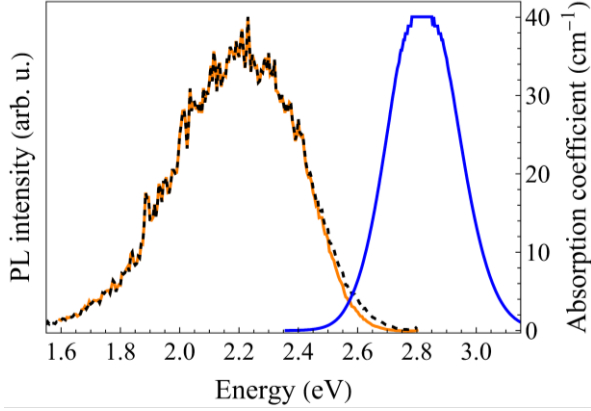


**Fig. 5.4.** Spectra of absorption (blue line) and luminescence (orange line) in sample S1 at the photoexcitation energy of 2.83 eV [A4]. Dashed black line shows the PL band corrected for reabsorption.

The cerium emission band consists of two lines attributed to  $5d_1 \rightarrow {}^2F_{5/2,7/2}$  transitions. The cerium emission spectrum in binary garnets is well described by two overlapping Gaussian bands separated by  $\sim 0.25$  eV [151]. However, this model does not allow satisfactory description of the spectra under study. At least two pairs of Gaussian bands are necessary to fit the calculation results to the measured PL spectra. Thus, the complicated emission band of cerium ions in a quaternary garnet host can be approximated by a pair of doublet band functions  $S_d(E)$  attributed to  $5d_1 \rightarrow {}^2F_{5/2,7/2}$  transitions and taking into account the reabsorption effect. A more accurate approximation for  $S_d(E)$  function can be achieved by using the single band shape function  $G(E)$  for the strong electron-phonon coupling as

$$S_d(E) = r(E) \left( A_1 G(E) + A_2 G(E - 0.25 \text{ eV}) \right), \quad (5.3)$$

where  $G(E)$  can be written as proposed in Ref. [152]:

$$\begin{aligned} G(E) &= \int_{-\infty}^{+\infty} e^{i\frac{E_0}{\hbar}t - s} \left( (1 - \cos(\Omega t)) \text{cth} \left( \frac{\hbar\Omega}{2k_B T} \right) - i \sin(\Omega t) \right) e^{i\frac{E}{\hbar}t} d(\Omega t) = \\ &= e^{-s(\alpha + \beta)} \left( \frac{\alpha}{\beta} \right)^{\frac{\zeta(E)}{2}} I_{|\zeta(E)|} (2\sqrt{\alpha}\sqrt{\beta}S), \end{aligned} \quad (5.4)$$

with

$$\zeta(E) = \frac{E-E_0-S\hbar\Omega}{\hbar\Omega},$$

$$\alpha = \frac{1}{e^{\frac{\hbar\Omega}{k_B T}} - 1},$$

$$\beta = \alpha + 1,$$

Here,  $T$  is the temperature,  $S$  is the Huang-Rhys factor (taken to be 6 [153]),  $\Omega$  is the general optical phonon frequency,  $E_0$  is the phononless transition energy,  $\hbar$  is the reduced Planck constant,  $k_B$  is the Boltzmann constant, whereas  $I_n(x)$  is the modified Bessel function.

The single-band shape function  $G(E)$  can be used also to fit the cerium absorption bands. Along with the emission bands, the absorption bands of cerium should also have a complicated structure caused by the compositional disorder in a quaternary garnet host. However, the widths of these bands are obtained to be smaller than those of the cerium emission bands, because the parameters of the electron-phonon interaction at the  ${}^2F_{5/2} \rightarrow 5d_{1,2}$  transitions differ from those at the  $5d_1 \rightarrow {}^2F_{5/2,7/2}$  transitions. Two disorder-induced lines in each narrow absorption bands of cerium cannot be resolved.

Since the shapes of emission bands at both photoexcitation energies are similar for all samples, only the spectra recorded at the photoexcitation energy of 3.62 eV were considered. Figure 5.5 presents the best fit with the experimental spectra of all samples under study. The ratio between the weight coefficients of low and high lines in each doublet was obtained to be  $\sim 0.7$ , whereas the shift between low energy lines of two doublets was equal to  $\sim 0.20$  eV.

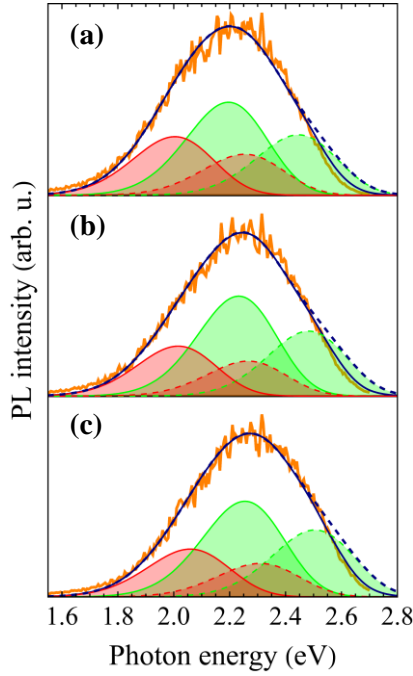


**Fig. 5.5.** PL spectra of samples S1 (a), S2 (b), and S3 (c) and their fits by two pairs of doublet bands (red solid and dashed, green solid and dashed) separated by 0.25 eV in accordance with  $2F_{5/2,7/2}$  splitting without (dashed navy blue) and with (solid navy blue) reabsorption taken into account [A4].

The composite emission band of  $Ce^{3+}$  ions in G(Y)AGG crystal host might be interpreted by the existence of disorder-induced inequivalent dodecahedral sites occupied by  $Ce^{3+}$  ions. For instance, the existence of five inequivalent sites occupied by  $Sm^{3+}$  ions has been revealed in GAGG:Sm scintillator [153]. Since the crystal field splitting mainly affects the cerium levels d, the composite emission band can be caused by a difference in the energy positions of the d levels of cerium ions in inequivalent dodecahedra. In quaternary garnets, dodecahedral sites occupied by  $Ce^{3+}$  ions are surrounded by tetrahedral and octahedral sites occupied by  $Al^{3+}$  and  $Ga^{3+}$  ions (see Fig. 5.6). The two tetrahedral sites sharing edges  $d_{48}$  with a certain dodecahedral site most strongly affect the crystal field in the vicinity of the dodecahedra [3]. The edge length  $d_{48}$  strongly affects the splitting energy between  $5d_1$  and  $5d_2$  cerium levels  $\Delta_{1,2}$  [3]. The edge length  $d_{48}$  is shorter in the tetrahedron occupied by a small  $Al^{3+}$  ion than that in the tetrahedron occupied by a large  $Ga^{3+}$  ion. As reported in Ref. [3], the shorter  $d_{48}$  leads to the larger splitting energy  $\Delta_{1,2}$ . The compositional disorder in the aluminum-gallium subsystem of G(Y)AGG crystal leads to the formation of three sets of filling tetrahedral

sites sharing edges  $d_{48}$  with the dodecahedral sites: two  $\text{Al}^{3+}$  ions, two  $\text{Ga}^{3+}$  ions, or one  $\text{Al}^{3+}$  and one  $\text{Ga}^{3+}$  ions in the tetrahedra. Two of these three sets can be attributed to a pair of doublet bands in the cerium emission spectra.

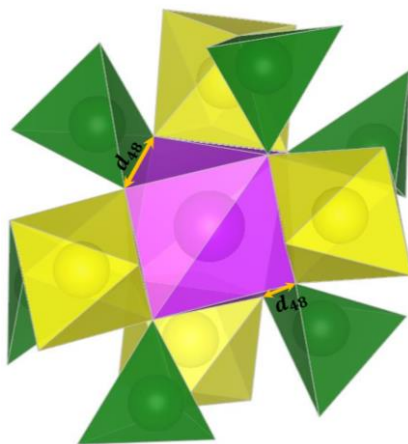


**Fig. 5.6.** Structure of dodecahedral (purple) site for  $\text{Ce}^{3+}$  ion in garnet lattice surrounded by octahedral (yellow) and tetrahedral (green) sites containing  $\text{Al}^{3+}$  and  $\text{Ga}^{3+}$  ions [A4].

As reported in Ref. [154], [155],  $\text{Ga}^{3+}$  ions tend to occupy tetrahedral sites in a garnet host. The occupation probability of an arbitrary tetrahedron by a  $\text{Ga}^{3+}$  ion was obtained to be  $\sim 0.7$  in  $\text{Y}_3\text{Al}_2\text{Ga}_3\text{O}_{12}$  crystal [156]. Using this result, the probability distribution of the number of tetrahedra containing  $\text{Ga}^{3+}$  ions and sharing edges with a certain dodecahedral site occupied by a  $\text{Ce}^{3+}$  ion was obtained by using the Binomial distribution and is presented in Fig. 5.7. The correlation effect in occupation of neighboring sites was neglected.

As seen in Fig. 5.7, the most probable configurations are the tetrahedra occupied both with  $\text{Ga}^{3+}$  ions or one with  $\text{Al}^{3+}$  and another with  $\text{Ga}^{3+}$ . Thus, the high-energy doublet band in the cerium emission spectra can be associated with emitting  $\text{Ce}^{3+}$  ions located in dodecahedral sites sharing edges  $d_{48}$  with the two  $\text{Ga}$ -containing tetrahedra, whereas the low-energy doublet band can be attributed to the intermediate configuration of tetrahedra with  $\text{Ga}^{3+}$  and  $\text{Al}^{3+}$  ions. Meanwhile, the contribution of emitting  $\text{Ce}^{3+}$  ions in the configuration with the two  $\text{Al}$ -containing tetrahedra to the emission spectra was found to be negligible.

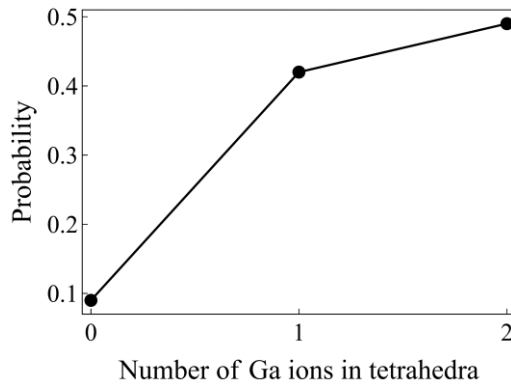


**Fig. 5.7.** The probability distribution for  $\text{Ce}^{3+}$  location among three inequivalent dodecahedra sharing edges with two tetrahedra occupied both with  $\text{Al}^{3+}$ , one with  $\text{Al}^{3+}$  and another with  $\text{Ga}^{3+}$ , and both with  $\text{Ga}^{3+}$  ions [A4].

Figure 5.8 presents the dependences of the peak positions of the low-energy lines in each doublet band on yttrium content. Both lines are blueshifted with increasing yttrium content. Linear fits of these dependences at the line slope obtained from the best fit of the yttrium content dependence of the peak position of the absorption band caused by the  ${}^2\text{F}_{5/2} \rightarrow 5\text{d}_1$  transition in  $\text{Ce}^{3+}$  ions are provided. The linear fits correlate well with the obtained peak positions of the low-energy lines in the doublet bands. This result is in line with the interpretation of the two doublet bands in the composite cerium emission spectrum caused by the compositional disorder in the aluminum-gallium subsystem of G(Y)AGG:Ce scintillator.

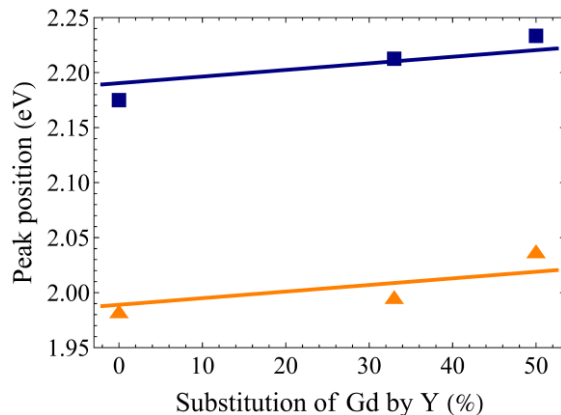


**Fig. 5.8.** The peak positions of the low-energy lines in both doublet bands (dots) as a function of yttrium content and linear fits of the dependences (lines) [A4].

### 5.3. Conclusions

The effect of compositional disorder in Ce-doped ternary and quaternary garnet scintillators on the band shape of the cerium emission spectrum was studied. The performed analysis of the cerium emission spectra in GYAGG matrixes with different yttrium content at photoexcitation of cerium ions from the ground state  $^2F_{5/2}$  to the levels  $5d_1$  and  $5d_2$  enabled to reveal the coexistence of predominantly two spectral components caused by the composition disorder in the aluminum-gallium sublattice. A model of the composite cerium emission spectrum consisting of two doublet bands separated by  $\sim 200$  meV in G(Y)AGG:Ce scintillators was developed and applied for describing the emission spectra of samples under study. The calculation results fit well the measured spectra. The fluctuations of the composition in the aluminum-gallium sublattice of the garnet host lead to the formation of three configurations of filling the tetrahedral sites, i.e., two  $Al^{3+}$  ions, two  $Ga^{3+}$  ions, or one  $Al^{3+}$  and one  $Ga^{3+}$  ions, sharing edges  $d_{48}$  with a Ce-containing dodecahedron. The energy positions of levels  $5d_1$  and  $5d_2$  of  $Ce^{3+}$  ions in dodecahedra are strongly affected by the crystal field splitting, which is affected predominantly by the edge length  $d_{48}$  of dodecahedron sharing it with two tetrahedral sites occupied by  $Ga^{3+}$  and  $Al^{3+}$  ions. The edge length  $d_{48}$  is shorter in the tetrahedron occupied by a small  $Al^{3+}$  ion than that in the tetrahedron occupied by a large  $Ga^{3+}$  ion. Meanwhile, the shorter  $d_{48}$  leads to the larger splitting energy  $\Delta_{1,2}$ . Thus, the low-energy doublet band in the cerium emission spectra is associated with the intermediate configuration of tetrahedra with  $Ga^{3+}$  and  $Al^{3+}$  ions, whereas the high-energy doublet band can be attributed to the configuration of the tetrahedra containing two  $Ga^{3+}$  ions. In addition, a decrease in the splitting between the  $5d_1$  and  $5d_2$  cerium energy levels as well as the blue shifting of the cerium emission band when incorporating Y ions in dodecahedral sites of Ce-doped gadolinium garnet scintillator was observed.

## GENERAL CONCLUSIONS

The developed methods allow describing the dynamic of excitations in crystalline compound scintillators and semiconductors. Summing up the major results obtained in this study enables us to do the following key conclusions:

1. Disorder-induced potential fluctuations in crystalline compound scintillators at room temperature affect the carrier transport in three qualitatively different ways: i) elastic scattering of non-equilibrium carriers on high-frequency core potential fluctuations and ii) fluctuations of the low-frequency potential modulating the band edge, and iii) carrier hopping through disorder-induced potential wells due to phonon emission and absorption.
2. The effect of compositional disorder on the migration of non-equilibrium electrons in lutetium yttrium oxyorthosilicates is weaker than the effect of electron-phonon scattering in the entire energy range.
3. The heavy-hole diffusivity in AlGaN compound semiconductors at room temperature is predominantly determined by the process of hopping over potential barriers due to phonon absorption and emission.
4. The effect of alloy scattering in AlGaN compound semiconductors on the heavy-hole diffusivity is substantially weaker than the effect of hole-phonon scattering. It is more pronounced in low-Al-content crystals where the hole localization is weaker.
5. The slower decay of luminescence at the excitation of high-energy electron-hole pairs in respect to that at the selective excitation to the emitting level  $5d_1$  of  $Ce^{3+}$  ions in Gd-containing garnet type scintillators is caused by excitation transfer via the Gd-subsystem in the scintillator matrix.
6. Excitation transfer to emitting  $Ce^{3+}$  ions via the gadolinium multiplets  ${}^6I_1$ , along with the lowest multiplet  ${}^6P_1$ , provides a significant contribution to the luminescence decay kinetics in Ce-doped Gd-

containing garnet scintillators such as LuGAGG:Ce crystal studied in this thesis work.

7. The introduction of magnesium into Ce-doped Gd-containing garnet scintillators suppresses the slow excitation transfer via the gadolinium subsystem to emitting  $\text{Ce}^{3+}$  ions and, consequently, accelerates the scintillation decay.
8. The acceleration of luminescence decay by Mg codoping of Ce-doped Gd-containing garnet scintillators is caused by the formation of a broad Mg-related absorption band in the spectral region of  ${}^6\text{P} \rightarrow {}^8\text{S}$  and  ${}^6\text{I} \rightarrow {}^8\text{S}$  transitions at  $\text{Gd}^{3+}$  ions.
9. Compositional disorder in the aluminum-gallium sublattice of GYAGG:Ce garnet scintillator affects the cerium emission band splitting it into two doublets separated by  $\sim 200$  meV.
10. The low-energy doublet band of the cerium emission spectra in GYAGG garnet host is associated with the intermediate configuration of tetrahedra containing  $\text{Ga}^{3+}$  and  $\text{Al}^{3+}$  ions and sharing edges  $d_{48}$  with a Ce-containing dodecahedron, whereas sharing the edges with these two tetrahedra containing two  $\text{Ga}^{3+}$  ions results in emission of the high-energy doublet band.



# SANTRAUKA

## ĮVADAS

Neorganinės kristalinės scintiliacinės medžiagos atlieka svarbų vaidmenį aptinkant jonizuojančią spinduliuotę. Scintiliatorius naudojantys spinduliuotės detektoriai yra plačiai paplitę didelių energijų fizikos eksperimentuose, o ypač Europos branduolinių mokslinių tyrimų organizacijos (CERN) atliekamuose eksperimentuose, pasitelkiant Didįji hadronų priešpriešinių srautų greitintuvą (LHC), mediciniame vaizdinime, ypač pozitronų emisijos tomografijos (PET) įrenginiuose, aplinkos monitoringe bei apsaugos sistemose. Neorganiniai kristalai suteikia galimybę derinti didelį medžiagos tankį, kuris užtikrina aukštą stabdymo galią, su lanksčiomis galimybėmis keisti liuminescencijos savybes keičiant medžiagos sudėtį ir pasirenkant aktyvuojančius jonus.

Pastaraisiais metais ceriu legiruoti oksidų dariniai, o visų pirma oksidortosilikatai bei granatai, išpopuliarėjo kaip scintiliacinės medžiagos spinduliuotės detektoriuose [1]. Tokioms medžiagoms būdingas didelis tankis, didelė šviesos išėiga ir spartus scintiliacijos gesimas. Parodyta, kad dariniai, sudaryti iš trijų ar keturių elementų ir turintys granato ar oksidortosilikato struktūrą, pasižymi puikomis scintiliacinėmis savybėmis [2]. Tarpinio spindulio jonų įterpimas į tokias medžiagas leido iš esmės pagerinti jų savybes keičiant juostos tarpą bei kristalinį lauką, kuris veikia aktyvuojančius jonus ir tokiu būdu daro įtaką jonų energijos lygmenims [3], [4]. Be to, kristalinio lauko moduliacija dėl šių junginių sudėties fluktuacijų mažina laisvųjų krūvininkų difuzijos ilgį. Todėl išauga geminantinių elektronų-skylių porų tankis ir dėl to padidėja sužadinimo perdavimo į liuminescencinius centrus efektyvumas. Tolimesnei sparčiųjų daugiakomponenčių kristalinių scintiliacinių medžiagų inžinerijai reikia gilaus teorinio suvokimo, kokį poveikį sudėties netvarkinga daro nestacionariems procesams tokiose sistemose. Daugelio tokių procesų neįmanoma tiesiogiai išmatuoti; tad juos tenka tyrinėti analizuojant integralų atsaką, pavyzdžiui, atsaką, gaunamą pasitelkiant nestacionariosios optinės sugerties metodiką [5], [6].

Be to, sužadinimo perdavimo per kristalinę matricą su sudėties fluktuacijomis tyrimas yra svarbus siekiant geriau suvokti puslaidininkių darinių elektrines ir optines savybes. Išsamus termalizuotų krūvininkų relaksacijos proceso sudėtinuose puslaidininkiuose supratimas tampa itin svarbus siekiant pagerinti vidinį kvantinį našumą (IQE), visų pirma InGaN

šviestukuose (LED) ir lazeriniuose dioduose (LD), spinduliuojančiuose ilgabangėje žalioje srityje, bei AlGaN šviestukuose, spinduliuojančiuose ultravioletinėje srityje [7]. InGaN šviesos šaltiniai yra išskirtinai svarbūs kuriant geresnės spalvinės atgavos šviestukais paremtus vaizduoklius ir lazerinių diodų projektorius. Be to, AlGaN šviestukai gali būti naudojami kaip ultravioletinės šviesos šaltiniai, kuriais būtų galima pakeisti aplinką teršiančias nuodingas gyvsidabrio lempas [8], [9] vandens valymui bei kitose taikymų srityse.

## PAGRINDINIS TIKSLAS IR UŽDAVINIAI

Šiuo tyrimu siekiama teoriškai aprašyti sudėties fluktuacijų kristaliniuose scintiliatoriuose ir puslaidininkiuose poveikį sužadinimo pernašai bei, tuo remiantis, šviesos emisijos spektrui ir laikinėms savybėms daugiakomponenčiuose scintiliatoriuose ir puslaidininkiuose. Siekiant įgyvendinti pagrindinį tyrimo tikslą, buvo iškelti šie uždaviniai:

1. Sukurti pakaitinių jonų pasiskirstymo modelį joniniuose sudėtinuose scintiliatoriuose ir jį pritaikyti ceriu legiruotiems lutecio itrio oksidrosilikato (LYSO) kietiesiems tirpalams, kurie yra perspektyvūs kaip spartūs scintiliatoriai didelio šviesingumo didelių energijų fizikos eksperimentuose bei aukštos erdvinės skyros mediciniame vaizdinime.
2. Sukurti nepusiausvirųjų krūvininkų elastinės sklaidos struktūrinės netvarkos sukeltomis fluktuacijomis teorinį modelį ir juo naudojantis apskaičiuoti sklaidos lydinyje spartą laisviems nepusiausviriesiems elektronams LYSO kristale. Gautus rezultatus palyginti su elektronų sklaidos fononais sparta virtualiojo kristalo apksimacijoje.
3. Sukurti nepusiausvirųjų krūvininkų sąveikos su fononais sudėtinuose scintiliatoriuose ir puslaidininkiuose su didele sudėties netvarka apibendrintą teorinį aprašą.
4. Įvertinti sunkiųjų skylių difuzijos koeficientą AlGaIn puslaidininkyje. Patikrinti gautuosius rezultatus lyginant juos su eksperimentiniais duomenimis, gautais pasitelkus šviesa sužadintų dinaminių gardelių metodiką.
5. Sukurti sužadinimo pernašos per granato kristalą, kuriame yra gadolinio, kinetinį Monte Karlo modelį ir juo naudojantis sumodeliuoti scintiliacijos gesimo kinetiką ceriu legiruotuose granato tipo scintiliatoriuose, atskleisti žadinimo pernašos per gadolinio sistemą scintiliatoriaus matricoje svarbą pasinaudojant gesimo spartos skirtumais žadinant didelės energijos elektronais katodoluminescencijos eksperimentuose ir žadinant šviesa rezonansiškai į  $Ce^{3+}$  lygmenį  $5d_1$ .

6. Atskleisti aliovalentinio legiravimo poveikį sužadavimo pernašai ceriu legiruotuose granato tipo scintiliatoriuose.
7. Ištirti sudėties netvarkos poveikį daugiakomponenčiuose granato tipo scintiliatoriuose spinduliuojančių cerio jonų spektrinėms savybėms.

## NAUJUMAS

Bolcmano kinetinė lygtis naudojanti Blocho savuosius vektorius ir jų savąsias būsenas ir suderintinio potencialo kristalo elementariajame narvelyje matricinius elementus yra gerai žinomas būdas skaičiuoti nepusiausvirųjų krūvininkų judrį tiek taisyklingame kristale, tiek ir daugiakomponenčių scintiliatorių ar puslaidininkų supernarvelyje [10], [11]. Tačiau toks požiūris reikalauja išskirtinai didelių laiko sąnaudų netgi potencialiai turint šiandienines skaičiavimo galimybes. Tuo tarpu dabartiniai kvaziklasikiniai metodai, simuliuojantys nešėjų migraciją per kristalinių scintiliatorių darinius ir puslaidininkius, pasitelkiantys sklaidos lydinyje spartą Borno aproksimacijoje [12], [13] ir atsižvelgiantys į tam tikras nepusiausvirinių krūvininkų sklaidos spartos modifikacijas dėl fononų emisijos ir absorbcijos [13] yra žemo tikslumo, kai krūvininkų energijos yra artimos judrio slenksčiui ir todėl gali būti naudojami tik kai kurioms kristalinėms medžiagoms. Koherentinio potencialo metodas [14] bei lokalaus reljefo metodas [15] leidžia gan tiksliai įvertinti energijos neapibrėžtumą netvarkioje kristalinėje terpėje krūvininkų būsenoms virtualiame kristale [16] ir gali būti pritaikytas modifikuoti turimus kvaziklasikinius metodus.

Pagrindiniai šios disertacijos nauji rezultatai yra šie:

1. Sukurtas bendras nepusiausvirųjų krūvininkų migracijos sudėtiniuose kristaliniuose scintiliatoriuose ir puslaidininkiuose aprašymas. Pateikiamos kvaziklasikinių išraiškų modifikacijos nustatyti sklaidos lydinyje spartai ir elektronų (skylių) sklaidos fononais spartai panaudojant CPA bei lokalaus reljefo metodus. Sukurtą aprašą galima pritaikyti modeliuojant nešėjų dinamiką scintiliatoriuose bei puslaidininkiuose junginiuose su stipria potencialo tvarka.

2. Skirtingai nei ankstesniuose modeliuose, šiame tyrime naudojami metodai yra validūs visame krūvininkų energijų ruože. Pademonstruota, kad sukurtoji strategija yra veiksminga aprašant skylių difuziją daugiakomponenčiuose puslaidininkiuose. Tai suteikė galimybę apskaičiuoti ambipoliarinę difuziją trinariame AlGaIn darinyje, kuri tiksliai atitiko vertes, eksperimentu nustatytas naudojant šviesa sukeltą dinaminių gardelių metodiką. Derinant teorinius ir eksperimentinius rezultatus atskleistos naujos sunkiųjų skylių sklaidos savybės, kurios buvo panaudotos apskaičiuoti sklaidos spartai.

3. Aprašyta didelės energijos elektronų elastingė sklaida šerdies potencialo svyravimais LYSO scintiliaciniame kristale ir įrodyta jos svarba.

4. Paskaičiavus liuminescencijos gesimo žadinant didelės energijos elektronais ir žadinant šviesa rezonansiškai į spinduliuojantįjį  $Ce^{3+}$  jono lygmenį, kiekybiškai pademonstruota sužadavimo pernašos per Gd subsystemą ceriu legiruotuose daugiakomponenčiuose granato tipo scintiliatoriuose svarba.

5. Atskleista, kad sužadavimo pernašai per Gd subsystemą granato tipo gardelėje svarbus ne tik žemiausias multipletas  ${}^6P$ , bet ir multipletas  ${}^6I$ .

6. Palyginus liuminescencijos gesimo kinetikas foto- ir katodoliuminescencijos eksperimentuose tarpusavyje ir su paskaičiuotomis buvo atskleistas to gesimo paspartėjimo esant aliovalentiniam legiravimui mechanizmas.

7. Buvo atskleistas cerio jonų emisijos juostos skilimas dėl sudėties netvarkos Ga-Al posistemėje ceriu legiruotame daugiakomponenčiame granato tipo scintiliatoriuje.

## GINAMIEJI TEIGINIAI

1. Sudėties netvarkos poveikis nepusiausvirųjų elektronų migravimui lutecio itrio oksidortosilikatuose yra silpnesnis nei sklaidos fononais poveikis.
2. Sunkių skylių difuzyvumas sudėtiniame puslaidininkyje AlGaIn kambario temperatūroje yra nulemtas šokavimo per potencialinius barjerus dėl fononų absorbcijos ir emisijos.
3. Greta žemiausios energijos gadolinio multiplieto  ${}^6P$ , multipletas  ${}^6I$  yra svarbus sužadavimo pernašai per gadolinio posistemę granato tipo gardelėje.
4. Cerio emisijos juosta daugiakomponenčiuose granato tipo scintiliatoriuose GYAGG:Ce susideda iš dviejų linijų porų dėl kristalo sudėties netvarkos, dėl kurios atsiranda skirtingas Al ir Ga kiekis dviejose artimiausiose spinduliuojančiojo  $Ce^{3+}$  jono koordinacinėse sferose.

## AUTORIAUS INDĖLIS

Autorius sukūrė sužadavimo pernašos netvarkiuose kristaluose modelį netvarkios sudėties kristaluose, šio modelio taikymą konkreitiems scintiliatoriams bei puslaidininkiniams aptaręs su šios disertacijos vadovu bei kolegomis iš Vilniaus universiteto Fotonikos ir nanotechnologijų instituto, ankstesniu tyrimų šioje srityje vadovu prof. Michailu Koržiku bei nepamainomu patarėju kietojo kūno fizikos teorijos bei scintiliacinių medžiagų srityse prof. Andrejumi Vasiljevu. Visus šiais modeliais paremtus skaičiavimus atliko pats autorius. Kompiuterinė programa naudota Monte Karlo simuliacijoms remiantis šiais modeliais buvo sukurta paties autoriaus nuo pat pradžių naudojant C++ kalbą. Visi eksperimentiniai duomenys, naudojami šiame darbe, buvo gauti autoriaus kolegų iš Vilniaus universiteto Fotonikos ir nanotechnologijų instituto.

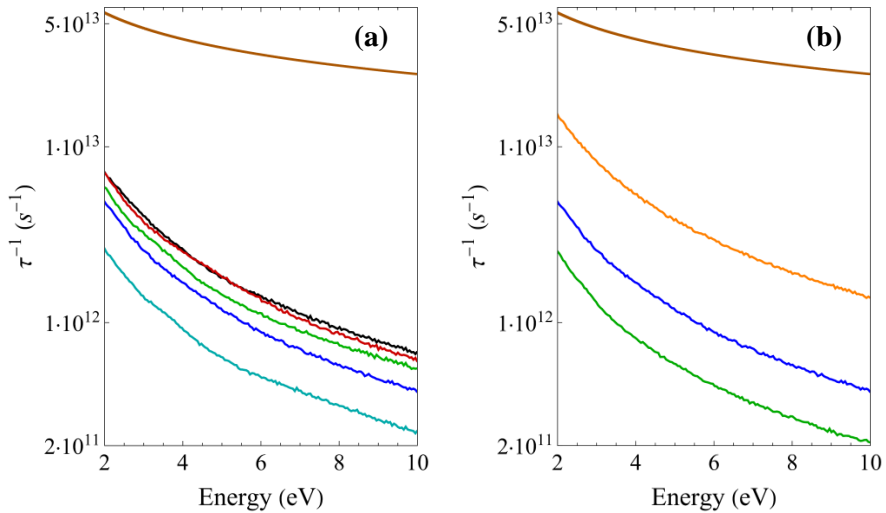
## 6. SUDĖTIES NETVARKOS POVEIKIS NEPUSIAUSVIRŪJŲ KRŪVININKŲ PERNAŠAI MIŠRIUOSE SCINTILIATORIUOSE

Sudėties netvarkos poveikis scintiliaciniuose dariniuose krūvininkų pernašai teoriškai buvo ištirtas šaltinyje [13]. Tame darbe jonų pasiskirstymui pakaitiniame kietajame tirpale simuliuoti buvo naudojamas termodinaminis Monte Karlo modelis. Tuo tarpu daugiakomponenčiuose scintiliatoriuose, tokiuose kaip trinariai granatai ir oksiertosilikatai, yra keletas dešimčių pozicijų kristalo gardelėje, užimtų pakaitiniais jonais. Todėl tokioms sistemoms reikėtų sukurti daugiakomponenčio kietojo tirpalo modelį. Šiame darbe pasiūlyta termodinaminio modelio [13] modifikacija, ir ji pritaikyta LYSO kristalui. Erdvinis lutecio ir itrio katijonų pasiskirstymas LYSO kristale buvo simuliuotas trimis kokybiškai skirtingais katijonų pasiskirstymo atvejais: tolygaus, heterogeninės kaimynystės ir klasterinio pasiskirstymo. Sukurta pseudopotencialo metodu paremta metodika potencialo reljefui LYSO kristale aprašyti. Ši metodika buvo pritaikyta aprašyti elektronų būsenas LYSO kristalo laidumo juostoje. Be to, buvo analizuotas lokalizuotų būsenų tankis LYSO kietajame tirpale panaudojant CPA metodą bei kvaziklasikinį artinį.

### 6.1. Rezultatai ir jų aptarimas

Paveikslas 6.1 pristato sklaidos sudėties fluktuacijomis spartos, gautos naudojant Borno aproksimaciją, ir suminės pernašos spartos dėl sklaidos fononais priklausomybes nuo elektronų kinetinės energijos. Kadangi sklaidą fononais aprašantys parametrai LSO ir YSO kristaluose yra panašaus dydžio, suminė pernašos sparta dėl sklaidos fononais 6.1 paveiksle pateikta tik kristalo su 20% itrio atvejui.

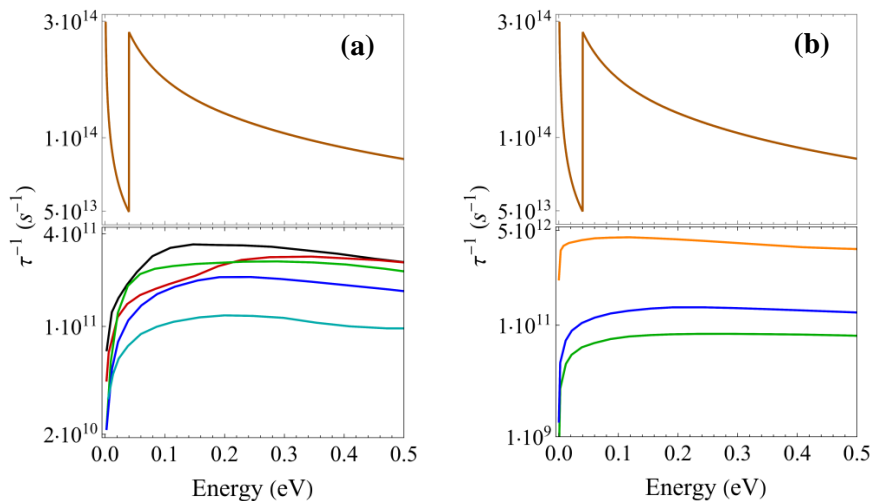




**Pav. 6.1.** Priklausomybės nuo elektronų kinetinės energijos: suminės pernašos spartos dėl sklaidos fononais virtualaus kristalo aproksimacijoje esant 20% itrio (rudos kreivės **(a)** ir **(b)**) ir pernašos spartos dėl sklaidos sudėties fluktuacijomis Borno aproksimacijoje tolygiam katijonų erdviniam pasiskirstymui, kai itrio yra 10% (žalsvai mėlyna), 20% (mėlyna), 30% (žalia), 40% (raudona) ir 50% (juoda) **(a)**; ir esant 20% itrio trims katijonų pasiskirstymo atvejams: tolygaus (mėlyna), heterogeninės kaimynystės (žalia), ir klasterinio (oranžinė) **(b)**.

Gauti rezultatai rodo, kad sklaida sudėties fluktuacijomis yra silpna, palyginus su sklaida fononais.

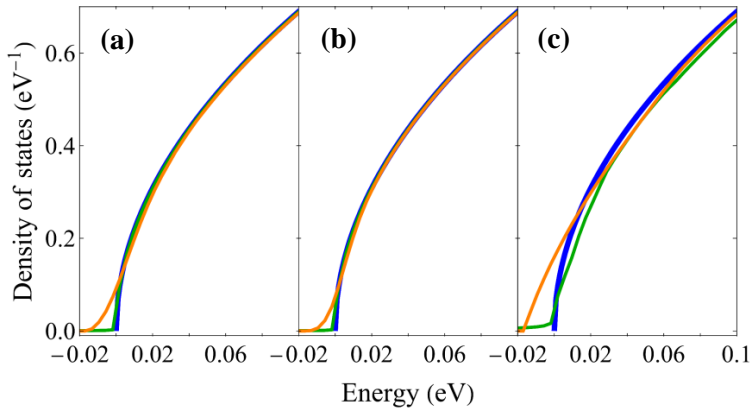
Sklaidos sudėties fluktuacijomis CPA artinyje ir fononų sklaidos ribojamos suminės pernašos spartų priklausomybės nuo elektronų kinetinės energijos pateiktos Pav. 6.2.



**Pav. 6.2.** Priklausomybės nuo elektronų kinetinės energijos: fononų sklaidos ribojamos suminės pernašos virtualaus kristalo aproksimacijoje esant 20% itrio (rudos kreivės (a) ir (b)) ir sklaidos sudėties fluktuacijomis CPA aproksimacijoje esant tolygiam katijonų pasiskirstymui, kai itrio kiekis lygus 10% (žalsvai mėlyna), 20% (mėlyna), 30% (žalia), 40% (raudona) ir 50% (juoda) (a); bei itrio kiekis lygus 20% trims katijonų pasiskirstymo atvejams: tolygaus (mėlyna), heterogeniškos kaimynystės (žalia), ir klasterinio (oranžinė) (b).

Gautosios sklaidos sudėties fluktuacijomis spartos vertės esant mažai elektronų energijai vis dar yra daug mažesnės nei suminė pernašos sparta dėl sklaidos fononais netgi klasterinio katijonų pasiskirstymo atveju. Taigi, mūsų skaičiavimai atskleidė, kad sudėties netvarka LYSO kietajame tirpale turi tik menką poveikį laisvųjų nepusiausvirųjų elektronų migravimui.

Būsenų tankio nepusiausviriesiems elektronams  $\text{Lu}_{1.6}\text{Y}_{0.4}\text{SiO}_5$  kietajame tirpale priklausomybės nuo energijos pateiktos Pav. 6.3. Skaičiavimai atlikti kvaziklasikiniame artinyje ir naudojant CPA metodą trims katijonų pasiskirstymo tipams.



**Pav. 6.3.** Būsenų tankio spektras  $\text{Lu}_{1.6}\text{Y}_{0.4}\text{SiO}_5$  kietajame tirpale, apskaičiuotas panaudojant kvaziklasikinį metodą (oranžinė) ir CPA metodą (žalia) trims katijonų pasiskirstymo atvejams: tolygiam (a), heterogeniškos kaimynystės (b), bei klasteriniam (c) [A1]. Būsenų tankis virtualiajame kristale yra parodytas mėlyna linija. Virtualiojo kristalo laidumo juostos apatinė vertė buvo paimta kaip nulinė energija.

CPA metodas bei kvaziklasikinis artinys leido apskaičiuoti, atitinkamai, žemutines ir viršutines ribas būsenų tankiui neigiamų energijos verčių srityje. Panaudojant vidutinį tarp šių dviejų kraštutinių būsenų tankių, buvo apytiksliai nustatyta, kad lokalizuotų būsenų koncentracija  $\text{Lu}_{1.6}\text{Y}_{0.4}\text{SiO}_5$  kristale lygi  $3,7 \cdot 10^{17} \text{ cm}^{-3}$ , kas yra gana didelė vertė. Pavyzdžiui, nepusiausvirųjų elektronų koncentracija jonizacijos take, kurį sukuria 100 keV energijos elektronas  $\text{Lu}_{1.6}\text{Y}_{0.4}\text{SiO}_5$  kristale apytiksliai lygus  $1,1 \cdot 10^{16} \text{ cm}^{-3}$ . Taigi, yra didelė tikimybė, kad visi antriniai elektronai po terminės relaksacijos bus lokalizuoti. Tačiau potencialo fluktuacijų gylis LYSO kietajame tirpale su tolygiu katijonų pasiskirstymu yra gana nedidelė. Todėl lokalizuotas elektronas gali greitai palikti potencialo minimumą dėl LO fononų ar mažo bangos ilgio LA fonono sugerties. Taigi, šie vertinimai atskleidžia, kad sudėties netvarkos poveikis nepusiausvirųjų elektronų, kurių energija yra artima mobilumo slenksčiui, migracijai LYSO kietajame tirpale taip pat yra silpna.

## 6.2. Išvados

Sukurtas teorinis nepusiausvirųjų krūvininkų sklaidos daugiakomponenčiuose joniniuose scintiliatoriuose su sudėties netvarka aprašymas ir pritaikytas LYSO kietajam tirpalui. Sklaidos sudėties

fluktuacijomis sparta LYSO junginyje buvo apskaičiuota ties apatine ( $0 < E_k < 0.3$  eV) ir viršutine ( $E_k > 7.2$  eV) energijos asimptotinėmis ribomis, atitinkamai pasitelkiant CPA ir Borno aproksimacijos metodus. Netvarkos sukelti potencialo svyravimai kristaliniuose sudėtinuose scintiliatoriuose kambario temperatūroje veikia krūvininkų pernašą dėl nepusiausvirųjų krūvininkų elastingos sklaidos aukštadažnėmis branduolinio potencialo fluktuacijomis, sklaidos žemo dažnio potencialo svyravimais, moduluojančiais juostos pakraštį, ir dėl nešėjų šokavimo per netvarkos suformuotas potencialo duobes dėl fononų emisijos ir absorbcijos. Sudėties netvarkos poveikis nepusiausvirųjų elektronų migracijai lutecio itrio oksidorsilikatuose yra silpnas, nei elektronų-fononų sklaidos visame energijų ruože.

## 7. SUDĖTIES NETVARKOS POVEIKIS NEŠĖJŲ DIFUZIJAI SUDĖTINIUOSE PUSLAIDININKIUOSE

Elektronų (skylių)-fononų sąveikos sparta virtualiojo kristalo aproksimacijoje yra paskaičiuojama gerai, kuomet nešėjo energija daug viršija netvarkos sukkelto pseudopotencialo fluktuacijų amplitudę, tačiau tokių skaičiavimų tikslumas yra žemas, jei nešėjo energija yra artima mobilumo slenksčiui. Šiame darbe pasiūlyta elektronų (skylių)-fononų sklaidos spartos skaičiavimo virtualaus kristalo aproksimacijoje modifikacija panaudojant lokalaus reljefo metodą. Ši technika buvo pritaikyta AlGaN puslaidininkiui, kuriame buvo apskaičiuotas sunkiųjų skylių difuzijos koeficientas. Netvarkos sukeltos efektyvaus potencialo fluktuacijos paveikiančios  $hh$ -šakos būsenas AlGaN valentingumo juostoje buvo sugeneruotos panaudojant pseudopotencialo metodu paremtą techniką. Simuliacijos rezultatai buvo palyginti su eksperimentiniais rezultatais, gautais panaudojant šviesos sukeltų dinaminių gardelių techniką.

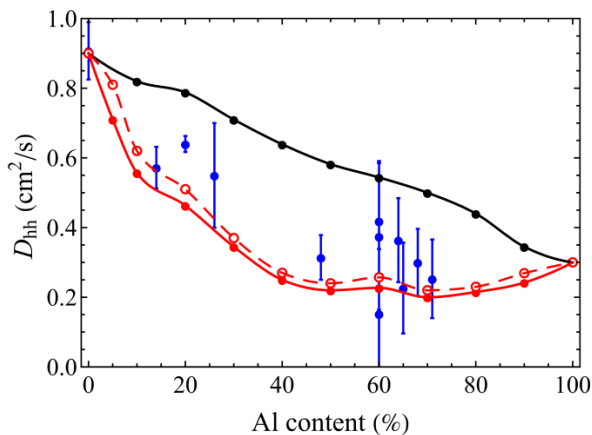
### 7.1. Medžiagos ir eksperimentinės metodikos

Eksperimentiniam tyrimui buvo panaudota 12  $\text{Al}_x\text{Ga}_{1-x}\text{N}$  epitaksinių sluoksnių, kuriuose aliuminio dalis  $x$  svyravo nuo 10% iki 70%. Palyginimui buvo tirtas ir vienas aliuminio neturintis GaN sluoksniu. Medžiagos buvo užaugintos panaudojant metalorganinį cheminį nusodinimą iš garų fazės (MOCVD).

Šviesos sukeltų dinaminių gardelių (LITG) metodika buvo panaudota gauti nepusiausvirųjų krūvininkų ambipolarinės difuzijos koeficiento  $D_a$  vertes tiriamuose bandiniuose. Iš matavimų buvo nustatyta sunkiųjų skylių difuzijos koeficiento vertė  $D_{hh} = \frac{D_a}{2}$  [131].

### 7.2. Rezultatai ir aptarimas

Paveiksle 7.1 pavaizduota sunkiųjų skylių difuzijos koeficiento priklausomybė nuo aliuminio dalies AlGaN puslaidininkyje, kuri buvo apskaičiuota virtualiojo kristalo artinyje ir įskaitant sudėties tankio fluktuacijas. Ten pateikiamos ir sunkiųjų skylių difuzijos koeficiento vertės, eksperimentiškai nustatytos panaudojant LITG techniką esant nepusiausvirųjų krūvininkų koncentracijai  $10^{19} \text{ cm}^{-3}$ .



**Pav. 7.1.** Sunkiųjų skylių difuzijos koeficiento priklausomybė nuo aliuminio dalies, apskaičiuota netvarkios sudėties  $\text{Al}_x\text{Ga}_{1-x}\text{N}$  kristale įskaitant (raudona ištinė linija) ir neįskaitant sklaidą sudėties fluktuacijomis (raudona punktyrinė linija) bei virtualaus kristalo aproksimacijoje (juoda linija) [A2]. Eksperimentiniai rezultatai yra parodyti mėlynais taškais. Linijos yra kubiniai splainai, palengvinantys informacijos suvokimą.

Išmatuotas sunkiųjų skylių difuzijos koeficientas gerai atitinka rezultatą, paskaičiuotą netvarkios sudėties  $\text{AlGaN}$  kristalui per visą sudėties ruožą (kur  $x$  kinta nuo 0 iki 1). Sunkiųjų skylių migracija sudėtiniame  $\text{AlGaN}$ , visų pirma, yra apspręsta šokavimo per potencialo barjerus sugeriant ir emituojant fononus. Tuo tarpu sunkiųjų skylių difuzijos koeficientas  $\text{AlGaN}$  kristale, apskaičiuotas pagal virtualaus kristalo aproksimaciją, labai skiriasi nuo eksperimentinių rezultatų.

### 7.3. Išvados

Pasiūlyta elektronų (skylių)-fononų sklaidos spartos skaičiavimo virtualaus kristalo aproksimacijoje modifikacija panaudojant lokalaus reljefo metodą leidžia paskaičiuoti sunkiųjų skylių difuzijos koeficiento vertes  $\text{AlGaN}$  junginyje su skirtingu aliuminio kiekiu tarp dvinarių junginių  $\text{GaN}$  ir  $\text{AlN}$ , kurios gerai atitinka eksperimentiškai nustatytas vertes. Atlikti skaičiavimai leido padaryti išvadą, kad sunkiųjų skylių difuzyvumą sudėtiniame puslaidininkyje  $\text{AlGaN}$  kambario temperatūroje nulemia šokavimas per potencialinius barjerus dėl fononų absorbcijos ir emisijos. Sklaidos sudėties fluktuacijomis sudėtiniame puslaidininkyje  $\text{AlGaN}$  poveikis sunkiųjų skylių difuzyvumui yra žymiai silpnesnis nei skylių-fononų sklaidos

poveikis. Jis ryškiau pasireiškia kristaluose, kuriuose aliuminio dalis yra nežymi ir skylių lokalizacija yra silpnesnė.

## 8. SUDĖTIES NETVARKOS POVEIKIS SUŽADINIMO PERNAŠAI GADOLINIO TURINČIAME GRANATO TIPO KRISTALE

Šiame darbe buvo tiriamas struktūrinės netvarkos poveikis žadinimo pernašai per gadolinio kvaziatominius lygmenis keturnarių granatų draustiniame tarpe. Disertaciniame darbe buvo sukurta šio modelio modifikacija, kad būtų atsižvelgiama į tai, jog sužadavimo pernašoje dalyvauja tiek  ${}^6\text{P}$ , tiek ir  ${}^6\text{I}$  gadolinio multiplėtai. Patobulintas modelis buvo pritaikytas aprašyti LuGAGG:Ce scintiliatoriaus katodoluminescencijos kinetiką. Skaičiavimų rezultatai buvo lyginami su eksperimentiniais rezultatais.

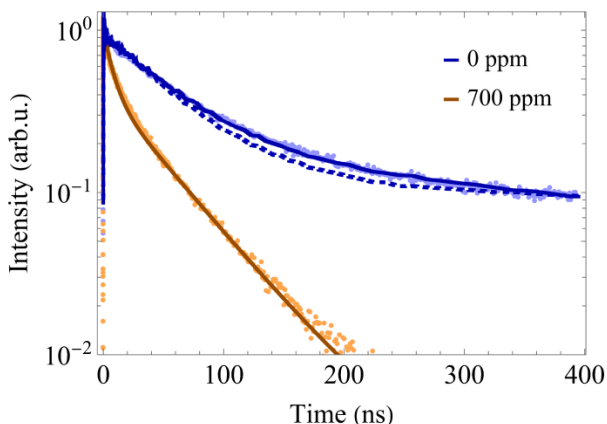
### 8.1. Eksperimento metodika ir rezultatai

Šiame darbe eksperimentiniai rezultatai buvo gauti katodoluminescencijos su laikine skyra metodu tiriant ceriu legiruoto granato struktūros  $\text{Lu}_{0.75}\text{Gd}_{2.22}\text{Ce}_{0.03}\text{Ga}_{2.5}\text{Al}_{2.5}\text{O}_{12}$  epitaksinį sluoksnį bei du tos pačios sudėties sluoksnius, 300 ppm ir 700 ppm kolegiruotus magniu. Katodoluminescencijos kinetika buvo išmatuota kolegų iš Fotonikos ir nanotechnologijų instituto naudojant katodoluminescencinį spektrometrą su laikine skyra. Fotoluminescencijos gesimo kinetika buvo išmatuota koreliuoto laike pavienių fotonų skaičiavimo metodu. Visi matavimai buvo atlikti kambario temperatūroje.

### 8.2. Rezultatai ir aptarimas

Paveiksle 8.1 pateikta išmatuota katodoluminescencijos kinetika bandinyje be kolegiravimo magniu ir tos priklausomybės teorinio skaičiavimo priderinimo rezultatai, kai teorinis modeliavimas įskaito tik į pernašos kanalą per multiplėtą  ${}^6\text{P}(\text{Gd}^{3+})$  ir per du multiplėtus  ${}^6\text{P}(\text{Gd}^{3+})$  bei  ${}^6\text{I}(\text{Gd}^{3+})$ . Šiame paveiksle pateikta ir katodoluminescencijos kinetika LuGAGG:Ce sluoksnyje su didžiausiu kolegiravimu magniu bei šios kinetikos aproksimacija biekspontiniu modeliu [63].





**Pav. 8.1.** Normuota katodoliuminescencijos kinetika LuGAGG:Ce,Mg sluoksnyje (taškai) su magnio kiekiu, kaip nurodyta paveiksle, ir geriausio atitikimo teorinės priklausomybės (kreivės), kuomet atsižvelgiama į pernašą per du,  ${}^6\text{P}$  ir  ${}^6\text{I}$ ,  $\text{Gd}^{3+}$  multipletus (ištisa mėlyna linija) ir tik per vieną multipletą  ${}^6\text{P}$  (mėlyna punktyrinė linija) bandiniui be magnio bei biekspontinė su gesimo trukmėmis 50 ns ir 7.5 ns (ištisa oranžinė linija) bandiniui su didžiausiu magnio kiekiu [A3].

Katodoliuminescencijos kinetika, apskaičiuota, naudojant modelį, atsižvelgiantį tiek į pernašą per  ${}^6\text{P}$ , tiek ir per  ${}^6\text{I}$  gerai atitinka eksperimentinius rezultatus.

### 8.3. Išvados

Sukurtas modelis, leidžiantis panaudojant Monte Karlo metodiką paskaičiuoti sužadinimo pernašos per gadolinio posistemę keturnariame granato tipo kristale parametrus. Lėtesnis liuminescencijos gesimas žadinant didelės energijos elektronais nei esant rezonansiniam žadinimui šviesa į  $\text{Ce}^{3+}$  jonų lygmenį  $5d_1$  gadolinio turinčiuose granato tipo scintiliatoriuose yra sukeltas sužadinimo pernašos per gadolinio posistemę scintiliatoriaus matricoje. Greta žemiausios energijos gadolinio multipletu  ${}^6\text{P}$ , multipletas  ${}^6\text{I}$  reikšmingai prisideda prie liuminescencijos gesimo kinetikos ceriu legiruotuose gadolinio turinčiuose granato tipo scintiliatoriuose, tokiuose kaip LuGAGG:Ce kristalas, kuris buvo tirtas šioje disertacijoje.

## 9. SUDĖTIES NETVARKOS POVEIKIS SPEKTRINĖMS CERIO JONŲ SAVYBĖMS KETURNARIUOSE GRANATO TIPO SCINTILIATORIUOSE

Struktūrinė netvarka neorganiniuose kristaliniuose dariniuose veikia ne tik krūvininkų judrį, bet ir emisijos spektrines savybes. Šiame darbe buvo tyrinėtas sudėties netvarkos  $(\text{Gd}_x\text{Y}_{1-x})_3\text{Al}_2\text{Ga}_3\text{O}_{12}:\text{Ce}$  (GYAGG:Ce) scintiliatoriuose su įvairiu itrio kiekiu poveikis spektrinėms cerio jonų savybėms. Buvo sukurtas  $\text{Ce}^{3+}$  jonų juostos emisijos modelis GYAGG:Ce scintiliatoriuje. Teoriniai spektrų skaičiavimai buvo derinti su eksperimentiškai gautais spektrais.

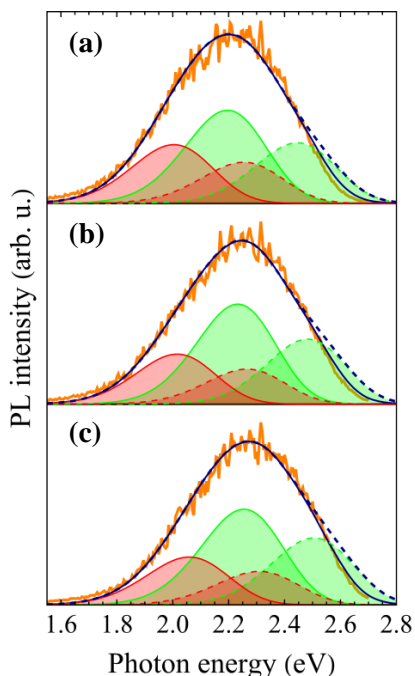
### 9.1. Medžiagos ir eksperimentų metodikos

Buvo tirta vienas kristalas  $\text{Gd}_3\text{Al}_2\text{Ga}_3\text{O}_{12}:\text{Ce},\text{Mg},\text{Ti}$  be itrio ir du bandiniai  $(\text{Gd}_x\text{Y}_{1-x})_3\text{Al}_2\text{Ga}_3\text{O}_{12}:\text{Ce},\text{Mg},\text{Ti}$  su skirtingu itrio kiekiu  $x$ : 0.33 ir 0.52. Visi kristalai buvo užauginti Čiochralskio būdu iridžio tiglyje palaikant neutralią atmosferą, kurioje buvo 1–5% deguonies (pagal tūrį) (šaltinyje [149] pateikta daugiau detalių).

Fotoluminescencijos spektrai buvo matuojami su laikine skyra naudojant laike koreliuoto pavienių fotonų skaičiavimo metodiką. Visi matavimai buvo atlikti kambario temperatūroje.

### 9.2. Rezultatai ir aptarimas

Paveiksle 9.1 pateikt eksperimentiniai spektrai ir geriausiai juos atitinkantys modeliavimo rezultatai visuose bandiniuose, kuomet fotosužadinimo energija lygi 3.62 eV. Buvo nustatyta, kad santykis tarp kiekvieno dubleto apatinės ir viršutinės linijos svorio koeficientų lygus  $\sim 0.7$ , o poslinkis tarp dviejų dubletų apatinių energijos linijų lygus  $\sim 0.20$  eV.



**Pav. 9.1.** Fotoluminescencijos spektrai bandiniuose su skirtingu kolegiravimo magniu lygiu [0, **(a)**, 0.33 **(b)**, ir 0.52 **(c)**] ir jų aproksimacijos dviem poromis juostų (atitinkamai, raudona ir žalia ištinės bei punktyrinės linijos), kurias skiria 0.25 eV dėl lygmens  ${}^2F_{5/2,7/2}$  skilimo, neatsižvelgiant į reabsorbciją (punktyrinė tamsiai mėlyna linija) ir atsižvelgiant į reabsorbciją (ištinė tamsiai mėlyna) [A4].

Sudėtinė  $Ce^{3+}$  jonų emisijos juosta GYAGG kristale gali būti paaiškinta netvarkos sukeltų neekvivalentiškų dodekaedrinių padėčių šiems jonams egzistavimu. Kadangi skilimas dėl kristalinio lauko visų pirma paveikia cerio jonų lygmenį  $d$ , tai šią emisijos juostą galėjo sąlygoti  $d$  lygmenų energijos skirtumas neekvivalentčiuose dodekaedruose. Keturiuose granatuose dodekaedrinės vietas užima  $Ce^{3+}$  jonai, kuriuos supa tetraedriniai ir oktaedriniai dariniai, užimti  $Al^{3+}$  arba  $Ga^{3+}$  jonais. Šie du tetraedriniai dariniai, turintys bendras kraštines  $d_{48}$  su dodekaedriniu dariniu, stipriausiai veikia kristalinį lauką [3]. Kraštinių ilgis  $d_{48}$  stipriai veikia skilimo tarp  $5d_1$  ir  $5d_2$  cerio lygmenų energiją  $\Delta_{1,2}$  [3]. Kraštinių ilgis  $d_{48}$  yra trumpesnis tetraedre, kurį užima mažas  $Al^{3+}$  jonas, nei tetraedre, kurį užima didelis  $Ga^{3+}$  jonas. Kuo trumpesnis  $d_{48}$ , tuo didesnė skilimo energija  $\Delta_{1,2}$  [3]. Dėl netvarkos GYAGG kristale susidaro galimybė susiformuoti trims tetraedrų užpildymo variantams: du  $Al^{3+}$  jonai, du  $Ga^{3+}$  jonai, arba vienas  $Al^{3+}$  jonas ir vienas  $Ga^{3+}$  jonas

tetraedruose. Du iš šių trijų rinkinių gali būti priskirti dubletinėms juostų poroms cerio emisijos spektruose.

### 9.3. Išvados

Buvo ištirtas sudėties netvarkos poveikio cerio emisijos spektro juostos formai ceriu legiruotuose granato struktūros daugiakomponenčiuose scintiliatoriuose. Sudėties netvarka GYAGG:Ce granato scintiliatoriaus aliuminio-galio subgardelėle paveikia cerio emisijos juostą ir suskaido ją į du dubletus, kuriuos skiria maždaug 200 meV. Žemos energijos dubletų juosta cerio emisijos spektruose GYAGG granato matricoje yra susijusi su tarpine tetraedrų konfigūracija, kai  $Ga^{3+}$  ir  $Al^{3+}$  jonų turintys tetraedrai turi bendrą kraštinę  $d_{48}$  su cerio turinčiu dodekaedru; tuo tarpu, kai yra bendros kraštinės su tetraedrais, kuriuose yra du  $Ga^{3+}$  jonai, susidaro didelės energijos dubleto juosta.

## BENDROSIOS IŠVADOS

Sukurti metodai leidžia aprašyti sužadavimo dinamiką daugiakomponenčiuose kristaliniuose scintiliatoriuose ir puslaidininkiuose. Apibendrinant pagrindinius šiame tyrime gautus rezultatus galime prieiti šių svarbiausių išvadų:

1. Netvarkos sukelti potencialo svyravimai kristaliniuose sudėtiniuose scintiliatoriuose kambario temperatūroje veikia krūvininkų pernašą trimis kokybiškai skirtingais būdais: i) nepusiausvirųjų krūvininkų elastinė sklaida aukštadažnėmis branduolinio potencialo fluktuacijomis; ii) žemo dažnio potencialo svyravimais, moduluojančiais laidumo juostos dugną; ir iii) nešėjų šokavimu per netvarkos suformuotus potencialo duobes dėl fononų emisijos ir absorbcijos.
2. Sudėties netvarkos poveikis nepusiausvirųjų elektronų migracijai lutecio itrio oksidortosilikatuose visame energijų ruože yra silpnas nei elektronų-fononų sklaidos.
3. Sunkiųjų skylių difuzyvumą sudėtiniame puslaidininkyje AlGaIn kambario temperatūroje lemia šokavimas per potencialinius barjerus dėl fononų absorbcijos ir emisijos.
4. Sklaidos sudėties fluktuacijomis sudėtiniame puslaidininkyje AlGaIn poveikis sunkiųjų skylių difuzyvumui yra žymiai silpnas nei skylių-fononų sklaidos poveikis. Jis ryškiau pasireiškia kristaluose, kuriuose aliuminio dalis yra nežymi ir skylių lokalizacija yra silpnas.
5. Lėtesnis liuminescencijos gesimas žadinant didelės energijos elektronais nei esant rezonansiniam žadinimui šviesa į  $Ce^{3+}$  jonų lygmenį  $5d_1$  gadolinio turinčiuose granato tipo scintiliatoriuose yra sukeltas sužadavimo pernašos per gadolinio posistemę scintiliatoriaus matricoje.
6. Greta žemiausios energijos gadolinio multipletu  ${}^6P$ , multipletas  ${}^6I$  reikšmingai prisideda prie liuminescencijos gesimo kinetikos palėtėjimo ceriu legiruotuose gadolinio turinčiuose granato

scintiliatoriuose, tokiuose kaip LuGAGG:Ce kristalas, kuris buvo tirtas šioje disertacijoje.

7. Magnio įterpimas į ceriu legiruotus gadolinio turinčius granato tipo scintiliatorius slopina lėtą sužadavimo pernašą per gadolinio posistemę į spinduliuojančius  $Ce^{3+}$  jonus ir dėl to pagreitina scintiliacijų gesimą.
8. Liuminescencijos gesimo pagreitėjimas, kurį sukelia ceriu legiruotų gadolinio turinčių granato scintiliatorių kolegiravimas magniu atsiranda dėl to, kad susidaro plati su Mg susijusi sugerties juosta tame pačiame energijų ruože, kuriame vyksta optiniai šuoliai  ${}^6P \rightarrow {}^8S$  ir  ${}^6I \rightarrow {}^8S$   $Gd^{3+}$  jonuose.
9. Sudėties netvarka GYAGG:Ce granato scintiliatoriaus aliuminio-galio subgardelėle paveikia cerio emisijos juostą ir suskaido ją į du dubletus, kuriuos skiria maždaug 200 meV.
10. Žemos energijos dubletų juosta cerio emisijos spektruose GYAGG granato matricoje yra susijusi su tarpine tetraedrų konfigūracija, kai  $Ga^{3+}$  ir  $Al^{3+}$  jonų turintys tetraedrai turi bendras kraštines  $d_{48}$  su cerio turinčiu dodekaedru; tuo tarpu kai yra bendros kraštinės su dviem tetraedrais, kuriuose yra du  $Ga^{3+}$  jonai, emituojama šviesa didelės energijos dubletų juostoje.

## LIST OF REFERENCES

- [1] M. Nikl and A. Yoshikawa, “Recent R&D Trends in Inorganic Single-Crystal Scintillator Materials for Radiation Detection,” *Adv. Opt. Mater.*, vol. 3, no. 4, pp. 463–481, 2015, doi: 10.1002/adom.201400571.
- [2] V. Retivov *et al.*, “Compositionally Disordered Crystalline Compounds for Next Generation of Radiation Detectors,” *Nanomaterials*, vol. 12, no. 23, Art. no. 23, Jan. 2022, doi: 10.3390/nano12234295.
- [3] J. Ueda and S. Tanabe, “(INVITED) Review of luminescent properties of Ce<sup>3+</sup>-doped garnet phosphors: New insight into the effect of crystal and electronic structure,” *Opt. Mater. X*, vol. 1, p. 100018, Jan. 2019, doi: 10.1016/j.omx.2019.100018.
- [4] S. K. Yadav, B. P. Uberuaga, M. Nikl, C. Jiang, and C. R. Stanek, “Band-Gap and Band-Edge Engineering of Multicomponent Garnet Scintillators from First Principles,” *Phys. Rev. Appl.*, vol. 4, no. 5, p. 054012, Nov. 2015, doi: 10.1103/PhysRevApplied.4.054012.
- [5] G. Tamulaitis *et al.*, “Improvement of the timing properties of Ce-doped oxyorthosilicate LYSO scintillating crystals,” *J. Phys. Chem. Solids*, vol. 139, p. 109356, Apr. 2020, doi: 10.1016/j.jpcs.2020.109356.
- [6] G. Tamulaitis *et al.*, “Improvement of response time in GAGG:Ce scintillation crystals by magnesium codoping,” *J. Appl. Phys.*, vol. 124, no. 21, p. 215907, Dec. 2018, doi: 10.1063/1.5064434.
- [7] C. Weisbuch, “Review—On The Search for Efficient Solid State Light Emitters: Past, Present, Future,” *ECS J. Solid State Sci. Technol.*, vol. 9, no. 1, p. 016022, Dec. 2019, doi: 10.1149/2.0392001JSS.
- [8] A. Khan, K. Balakrishnan, and T. Katona, “Ultraviolet light-emitting diodes based on group three nitrides,” *Nat. Photonics*, vol. 2, no. 2, Art. no. 2, Feb. 2008, doi: 10.1038/nphoton.2007.293.
- [9] M. Kneissl, T.-Y. Seong, J. Han, and H. Amano, “The emergence and prospects of deep-ultraviolet light-emitting diode technologies,” *Nat. Photonics*, vol. 13, no. 4, Art. no. 4, Apr. 2019, doi: 10.1038/s41566-019-0359-9.
- [10] S. Poncé, D. Jena, and F. Giustino, “Hole mobility of strained GaN from first principles,” *Phys. Rev. B*, vol. 100, no. 8, p. 085204, Aug. 2019, doi: 10.1103/PhysRevB.100.085204.
- [11] M. P. Prange, L. W. Campbell, D. Wu, F. Gao, and S. Kerisit, “Calculation of energy relaxation rates of fast particles by phonons in crystals,” *Phys. Rev. B*, vol. 91, no. 10, p. 104305, Mar. 2015, doi: 10.1103/PhysRevB.91.104305.
- [12] E. Bellotti, F. Bertazzi, and M. Goano, “Alloy scattering in AlGaIn and InGaIn: A numerical study,” *J. Appl. Phys.*, vol. 101, no. 12, p. 123706, Jun. 2007, doi: 10.1063/1.2748353.

- [13] A. Belsky, A. Gektin, and A. N. Vasil'ev, "Influence of Disorder in Scintillating Solid Solutions on Thermalization and Recombination of Electronic Excitations," *Phys. Status Solidi B*, vol. 257, no. 8, p. 1900535, 2020, doi: 10.1002/pssb.201900535.
- [14] F. Yonezawa and K. Morigaki, "Coherent Potential Approximation. Basic concepts and applications," *Prog. Theor. Phys. Suppl.*, vol. 53, pp. 1–76, Jan. 1973, doi: 10.1143/PTPS.53.1.
- [15] M. Filoche and S. Mayboroda, "Universal mechanism for Anderson and weak localization," *Proc. Natl. Acad. Sci.*, vol. 109, no. 37, pp. 14761–14766, Sep. 2012, doi: 10.1073/pnas.1120432109.
- [16] L. Bellaiche and D. Vanderbilt, "Virtual crystal approximation revisited: Application to dielectric and piezoelectric properties of perovskites," *Phys. Rev. B*, vol. 61, no. 12, pp. 7877–7882, Mar. 2000, doi: 10.1103/PhysRevB.61.7877.
- [17] R. J. Moon, "Inorganic Crystals for the Detection of High Energy Particles and Quanta," *Phys. Rev.*, vol. 73, no. 10, pp. 1210–1210, May 1948, doi: 10.1103/PhysRev.73.1210.
- [18] H. Kallmann, "Quantitative Measurements with Scintillation Counters," *Phys. Rev.*, vol. 75, no. 4, pp. 623–626, Feb. 1949, doi: 10.1103/PhysRev.75.623.
- [19] P. R. Bell, "The Use of Anthracene as a Scintillation Counter," *Phys. Rev.*, vol. 73, no. 11, pp. 1405–1406, Jun. 1948, doi: 10.1103/PhysRev.73.1405.2.
- [20] H. Kallmann, "Scintillation Counting with Solutions," *Phys. Rev.*, vol. 78, no. 5, pp. 621–622, Jun. 1950, doi: 10.1103/PhysRev.78.621.2.
- [21] H. Kallmann and M. Furst, "Fluorescence of Solutions Bombarded with High Energy Radiation (Energy Transport in Liquids)," *Phys. Rev.*, vol. 79, no. 5, pp. 857–870, Sep. 1950, doi: 10.1103/PhysRev.79.857.
- [22] H. Kallmann and M. Furst, "Fluorescence of Solutions Bombarded with High Energy Radiation (Energy Transport in Liquids) Part II," *Phys. Rev.*, vol. 81, no. 5, pp. 853–864, Mar. 1951, doi: 10.1103/PhysRev.81.853.
- [23] M. Furst and H. Kallman, "High Energy Induced Fluorescence in Organic Liquid Solutions (Energy Transport in Liquids). III," *Phys. Rev.*, vol. 85, no. 5, pp. 816–825, Mar. 1952, doi: 10.1103/PhysRev.85.816.
- [24] G. T. Reynolds, "Scintillation counting," *Nucleonics*, vol. 6, pp. 488–489, 1950.
- [25] R. K. Swank, "Recent advances in theory of scintillation phosphors," *Nucleonics*, vol. 12, pp. 4–22, 1954.
- [26] F. Santanastasio, "Precision Timing in the CMS MTD Barrel Timing Layer With Crystal Bars and SiPMs," *IEEE Trans. Nucl. Sci.*, vol. 67, no. 9, pp. 2105–2110, Sep. 2020, doi: 10.1109/TNS.2020.3009251.



- [27] P. Lecoq, “Development of new scintillators for medical applications,” *Nucl. Instrum. Methods Phys. Res. Sect. Accel. Spectrometers Detect. Assoc. Equip.*, vol. 809, pp. 130–139, Feb. 2016, doi: 10.1016/j.nima.2015.08.041.
- [28] M. Korjik and E. Auffray, “Limits of Inorganic Scintillating Materials to Operate in a High Dose Rate Environment at Future Collider Experiments,” *IEEE Trans. Nucl. Sci.*, vol. 63, no. 2, pp. 552–563, Apr. 2016, doi: 10.1109/TNS.2016.2527701.
- [29] B. Fleming *et al.*, “Basic Research Needs for High Energy Physics Detector Research & Development: Report of the Office of Science Workshop on Basic Research Needs for HEP Detector Research and Development: December 11-14, 2019,” USDOE Office of Science (SC) (United States), Dec. 2019. doi: 10.2172/1659761.
- [30] X. Yu *et al.*, “Requirements of Scintillation Crystals with the Development of PET Scanners,” *Crystals*, vol. 12, no. 9, Art. no. 9, Sep. 2022, doi: 10.3390/cryst12091302.
- [31] *Technical proposal*. in LHC technical proposal. Geneva: CERN, 1994. Accessed: Aug. 29, 2023. [Online]. Available: <https://cds.cern.ch/record/290969>
- [32] “ALICE: Technical proposal for a Large Ion collider Experiment at the CERN LHC.” in LHC technical proposal. CERN, Geneva, 1995. Accessed: Aug. 29, 2023. [Online]. Available: <https://cds.cern.ch/record/293391>
- [33] V. G. Baryshevsky *et al.*, “Single crystals of tungsten compounds as promising materials for the total absorption detectors of the e.m. calorimeters,” *Nucl. Instrum. Methods Phys. Res. Sect. Accel. Spectrometers Detect. Assoc. Equip.*, vol. 322, no. 2, pp. 231–234, Nov. 1992, doi: 10.1016/0168-9002(92)90033-Z.
- [34] M. Kobayashi, M. Ishii, Y. Usuki, and H. Yahagi, “Scintillation characteristics of PbWO<sub>4</sub> single crystals at room temperature,” *Nucl. Instrum. Methods Phys. Res. Sect. Accel. Spectrometers Detect. Assoc. Equip.*, vol. 333, no. 2, pp. 429–433, Sep. 1993, doi: 10.1016/0168-9002(93)91187-R.
- [35] P. Lecoq *et al.*, “Lead tungstate (PbWO<sub>4</sub>) scintillators for LHC EM calorimetry,” *Nucl. Instrum. Methods Phys. Res. Sect. Accel. Spectrometers Detect. Assoc. Equip.*, vol. 365, no. 2, pp. 291–298, Nov. 1995, doi: 10.1016/0168-9002(95)00589-7.
- [36] R. Y. Zhu *et al.*, “A study on the properties of lead tungstate crystals,” *Nucl. Instrum. Methods Phys. Res. Sect. Accel. Spectrometers Detect. Assoc. Equip.*, vol. 376, no. 3, pp. 319–334, Jul. 1996, doi: 10.1016/0168-9002(96)00286-0.
- [37] A. A. Annenkov, M. V. Korzhik, and P. Lecoq, “Lead tungstate scintillation material,” *Nucl. Instrum. Methods Phys. Res. Sect. Accel. Spectrometers Detect. Assoc. Equip.*, vol. 490, no. 1, pp. 30–50, Sep. 2002, doi: 10.1016/S0168-9002(02)00916-6.

- [38] M. Follin, V. Sharyy, J.-P. Bard, M. Korzhik, and D. Yvon, “Scintillating properties of today available lead tungstate crystals,” *J. Instrum.*, vol. 16, no. 08, p. P08040, Aug. 2021, doi: 10.1088/1748-0221/16/08/P08040.
- [39] Yu. D. Prokoshkin and A. V. Shtannikov, “Energy resolution calculation of the PWO calorimeter, comparison with the beam tests,” *Nucl. Instrum. Methods Phys. Res. Sect. Accel. Spectrometers Detect. Assoc. Equip.*, vol. 362, no. 2, pp. 406–409, Aug. 1995, doi: 10.1016/0168-9002(95)00226-X.
- [40] R. W. Novotny *et al.*, “High resolution calorimetry with PWO-II,” in *IEEE Nuclear Science Symposium Conference Record, 2005*, Oct. 2005, pp. 244–248. doi: 10.1109/NSSMIC.2005.1596246.
- [41] M. Moszyński, W. Czarnacki, W. Klamra, M. Szawłowski, P. Schotanus, and M. Kapusta, “Application of large area avalanche photodiodes to study scintillators at liquid nitrogen temperatures,” *Nucl. Instrum. Methods Phys. Res. Sect. Accel. Spectrometers Detect. Assoc. Equip.*, vol. 504, no. 1, pp. 307–312, May 2003, doi: 10.1016/S0168-9002(03)00785-X.
- [42] M. Moszynski, M. Kapusta, M. Mayhugh, D. Wolski, and S. O. Flyckt, “Absolute light output of scintillators,” *IEEE Trans. Nucl. Sci.*, vol. 44, no. 3, pp. 1052–1061, Jun. 1997, doi: 10.1109/23.603803.
- [43] I. Holl, E. Lorenz, and G. Mageras, “A measurement of the light yield of common inorganic scintillators,” *IEEE Trans. Nucl. Sci.*, vol. 35, no. 1, pp. 105–109, Feb. 1988, doi: 10.1109/23.12684.
- [44] V. Vaněček, K. Děcká, E. Mihóková, V. Čuba, R. Král, and M. Nikl, “Advanced Halide Scintillators: From the Bulk to Nano,” *Adv. Photonics Res.*, vol. 3, no. 8, p. 2200011, 2022, doi: 10.1002/adpr.202200011.
- [45] S. Gridin, A. Belsky, M. Moszynski, A. Syntfeld-Kazuch, N. Shiran, and A. Gektin, “Scintillation properties of CsI:In single crystals,” *Nucl. Instrum. Methods Phys. Res. Sect. Accel. Spectrometers Detect. Assoc. Equip.*, vol. 761, pp. 13–18, Oct. 2014, doi: 10.1016/j.nima.2014.05.111.
- [46] S. Kerisit, Z. Wang, R. T. Williams, J. Q. Grim, and F. Gao, “Kinetic Monte Carlo Simulations of Scintillation Processes in NaI(Tl),” *IEEE Trans. Nucl. Sci.*, vol. 61, no. 2, pp. 860–869, Apr. 2014, doi: 10.1109/TNS.2014.2300142.
- [47] E. Auffray *et al.*, “Irradiation effects on Gd<sub>3</sub>Al<sub>2</sub>Ga<sub>3</sub>O<sub>12</sub> scintillators prospective for application in harsh irradiation environments,” *Radiat. Phys. Chem.*, vol. 164, p. 108365, Nov. 2019, doi: 10.1016/j.radphyschem.2019.108365.
- [48] R. Mao, L. Zhang, and R.-Y. Zhu, “LSO/LYSO Crystals for Future HEP Experiments,” *J. Phys. Conf. Ser.*, vol. 293, no. 1, p. 012004, Apr. 2011, doi: 10.1088/1742-6596/293/1/012004.

- [49] K. Kamada *et al.*, “Cz grown 2-in. size Ce:Gd<sub>3</sub>(Al,Ga)<sub>5</sub>O<sub>12</sub> single crystal; relationship between Al, Ga site occupancy and scintillation properties,” *Opt. Mater.*, vol. 36, no. 12, pp. 1942–1945, Oct. 2014, doi: 10.1016/j.optmat.2014.04.001.
- [50] K. Kamada *et al.*, “Scintillator-oriented combinatorial search in Ce-doped (Y,Gd)<sub>3</sub>(Ga,Al)<sub>5</sub>O<sub>12</sub> multicomponent garnet compounds,” *J. Phys. Appl. Phys.*, vol. 44, no. 50, p. 505104, Dec. 2011, doi: 10.1088/0022-3727/44/50/505104.
- [51] K. Kamada *et al.*, “Growth of 2-inch size Ce:doped Lu<sub>2</sub>Gd<sub>1</sub>Al<sub>2</sub>Ga<sub>3</sub>O<sub>12</sub> single crystal by the Czochralski method and their scintillation properties,” *J. Cryst. Growth*, vol. 410, pp. 14–17, Jan. 2015, doi: 10.1016/j.jcrysgro.2014.10.004.
- [52] W. Chewpraditkul *et al.*, “Optical and scintillation properties of LuGd<sub>2</sub>Al<sub>2</sub>Ga<sub>3</sub>O<sub>12</sub>:Ce, Lu<sub>2</sub>GdAl<sub>2</sub>Ga<sub>3</sub>O<sub>12</sub>:Ce, and Lu<sub>2</sub>YAl<sub>2</sub>Ga<sub>3</sub>O<sub>12</sub>:Ce single crystals: A comparative study,” *Nucl. Instrum. Methods Phys. Res. Sect. Accel. Spectrometers Detect. Assoc. Equip.*, vol. 1004, p. 165381, Jul. 2021, doi: 10.1016/j.nima.2021.165381.
- [53] M. Korzhik *et al.*, “Role of the Dilution of the Gd Sublattice in Forming the Scintillation Properties of Quaternary (Gd,Lu)<sub>3</sub>Al<sub>2</sub>Ga<sub>3</sub>O<sub>12</sub>: Ce Ceramics,” *Crystals*, vol. 12, no. 9, Art. no. 9, Sep. 2022, doi: 10.3390/cryst12091196.
- [54] S. Gundacker, E. Auffray, K. Pauwels, and P. Lecoq, “Measurement of intrinsic rise times for various L(Y)SO and LuAG scintillators with a general study of prompt photons to achieve 10 ps in TOF-PET,” *Phys. Med. Biol.*, vol. 61, no. 7, p. 2802, Mar. 2016, doi: 10.1088/0031-9155/61/7/2802.
- [55] G. Tamulaitis *et al.*, “Improvement of the Time Resolution of Radiation Detectors Based on Gd<sub>3</sub>Al<sub>2</sub>Ga<sub>3</sub>O<sub>12</sub> Scintillators With SiPM Readout,” *IEEE Trans. Nucl. Sci.*, vol. 66, no. 7, pp. 1879–1888, Jul. 2019, doi: 10.1109/TNS.2019.2919898.
- [56] S. Nargelas, M. Korjik, M. Vengris, and G. Tamulaitis, “Study of electronic excitation relaxation at cerium ions in Gd<sub>3</sub>Al<sub>2</sub>Ga<sub>3</sub>O<sub>12</sub> matrix using multipulse transient absorption technique,” *J. Appl. Phys.*, vol. 128, no. 10, p. 103104, Sep. 2020, doi: 10.1063/5.0015141.
- [57] M. S. Alekhin *et al.*, “Improvement of  $\gamma$ -ray energy resolution of LaBr<sub>3</sub>:Ce<sup>3+</sup> scintillation detectors by Sr<sup>2+</sup> and Ca<sup>2+</sup> co-doping,” *Appl. Phys. Lett.*, vol. 102, no. 16, p. 161915, Apr. 2013, doi: 10.1063/1.4803440.
- [58] K. Yang and P. R. Menge, “Improving  $\gamma$ -ray energy resolution, non-proportionality, and decay time of NaI:Tl<sup>+</sup> with Sr<sup>2+</sup> and Ca<sup>2+</sup> co-doping,” *J. Appl. Phys.*, vol. 118, no. 21, p. 213106, Dec. 2015, doi: 10.1063/1.4937126.
- [59] I. V. Khodyuk, S. A. Messina, T. J. Hayden, E. D. Bourret, and G. A. Bizarri, “Optimization of scintillation performance via a combinatorial

- multi-element co-doping strategy: Application to NaI:Tl,” *J. Appl. Phys.*, vol. 118, no. 8, p. 084901, Aug. 2015, doi: 10.1063/1.4928771.
- [60] C. Brecher *et al.*, “Suppression of afterglow in CsI:Tl by codoping with  $\text{Eu}^{2+}$ —I: Experimental,” *Nucl. Instrum. Methods Phys. Res. Sect. Accel. Spectrometers Detect. Assoc. Equip.*, vol. 558, no. 2, pp. 450–457, Mar. 2006, doi: 10.1016/j.nima.2005.11.119.
- [61] R. W. Novotny *et al.*, “The PANDA Electromagnetic Calorimeter—A High-Resolution Detector Based on PWO-II,” *IEEE Trans. Nucl. Sci.*, vol. 57, no. 3, pp. 1441–1446, Jun. 2010, doi: 10.1109/TNS.2009.2033913.
- [62] V. Babin, P. Herman, M. Kucera, M. Nikl, and S. Zazubovich, “Effect of  $\text{Mg}^{2+}$  co-doping on the photo- and thermally stimulated luminescence of the  $(\text{Lu,Gd})_3(\text{Ga,Al})_5\text{O}_{12}:\text{Ce}$  epitaxial films,” *J. Lumin.*, vol. 215, p. 116608, Nov. 2019, doi: 10.1016/j.jlumin.2019.116608.
- [63] S. Nargelas *et al.*, “Influence of heavy magnesium codoping on emission decay in Ce-doped multicomponent garnet scintillators,” *J. Mater. Chem. C*, vol. 11, no. 35, pp. 12007–12015, 2023, doi: 10.1039/D3TC02247A.
- [64] S. Gundacker *et al.*, “Time of flight positron emission tomography towards 100ps resolution with L(Y)SO: an experimental and theoretical analysis,” *J. Instrum.*, vol. 8, no. 07, p. P07014, Jul. 2013, doi: 10.1088/1748-0221/8/07/P07014.
- [65] S. Gundacker, “Time resolution in scintillator based detectors for positron emission tomography,” Thesis, Technische Universität Wien, 2014. doi: 10.34726/hss.2014.21431.
- [66] M. Korzhik, G. Tamulaitis, and A. N. Vasil’ev, *Physics of Fast Processes in Scintillators*. in Particle Acceleration and Detection. Cham: Springer International Publishing, 2020. doi: 10.1007/978-3-030-21966-6.
- [67] C. Weisbuch, S. Nakamura, Y.-R. Wu, and J. S. Speck, “Disorder effects in nitride semiconductors: impact on fundamental and device properties,” *Nanophotonics*, vol. 10, no. 1, pp. 3–21, Jan. 2021, doi: 10.1515/nanoph-2020-0590.
- [68] A. Rubio, J. L. Corkill, M. L. Cohen, E. L. Shirley, and S. G. Louie, “Quasiparticle band structure of AlN and GaN,” *Phys. Rev. B*, vol. 48, no. 16, pp. 11810–11816, Oct. 1993, doi: 10.1103/PhysRevB.48.11810.
- [69] J. Wu *et al.*, “Temperature dependence of the fundamental band gap of InN,” *J. Appl. Phys.*, vol. 94, no. 7, pp. 4457–4460, Sep. 2003, doi: 10.1063/1.1605815.
- [70] R. Finn and S. Schulz, “Impact of random alloy fluctuations on the electronic and optical properties of  $(\text{Al,Ga})\text{N}$  quantum wells: Insights from tight-binding calculations,” *J. Chem. Phys.*, vol. 157, no. 24, p. 244705, Dec. 2022, doi: 10.1063/5.0132490.

- [71] E. Kuokstis, W. H. Sun, M. Shatalov, J. W. Yang, and M. Asif Khan, "Role of alloy fluctuations in photoluminescence dynamics of AlGa<sub>N</sub> epilayers," *Appl. Phys. Lett.*, vol. 88, no. 26, p. 261905, Jun. 2006, doi: 10.1063/1.2218275.
- [72] Y.-R. Wu, R. Shivaraman, K.-C. Wang, and J. S. Speck, "Analyzing the physical properties of InGa<sub>N</sub> multiple quantum well light emitting diodes from nano scale structure," *Appl. Phys. Lett.*, vol. 101, no. 8, p. 083505, Aug. 2012, doi: 10.1063/1.4747532.
- [73] M. Piccardo *et al.*, "Localization landscape theory of disorder in semiconductors. II. Urbach tails of disordered quantum well layers," *Phys. Rev. B*, vol. 95, no. 14, p. 144205, Apr. 2017, doi: 10.1103/PhysRevB.95.144205.
- [74] C.-K. Li *et al.*, "Localization landscape theory of disorder in semiconductors. III. Application to carrier transport and recombination in light emitting diodes," *Phys. Rev. B*, vol. 95, no. 14, p. 144206, Apr. 2017, doi: 10.1103/PhysRevB.95.144206.
- [75] S. F. Chichibu *et al.*, "Origin of defect-insensitive emission probability in In-containing (Al,In,Ga)<sub>N</sub> alloy semiconductors," *Nat. Mater.*, vol. 5, no. 10, Art. no. 10, Oct. 2006, doi: 10.1038/nmat1726.
- [76] C. A. Hurni *et al.*, "Bulk Ga<sub>N</sub> flip-chip violet light-emitting diodes with optimized efficiency for high-power operation," *Appl. Phys. Lett.*, vol. 106, no. 3, p. 031101, Jan. 2015, doi: 10.1063/1.4905873.
- [77] G. F. Knoll, *Radiation Detection and Measurement*. in John Wiley & Sons, 2000.
- [78] P. Lecoq, A. Gektin, and M. Korzhik, *Inorganic Scintillators for Detector Systems*. in Particle Acceleration and Detection. Cham: Springer International Publishing, 2017. doi: 10.1007/978-3-319-45522-8.
- [79] A. Gektin, A. N. Vasil'ev, V. Suzdal, and A. Sobolev, "Energy Resolution of Scintillators in Connection With Track Structure," *IEEE Trans. Nucl. Sci.*, vol. 67, no. 6, pp. 880–887, Jun. 2020, doi: 10.1109/TNS.2020.2978236.
- [80] A. N. Vasil'ev and A. V. Gektin, "Multiscale Approach to Estimation of Scintillation Characteristics," *IEEE Trans. Nucl. Sci.*, vol. 61, no. 1, pp. 235–245, Feb. 2014, doi: 10.1109/TNS.2013.2282117.
- [81] M. P. Prange, Y. Xie, L. W. Campbell, F. Gao, and S. Kerisit, "Monte Carlo simulation of electron thermalization in scintillator materials: Implications for scintillator nonproportionality," *J. Appl. Phys.*, vol. 122, no. 23, p. 234504, Dec. 2017, doi: 10.1063/1.4998966.
- [82] Z. Wang, Y. Xie, L. W. Campbell, F. Gao, and S. Kerisit, "Monte Carlo simulations of electron thermalization in alkali iodide and alkaline-earth fluoride scintillators," *J. Appl. Phys.*, vol. 112, no. 1, p. 014906, Jul. 2012, doi: 10.1063/1.4736088.

- [83] A. Gektin and A. Vasil'ev, "Scintillator energy resolution and a way to improve it by kinetic waveform analysis," *Radiat. Meas.*, vol. 122, pp. 108–114, Mar. 2019, doi: 10.1016/j.radmeas.2019.02.004.
- [84] S. Gridin, A. Belsky, C. Dujardin, A. Gektin, N. Shiran, and A. Vasil'ev, "Kinetic Model of Energy Relaxation in CsI:A (A = Tl and In) Scintillators," *J. Phys. Chem. C*, vol. 119, no. 35, pp. 20578–20590, Sep. 2015, doi: 10.1021/acs.jpcc.5b05627.
- [85] Z. Wang, Y. Xie, B. D. Cannon, L. W. Campbell, F. Gao, and S. Kerisit, "Computer simulation of electron thermalization in CsI and CsI(Tl)," *J. Appl. Phys.*, vol. 110, no. 6, p. 064903, Sep. 2011, doi: 10.1063/1.3632969.
- [86] A. N. Vasil'ev, "Microtheory of Scintillation in Crystalline Materials," in *Engineering of Scintillation Materials and Radiation Technologies*, M. Korzhik and A. Gektin, Eds., in Springer Proceedings in Physics. Cham: Springer International Publishing, 2017, pp. 3–34. doi: 10.1007/978-3-319-68465-9\_1.
- [87] O. Motornyi, N. Vast, I. Timrov, O. Baseggio, S. Baroni, and A. D. Corso, "Electron energy loss spectroscopy of bulk gold with ultrasoft pseudopotentials and the Liouville-Lanczos method," *Phys. Rev. B*, vol. 102, no. 3, p. 035156, Jul. 2020, doi: 10.1103/PhysRevB.102.035156.
- [88] S. T. Perkins and D. E. Cullen, "ENDL Type Formats for the LLNL Evaluated Atomic Data Library (EADL), Evaluated Electron Data Library (EEDL), and Evaluated Photon Data Library (EPDL)," Lawrence Livermore National Lab. (LLNL), Livermore, CA (United States), UCRL-ID-117796-REV-1, May 2002. doi: 10.2172/15013373.
- [89] R. Klucker and U. Nielsen, "Kramers-Kronig analysis of reflection data," *Comput. Phys. Commun.*, vol. 6, no. 4, pp. 187–193, Oct. 1973, doi: 10.1016/0010-4655(73)90099-4.
- [90] S. Agostinelli *et al.*, "Geant4—a simulation toolkit," *Nucl. Instrum. Methods Phys. Res. Sect. Accel. Spectrometers Detect. Assoc. Equip.*, vol. 506, no. 3, pp. 250–303, Jul. 2003, doi: 10.1016/S0168-9002(03)01368-8.
- [91] M. P. Prange, L. W. Campbell, and S. Kerisit, "Electron-phonon scattering rates in complex polar crystals," *Phys. Rev. B*, vol. 96, no. 10, p. 104307, Sep. 2017, doi: 10.1103/PhysRevB.96.104307.
- [92] R. Kirkin, V. V. Mikhailin, and A. N. Vasil'ev, "Recombination of Correlated Electron–Hole Pairs With Account of Hot Capture With Emission of Optical Phonons," *IEEE Trans. Nucl. Sci.*, vol. 59, no. 5, pp. 2057–2064, Oct. 2012, doi: 10.1109/TNS.2012.2194306.
- [93] J. Llacer and E. L. Garwin, "Electron-Phonon Interaction in Alkali Halides. I. The Transport of Secondary Electrons with Energies between 0.25 and 7.5 eV," *J. Appl. Phys.*, vol. 40, no. 7, pp. 2766–2775, Jun. 1969, doi: 10.1063/1.1658075.

- [94] K. S. Song and R. T. Williams, *Self-Trapped Excitons*. in Springer Series in Solid-State Sciences, 1996. doi: 10.1007/978-3-642-85236-7
- [95] M. Inokuti and F. Hirayama, “Influence of Energy Transfer by the Exchange Mechanism on Donor Luminescence,” *J. Chem. Phys.*, vol. 43, no. 6, pp. 1978–1989, May 1965, doi: 10.1063/1.1697063.
- [96] M. Yokota and O. Tanimoto, “Effects of Diffusion on Energy Transfer by Resonance,” *J. Phys. Soc. Jpn.*, vol. 22, no. 3, pp. 779–784, Mar. 1967, doi: 10.1143/JPSJ.22.779.
- [97] Z. Onderisinova, M. Kucera, M. Hanus, and M. Nikl, “Temperature-dependent nonradiative energy transfer from  $Gd^{3+}$  to  $Ce^{3+}$  ions in co-doped LuAG:Ce,Gd garnet scintillators,” *J. Lumin.*, vol. 167, pp. 106–113, Nov. 2015, doi: 10.1016/j.jlumin.2015.06.014.
- [98] A. A. Setlur, J. J. Shiang, and C. J. Vess, “Transition from Long-Range to Short-Range Energy Transfer through Donor Migration in Garnet Hosts,” *J. Phys. Chem. C*, vol. 115, no. 8, pp. 3475–3480, Mar. 2011, doi: 10.1021/jp110520j.
- [99] M. Kirm *et al.*, “Exciton-exciton interactions in  $CdWO_4$  irradiated by intense femtosecond vacuum ultraviolet pulses,” *Phys. Rev. B*, vol. 79, no. 23, p. 233103, Jun. 2009, doi: 10.1103/PhysRevB.79.233103.
- [100] D. Spassky *et al.*, “Excitation density effects in luminescence properties of  $CaMoO_4$  and  $ZnMoO_4$ ,” *Opt. Mater.*, vol. 90, pp. 7–13, Apr. 2019, doi: 10.1016/j.optmat.2019.02.011.
- [101] J. Cho, E. F. Schubert, and J. K. Kim, “Efficiency droop in light-emitting diodes: Challenges and countermeasures,” *Laser Photonics Rev.*, vol. 7, no. 3, pp. 408–421, 2013, doi: 10.1002/lpor.201200025.
- [102] Y. C. Shen, G. O. Mueller, S. Watanabe, N. F. Gardner, A. Munkholm, and M. R. Krames, “Auger recombination in InGaN measured by photoluminescence,” *Appl. Phys. Lett.*, vol. 91, no. 14, p. 141101, Oct. 2007, doi: 10.1063/1.2785135.
- [103] T. Mukai, M. Yamada, and S. Nakamura, “Characteristics of InGaN-Based UV/Blue/Green/Amber/Red Light-Emitting Diodes,” *Jpn. J. Appl. Phys.*, vol. 38, no. 7R, p. 3976, Jul. 1999, doi: 10.1143/JJAP.38.3976.
- [104] J. Iveland, L. Martinelli, J. Peretti, J. S. Speck, and C. Weisbuch, “Direct Measurement of Auger Electrons Emitted from a Semiconductor Light-Emitting Diode under Electrical Injection: Identification of the Dominant Mechanism for Efficiency Droop,” *Phys. Rev. Lett.*, vol. 110, no. 17, p. 177406, Apr. 2013, doi: 10.1103/PhysRevLett.110.177406.
- [105] A. C. Espenlaub, D. J. Myers, E. C. Young, S. Marcinkevičius, C. Weisbuch, and J. S. Speck, “Evidence of trap-assisted Auger recombination in low radiative efficiency MBE-grown III-nitride LEDs,” *J. Appl. Phys.*, vol. 126, no. 18, p. 184502, Nov. 2019, doi: 10.1063/1.5096773.

- [106] K. Nomeika, Ž. Podlipskas, M. Nikitina, S. Nargelas, G. Tamulaitis, and R. Aleksiejūnas, “Impact of carrier diffusion on the internal quantum efficiency of InGaN quantum well structures,” *J. Mater. Chem. C*, vol. 10, no. 5, pp. 1735–1745, Feb. 2022, doi: 10.1039/D1TC04760D.
- [107] S. D. Baranovskii, R. Eichmann, and P. Thomas, “Temperature-dependent exciton luminescence in quantum wells by computer simulation,” *Phys. Rev. B*, vol. 58, no. 19, pp. 13081–13087, Nov. 1998, doi: 10.1103/PhysRevB.58.13081.
- [108] O. Kravcov, J. Mickevičius, and G. Tamulaitis, “Kinetic Monte Carlo simulations of the dynamics of a coupled system of free and localized carriers in AlGaIn,” *J. Phys. Condens. Matter*, vol. 32, no. 14, p. 145901, Jan. 2020, doi: 10.1088/1361-648X/ab61cb.
- [109] P. Sohi, J.-F. Carlin, and N. Grandjean, “Alloy disorder limited mobility of InGaIn two-dimensional electron gas,” *Appl. Phys. Lett.*, vol. 112, no. 26, p. 262101, Jun. 2018, doi: 10.1063/1.5030992.
- [110] B. I. Shklovskii and A. L. Efros, *Electronic Properties of Doped Semiconductors*, vol. 45. in Springer Series in Solid-State Sciences, vol. 45. Berlin, Heidelberg: Springer, 1984. doi: 10.1007/978-3-662-02403-4.
- [111] M. Filoche, M. Piccardo, Y.-R. Wu, C.-K. Li, C. Weisbuch, and S. Mayboroda, “Localization landscape theory of disorder in semiconductors. I. Theory and modeling,” *Phys. Rev. B*, vol. 95, no. 14, p. 144204, Apr. 2017, doi: 10.1103/PhysRevB.95.144204.
- [112] F. Gebhard, A. V. Nenashev, K. Meerholz, and S. D. Baranovskii, “Quantum states in disordered media. I. Low-pass filter approach,” *Phys. Rev. B*, vol. 107, no. 6, p. 064206, Feb. 2023, doi: 10.1103/PhysRevB.107.064206.
- [113] A. V. Nenashev, S. D. Baranovskii, K. Meerholz, and F. Gebhard, “Quantum states in disordered media. II. Spatial charge carrier distribution,” *Phys. Rev. B*, vol. 107, no. 6, p. 064207, Feb. 2023, doi: 10.1103/PhysRevB.107.064207.
- [114] H.-T. Shen, C. Weisbuch, J. S. Speck, and Y.-R. Wu, “Three-Dimensional Modeling of Minority-Carrier Lateral Diffusion Length Including Random Alloy Fluctuations in InGaIn and AlGaIn Single Quantum Wells,” *Phys. Rev. Appl.*, vol. 16, no. 2, p. 024054, Aug. 2021, doi: 10.1103/PhysRevApplied.16.024054.
- [115] S.-H. Wei, L. G. Ferreira, J. E. Bernard, and A. Zunger, “Electronic properties of random alloys: Special quasirandom structures,” *Phys. Rev. B*, vol. 42, no. 15, pp. 9622–9649, Nov. 1990, doi: 10.1103/PhysRevB.42.9622.
- [116] Y. A. Mastrikov, R. Merkle, E. Heifets, E. A. Kotomin, and J. Maier, “Pathways for oxygen incorporation in mixed conducting perovskites: A DFT-based Mechanistic analysis for (La, Sr)MnO<sub>3-δ</sub>,” *J. Phys. Chem. C*, vol. 114, no. 7, 2010, doi: 10.1021/jp909401g.



- [117] A. Weizman, D. Fuks, E. A. Kotomin, and D. Gryaznov, “Ab initio study of phase competition in  $(\text{La}_{1-c}, \text{Sr}_c)\text{CoO}_3$  solid solutions,” *Solid State Ion.*, vol. 230, pp. 32–36, Jan. 2013, doi: 10.1016/j.ssi.2012.09.007.
- [118] L. Qin, H. Li, S. Lu, D. Ding, and G. Ren, “Growth and characteristics of LYSO ( $\text{Lu}_{2(1-x-y)}\text{Y}_{2x}\text{SiO}_5:\text{Ce}_y$ ) scintillation crystals,” *J. Cryst. Growth*, vol. 281, no. 2, pp. 518–524, Aug. 2005, doi: 10.1016/j.jcrysgro.2005.04.057.
- [119] D. Ding, L. Weng, J. Yang, G. Ren, and Y. Wu, “Influence of yttrium content on the location of rare earth ions in LYSO:Ce crystals,” *J. Solid State Chem.*, vol. 209, pp. 56–62, Jan. 2014, doi: 10.1016/j.jssc.2013.10.018.
- [120] R. D. Shannon, “Revised effective ionic radii and systematic studies of interatomic distances in halides and chalcogenides,” *Acta Crystallogr. A*, vol. 32, no. 5, Art. no. 5, Sep. 1976, doi: 10.1107/S0567739476001551.
- [121] K. A. Persson et al., “Materials Data on  $\text{Lu}_2\text{SiO}_5$  (Mp-16969) by Materials Project,” <https://next-gen.materialsproject.org/materials/mp-16969/> (accessed Sep. 25, 2023).
- [122] K. A. Persson et al., “Materials Data on  $\text{Y}_2\text{SiO}_5$  (Mp-3520) by Materials Project,” <https://next-gen.materialsproject.org/materials/mp-3520/> (accessed Sep. 25, 2023).
- [123] J. R. Cárdenas, “Effective passivant pseudopotentials for semiconductors: Beyond the spherical approximation,” *Superlattices Microstruct.*, vol. 100, pp. 548–559, Dec. 2016, doi: 10.1016/j.spmi.2016.10.009.
- [124] P. Giannozzi et al., “Advanced capabilities for materials modelling with Quantum ESPRESSO,” *J. Phys. Condens. Matter*, vol. 29, no. 46, p. 465901, Oct. 2017, doi: 10.1088/1361-648X/aa8f79.
- [125] J. Heyd, G. E. Scuseria, and M. Ernzerhof, “Hybrid functionals based on a screened Coulomb potential,” *J. Chem. Phys.*, vol. 118, no. 18, pp. 8207–8215, Apr. 2003, doi: 10.1063/1.1564060.
- [126] L. Chen et al., “Role of Yttrium in Thermoluminescence of LYSO:Ce Crystals,” *J. Phys. Chem. C*, vol. 124, no. 32, pp. 17726–17732, Aug. 2020, doi: 10.1021/acs.jpcc.0c03370.
- [127] H. Huang, Q. Li, X. Lu, Y. Qian, Y. Wu, and R. T. Williams, “Role of hot electron transport in scintillators: A theoretical study,” *Phys. Status Solidi RRL – Rapid Res. Lett.*, vol. 10, no. 10, pp. 762–768, 2016, doi: 10.1002/pssr.201600276.
- [128] Z. Tian, L. Sun, J. Wang, and J. Wang, “Theoretical prediction and experimental determination of the low lattice thermal conductivity of  $\text{Lu}_2\text{SiO}_5$ ,” *J. Eur. Ceram. Soc.*, vol. 35, no. 6, pp. 1923–1932, Jun. 2015, doi: 10.1016/j.jeurceramsoc.2015.01.001.
- [129] P. Sohi, D. Martin, and N. Grandjean, “Critical thickness of GaN on AlN: impact of growth temperature and dislocation density,”

- Semicond. Sci. Technol.*, vol. 32, no. 7, p. 075010, Jun. 2017, doi: 10.1088/1361-6641/aa7248.
- [130] H. J. Eichler, P. Günter, and D. W. Pohl, *Laser-Induced Dynamic Gratings*, vol. 50. in Springer Series in Optical Sciences, vol. 50. Berlin, Heidelberg: Springer, 1986. doi: 10.1007/978-3-540-39662-8.
- [131] R. Aleksiejūnas *et al.*, “Impact of Alloy-Disorder-Induced Localization on Hole Diffusion in Highly Excited c-Plane and m-Plane InGaN Quantum Wells,” *Phys. Rev. Appl.*, vol. 14, no. 5, p. 054043, Nov. 2020, doi: 10.1103/PhysRevApplied.14.054043.
- [132] K.A. Persson *et al.*, "Materials Data on GaN (Mp-804) by Materials Project," <https://materialsproject.org/materials/mp-804/> (accessed Dec. 15, 2022).
- [133] K.A. Persson *et al.*, "Materials Data on AlN (Mp-661) by Materials Project," <https://materialsproject.org/materials/mp-661> (accessed Dec. 15, 2022).
- [134] C. G. Rodrigues and R. Luzzi, “Nonlinear charge transport in highly polar semiconductors: GaN, AlN, InN and GaAs,” *Pramana*, vol. 95, no. 1, p. 44, Mar. 2021, doi: 10.1007/s12043-021-02077-1.
- [135] I. Vurgaftman and J. R. Meyer, “Band parameters for nitrogen-containing semiconductors,” *J. Appl. Phys.*, vol. 94, no. 6, pp. 3675–3696, Aug. 2003, doi: 10.1063/1.1600519.
- [136] K. B. Nam, J. Li, M. L. Nakarmi, J. Y. Lin, and H. X. Jiang, “Unique optical properties of AlGaIn alloys and related ultraviolet emitters,” *Appl. Phys. Lett.*, vol. 84, no. 25, pp. 5264–5266, Jun. 2004, doi: 10.1063/1.1765208.
- [137] I. Vurgaftman, J. R. Meyer, and L. R. Ram-Mohan, “Band parameters for III–V compound semiconductors and their alloys,” *J. Appl. Phys.*, vol. 89, no. 11, pp. 5815–5875, Jun. 2001, doi: 10.1063/1.1368156.
- [138] A. J. De Vries, H. S. Kiliaan, and G. Blasse, “An investigation of energy migration in luminescent diluted Gd<sup>3+</sup> systems,” *J. Solid State Chem.*, vol. 65, no. 2, pp. 190–198, Nov. 1986, doi: 10.1016/0022-4596(86)90053-8.
- [139] M. Kučera, M. Nikl, M. Hanuš, and Z. Onderišinová, “Gd<sup>3+</sup> to Ce<sup>3+</sup> energy transfer in multi-component GdLuAG and GdYAG garnet scintillators,” *Phys. Status Solidi RRL – Rapid Res. Lett.*, vol. 7, no. 8, pp. 571–574, 2013, doi: 10.1002/pssr.201307256.
- [140] S. I. Omelkov, M. Kirm, V. A. Pustovarov, and L. I. Isaenko, “Energy transfer in pure and rare-earth doped SrAlF<sub>5</sub> crystals,” *IOP Conf. Ser. Mater. Sci. Eng.*, vol. 15, no. 1, p. 012011, Nov. 2010, doi: 10.1088/1757-899X/15/1/012011.
- [141] D. Spassky *et al.*, “Decay Kinetics of Gd<sub>3</sub>Al<sub>2</sub>Ga<sub>3</sub>O<sub>12</sub>:Ce<sup>3+</sup> Luminescence under Dense Laser Irradiation,” *Materials*, vol. 16, no. 3, Art. no. 3, Jan. 2023, doi: 10.3390/ma16030971.
- [142] H. Suzuki, T. A. Tombrello, C. L. Melcher, C. A. Peterson, and J. S. Schweitzer, “The role of gadolinium in the scintillation processes of

- cerium-doped gadolinium oxyorthosilicate,” *Nucl. Instrum. Methods Phys. Res. Sect. Accel. Spectrometers Detect. Assoc. Equip.*, vol. 346, no. 3, pp. 510–521, Aug. 1994, doi: 10.1016/0168-9002(94)90586-X.
- [143] P. J. Alonso, V. M. Orera, R. Cases, R. Alcalá, and V. D. Rodríguez, “Optical properties of  $Gd^{3+}$  in fluorozirconate glasses,” *J. Lumin.*, vol. 39, no. 5, pp. 275–282, Apr. 1988, doi: 10.1016/0022-2313(88)90026-9.
- [144] M. Korzhik *et al.*, “First Observation of the Scintillation Cascade in  $Tb^{3+}$ -Doped Quaternary Garnet Ceramics,” *Phys. Status Solidi RRL – Rapid Res. Lett.*, vol. 17, no. 4, p. 2200368, 2023, doi: 10.1002/pssr.202200368.
- [145] K. A. Persson *et al.*, “Materials Data on  $Gd_3Ga_5O_{12}$  (Mp-2921) by Materials Project,” <https://next-gen.materialsproject.org/materials/mp-2921/> (accessed Jul. 5, 2023).
- [146] K. A. Persson *et al.*, “Materials Data on  $Gd_3Al_5O_{12}$  (Mp-14133) by Materials Project,” <https://next-gen.materialsproject.org/materials/mp-14133/> (accessed Jul. 5, 2023).
- [147] K. A. Persson *et al.*, “Materials Data on  $Lu_3Ga_5O_{12}$  (Mp-14134) by Materials Project,” <https://next-gen.materialsproject.org/materials/mp-14134/> (accessed Jul. 5, 2023).
- [148] K. A. Persson *et al.*, “Materials Data on  $Lu_3Al_5O_{12}$  (Mp-14132) by Materials Project,” <https://next-gen.materialsproject.org/materials/mp-14132/> (accessed Jul. 5, 2023).
- [149] M. Korzhik *et al.*, “Engineering of a new single-crystal multi-ionic fast and high-light-yield scintillation material ( $Gd_{0.5}Y_{0.5}$ ) $_3Al_2Ga_3O_{12}:Ce,Mg$ ,” *CrystEngComm*, vol. 22, no. 14, pp. 2502–2506, Apr. 2020, doi: 10.1039/D0CE00105H.
- [150] H. Haug, “V. M. Agranovich, M. D. Galanin: Electronic Excitation Energy Transfer in Condensed Matter, North-Holland, Amsterdam, New York 1983. 371 Seiten, Preis: Dfl 225.–,” *Berichte Bunsenges. Für Phys. Chem.*, vol. 88, no. 7, pp. 687–687, 1984, doi: 10.1002/bbpc.19840880729.
- [151] E. F. Polisadova *et al.*, “EFFECT OF CERIUM CONCENTRATION ON LUMINESCENT PROPERTIES OF  $Y_3Al_5O_{12}:Ce$  UNDER ULTRAVIOLET EXCITATION,” *Fundam. Res.*, vol. 1, no. №12 2017, pp. 103–109, 2017, doi: 10.17513/fr.41987.
- [152] A. M. Stoneham, *Theory of Defects in Solids: Electronic Structure of Defects in Insulators and Semiconductors*. Oxford University Press, 2001. doi: 10.1093/acprof:oso/9780198507802.001.0001.
- [153] P. Solarz, M. Głowacki, M. Berkowski, and W. Ryba-Romanowski, “Growth and spectroscopy of  $Gd_3Ga_3Al_2O_{12}$  (GGAG) and evidence of multisite positions of  $Sm^{3+}$  ions in solid solution matrix,” *J. Alloys Compd.*, vol. 689, pp. 359–365, Dec. 2016, doi: 10.1016/j.jallcom.2016.07.321.

- [154] T. Kanai, M. Satoh, and I. Miura, "Characteristics of a Nonstoichiometric  $\text{Gd}_{3+\delta}(\text{Al,Ga})_{5-\delta}\text{O}_{12}:\text{Ce}$  Garnet Scintillator," *J. Am. Ceram. Soc.*, vol. 91, no. 2, pp. 456–462, 2008, doi: 10.1111/j.1551-2916.2007.02123.x.
- [155] R. Sifat and A. P. Grosvenor, "Examination of the site preference in garnet type ( $\text{X}_3\text{A}_2\text{B}_3\text{O}_{12}$ ; X=Y, A/B= Al, Ga, Fe) materials," *Solid State Sci.*, vol. 83, pp. 56–64, Sep. 2018, doi: 10.1016/j.solidstatesciences.2018.06.013.
- [156] V. Laguta *et al.*, "Aluminum and Gallium Substitution in Yttrium and Lutetium Aluminum–Gallium Garnets: Investigation by Single-Crystal NMR and TSL Methods," *J. Phys. Chem. C*, vol. 120, no. 42, pp. 24400–24408, Oct. 2016, doi: 10.1021/acs.jpcc.6b08593.

## CURRICULUM VITAE

First name, Last Name	Yauheni Talochka
Birth date	1997-05-27
Email	yauheni.talochka@ff.vu.lt

### **Education**

2014-2019	<u>Bachelor's degree:</u> Physics (science research activity), Theoretical Physics and Astrophysics, Faculty of Physics, Belarusian State University
2019-2020	<u>Master's degree:</u> Physics, Faculty of Physics, Belarusian State University
2020-2024	<u>Doctoral studies:</u> Physics, Institute of Photonics and Nanotechnology, Vilnius University

### **Professional experience**

2018-2023	Junior researcher: Research Institute for Nuclear Problems, Belarusian State University
Since 2020	Junior researcher: Institute of Photonics and Nanotechnology, Vilnius University

FOR NOTES

FOR NOTES

Vilniaus universiteto leidykla  
Saulėtekio al. 9, III rūmai, LT-10222 Vilnius  
El. p. [info@leidykla.vu.lt](mailto:info@leidykla.vu.lt), [www.leidykla.vu.lt](http://www.leidykla.vu.lt)  
[bookshop.vu.lt](http://bookshop.vu.lt), [journals.vu.lt](http://journals.vu.lt)  
Tiražas 15 egz.